UC Irvine
UC Irvine Electronic Theses and Dissertations

Title

Combined Spectroscopic and Computational Approaches to Understand Surface Behavior of Aqueous Solutions

Permalink

https://escholarship.org/uc/item/6mm9x600

Author

Parry, Krista Monique

Publication Date

2017

Peer reviewed|Thesis/dissertation

UNIVERSITY OF CALIFORNIA,
IRVINE

Combined Spectroscopic and Computational Approaches to Understand Surface Behavior
of Aqueous Solutions

DISSERTATION

submitted in partial satisfaction of the requirements
for the degree of

DOCTOR OF PHILOSOPHY

in Chemistry

by

Krista M. Parry

Dissertation Committee:
Professor Douglas Tobias, Chair
Professor Filipp Furche
Professor Sergey Nizkorodov

2017

TABLE OF CONTENTS

LIST OF FIGURES

LIST OF TABLES

ACKNOWLEDGMENTS

CURRICULUM VITAE

Krista M. Parry

EDUCATION

Doctor of Philosophy in Chemistry, ChaMP   **2017**
University of California, Irvine   *Irvine, CA*

Master of Science in Chemistry, ChaMP   **2017**
University of California, Irvine   *Irvine, CA*

Bachelor of Science in Chemistry, Applied Mathematics   **2011**
University of Arizona   *Tucson, AZ*

RESEARCH EXPERIENCE

Graduate Research Assistant   **2011–2017**
University of California, Irvine   *Irvine, California*

Undergraduate Research Assistant   **2010–2011**
University of Arizona   *Tucson, AZ*

TEACHING EXPERIENCE

Teaching Assistant   **2011–2017**
University of California, Irvine   *Irvine, CA*

REFEREED JOURNAL PUBLICATIONS

Quantitative Interpretation of Molecular Dynamics Simulations for X-ray Photoelectron Spectroscopy of Aqueous Solutions   **2016**

Olivieri, G., Parry, K. M., Powell, C. J., Tobias, D. J., and Brown, M. A., *Journal of Chemical Physics*, 2016, Vol. 144,154704, `https://doi.org/10.1063/1.4947027`

Simulated Photoelectron Intensities at the Aqueous Solution-Air Interface for Flat and Cylindrical (Micro-jet) Geometries   **2017**

Olivieri, G., Parry, K. M., Powell, C. J., Tobias, D. J., and Brown,M. A.,*Physical Chemistry Chemical Physics*, 2017, Vol. 19, 19, 6330-6333 , `http://dx.doi.org/10.1039/C6CP07539H`

Specific Cation Effects at Aqueous Solution-Vapor Interfaces: Surfactant-like Behavior of Li^+ Revealed by Experiments and Simulations   **2017**

Perrine, K. A., Parry, K. M., Stern, A. C., Van Spyk, M. H. C., Makowski, M. J., Freites, J. A., Winter, B.,Tobias, D. J. and Hemminger, J. C., *Proceedings of the National Academy of Sciences*, 2017, `https://doi.org/doi:10.1073/pnas.1707540114`

Specific Anion Effects on Na^+ Adsorption at the Aqueous SolutionAir Interface: MD Simulations, SESSA Calculations, and Photoelectron Spectroscopy Experiments   **2017**

Olivieri, G. and Parry, K. M. and D'Auria, R. and Tobias, D. J. and Brown, M.A.,*The Journal of Physical Chemistry B*, 2017, `http://dx.doi.org/10.1021/acs.jpcb.7b06981`

Solvent-Shared Ion Pairs at the Air-Solution Interface of Magnesium Chloride and Sulfate Solutions Revealed by Sum Freuqnecy Spectroscopy and Molecular Dynamics Simulations   **2017**

Götte, L. and Parry, K. M. and Verreault, D. and Allen, H. C. and Tobias, D. J., *The Journal of Physical Chemistry A*, 2017, `https://pubs.acs.org/doi/abs/10.1021/acs.jpca.7b05600`

SOFTWARE

Instantaneous Interface code
C code that calculates the instantaneous interface and related analyses for aqueous solutions.

ABSTRACT OF THE DISSERTATION

Combined Spectroscopic and Computational Approaches to Understand Surface Behavior
of Aqueous Solutions

By

Krista M. Parry

Doctor of Philosophy in Chemistry

University of California, Irvine, 2017

Professor Douglas Tobias, Chair

In this work, the surface behavior of a number of organic and inorganic molecules in aqueous
solution was analyzed using collaborative computational and spectroscopic approaches. It
is well-established that some organic molecules (such as molecular HNO_3) and inorganic
ions (such as I^-) have a propensity for the air/water interface, and this fact has significant
implications for the role that these molecules may play in heterogeneous chemical reactions
in the atmosphere.

Using molecular dynamics in combination with surface-sensitive spectroscopic methods such
as vibrational-sum frequency generation spectroscopy and liquid-jet x-ray photoelectron
spectroscopy, we have discovered some unexpected surface-propensity for various molecules
and determined the driving forces responsible for such behavior.

Introduction

The research presented in this dissertation is centerered on understanding the behavior of interfacial systems relevant to atmospheric chemistry. These systems have mostly consisted of aqueous solutions of organic acids (HNO_3) or alkali-halide electrolyte solutions (NaI, etc.), which act as proxies for aqueous atmospheric aerosol particles. Of particular interest is the behavior of these solutes with respect to the air/water interface. In the case of electrolyte solutions, it has been well-established that some ionic species, particularly large, polarizable anions have a surface preference for the air/water interface in the order of the Hofemister series ($I^- > Br^- > Cl^- > F^-$), while smaller, highly-charged cations tend to be repelled from the interface.[5] In the case of HNO_3 solution, molecular HNO_3 shows a preference for the interface compared to the ionic NO_3^- species.[6,7,8,9,10,11] These findings have significant implications, because the presence of solutes near the air/ water interface increases the availabilty of the species to participate in heterogeneous chemistry.[12,13,14,15,16,17,18,19]

While it is has been shown experimentally that some species have a propensity for the air/water interface, the driving forces for such behavior is not well understood. Many experimental spectroscopic methods such as X-ray photoelectron spectroscopy or vibrational sum-frequency generation spectroscopy are capable of detecting species at the air/water interface, but the thermodynamic and electrostatic driving forces and distributions must be indirectly inferred. In order to obtain molecular-scale insight into the composition and behavior of

such solutions, we can employ computational methods in combination with experimental techniques. In the Tobias lab, we use molecular dynamics simulations to simulate systems of interest, then analyze the data using custom-built codes and scripts. In order to compare and validate our work to real-world observations, we collaborate closely with experimental spectroscopists using surface-sensitive techniques to probe the surface of systems of interest.

One of the primary challenges of these spectroscopic methods is determining the probe depth of the technique. For example, in the case of x-ray photoelectron spectroscopy performed on aqueous solutions, the probe depth can be varied by tuning the kinetic energy of the incident beam. But determining the exact relationship between the kinetic energy and the depth into solution that the signal originates from is difficult. One of the advantages of using a collaborative experimental/computational approach is that we can obtain molecular scale detail of the systems of study using molecular dynamics simulations to aid in interpreting the spectroscopic results.

One common theme in the following work is in the use of the instantaneous definition of the air/water interface (see Ref. 20). This is an important detail, as it allows for an enhanced resolution of the interface, and therefore, a more precise estimate of the composition and species distributions of the species in our systems of study. These analyses were accomplished using custom-built code.

With the exception of Chapters 1 and 6, the work contained herein has been published in peer-reviewed academic journals. Chapter 1 is an unpublished manuscript written between 2012 and 2013 that preceded and motivated the works presented in Chapters 2 (Ref. 1) and 3 (Ref. 2). This manuscript proposed a method to allow for the direct quantitative comparison between liquid-jet x-ray photoelectron spectroscopy to MD simulations of an aqueous electrolyte solution. This method relies on a simple "calibration-point" to map the inelastic mean free path (IMFP) of an ejected photoelectron to its kinetic energy(KE).

After this mansucript was written, we began a collaboration with Giorgia Olivieri and Matthew Brown at ETH Zurich and Cedric Powell at NIST to continue this work using the software package, SESSA. This software allows for the simulation of electron spectra using density profiles derived from molecular dynamics (MD) simulation as input. From the SESSA simulations, the inelastic mean free path curve can be calculated over a range of kinetic energy, and therefore can give a more precise relationship to the inelastic mean free path to the kinetic energy of the ejected photoelectron.

The results of this work highlighted the limitations of the previous "calibration-point" method in defining the relationship between the inelastic mean free path and the electron kinetic energy and therefore invalidated the results of Chapter 1. The manuscript is included here to show the progression of the field and reveal the complexity of mapping the IMFP to the KE. Multiple follow-up works have been published including Chapters 2 (Ref. 1) and 3 (Ref. 2), as well as an additional publication which can be found in Ref. 21.

In Chapter 4 (Ref. 3), a combined approach of liquid-jet x-ray photoelectron spectroscopy (LJ-XPS) and MD simulation were used to study a series of 2 M Li-halide and K-halide solutions. Our study showed that the lithium ion has a strong preference for the air/water interface relative to that of the potassium ion. We show that the main stabilizing force is due to the strong water-ion electrostatic interactions in the solvation shell of Li^+.

In Chapter 5 (Ref. 4), $MgSO_4$ and $MgCl_2$ solutions were studied using MD simulation and vibrational sum-frequency generation spectroscopy. It was shown that the solvent-shared ion pairs play an important role in determining the electric field direction and magnitude at the air/water interface. We conclude that in $MgCl_2$, the Cl^- anion approaches the interface more closely than the Mg^{2+} ion. Conversely, in $MgSO_4$, Mg^{2+} approaches the interface more closely than the SO_4^{2-} anion, effectively reversing the direction of the electric field as observed in the VSFG spectra.

Finally, in Chapter 6, concentrated aqueous nitric acid solution was simulated using *ab initio* molecular dynamics. This is a follow-up study to Ref. 11 and Ref. 10 in which x-ray photoelectron spectroscopy of nitric acid solution was performed over the concentration range of 0.7 M to 7.8 M. In the previous studies, the degree of dissociation was shown to decrease in the interface relative to the bulk, indicating an enhancement of the molecular form of HNO_3 at the interface. Accompanying simulations of a single HNO_3 molecule in various positions within the simulation cell (bulk vs. the interface) suggested that increased hydrogen bonding between water and the molecular HNO_3 served to stabilize the molecule in the interface, relative to in the bulk.

In this work, the simulation of a concentrated HNO_3 simulation provides more statistical evidence for the dissociation behavior of the nitric species as a function of the distance to the air/water interface. In this study, we can determine the probability of various hydrogen-honding configurations that serve to stabilize the molecular HNO_3 species particularly in the interface region, compared to the middle and bulk regions of the solution.

Chapter 1

Photoelectron Spectroscopy Signal Ratios of NaI and KI Solution: Comparison of Experimental Data to Calculated Spectra from MD Simulation

1.1 Introduction

The behavior of ions in aqueous solutions has been a focus for atmospheric chemists and biochemists due to the mounting evidence that the heavy halides preferentially move to the air-water interface.[22, 23, 24, 25, 26, 27, 28, 29, 30] This behavior is interesting not only as a question of fundamental physical chemistry but because it is also involved in important chemistry in biological and atmospheric systems.[31, 32] For example, specific ion effects, such as the Hofmeister effect, modify the solubility and chemical environment of proteins in the body.[33] In the atmosphere, particularly in the planetary boundary layer of the troposphere, the movement of ions to the air-water interface plays an important role in heterogeneous chemical reactions in sea-spray aerosol particles, as they are readily available to react with molecules present in the gas-phase.[12, 34, 35, 36]

Prior to these recent discoveries, it was believed that aqueous ions prefer to be fully solvated and reside in the bulk, leaving an ion-depleted layer at the air/water interface. The revelation that certain ions could be present at atmospherically relevant and biologically relevant interfaces prompted many researchers to investigate the phenomenon resulting in what is now a large body of literature. For recent reviews see references 23, 22, 31, 37, 38, 39. Most of the exciting experimental developments have come from surface-specific methods in which an enhanced population at the interface can be inferred. These include vibrational sum frequency generation,[27, 40, 41, 42, 43, 44] second harmonic generation,[30, 29, 28] and X-ray photoelectron spectroscopy.[24, 25, 22, 45, 46] These studies represent significant progress, but quantitative measurements of surface composition/organization and corresponding quantitative comparison of experimental measurements to simulation results is difficult due to the indirect nature of the measurements.

Here we focus on using molecular dynamics simulations to develop a quantitative connection between experimentally measured X-ray photoelectron spectroscopy (XPS) signal intensities (or ratios thereof) and the composition of an electrolyte solution as a function of depth. Doing so requires knowledge of the probe depth of the experiment, or, in other words, the depth from which the photoelectron was generated. This, in conjunction with the analysis geometry is sufficient to relate measured XPS signal intensity ratios to the depth profile of the interrogated solution.

Experimental photoelectron spectroscopy studies have historically been limited to solid samples. In these experiments, a probe depth could be inferred by carefully controlling the thickness of the solid sample, therefore allowing for the determination of the probe depth of a photoelectron as a function of the kinetic energy of the detected photoelectron. The energy dependence of the photoelectron attenuation can then be determined by changing the angle of the photoelectron detector (common for fixed-energy X-ray sources) or by tuning the incident beam energy using a synchrotron radiation source. A depth profile can then

be constructed by measuring the normalized signal intensity as a function of photoelectron kinetic energy.[24, 45, 25]

Through recent advances in instrumentation and methods, aqueous and liquid solutions have undergone XPS analysis owing to the innovation of the liquid micro-jet experiment.[47] A challenge that remains in the analysis of LJ-XPS spectra is the determination of the probe depth with sufficient spatial resolution to allow for an accurate depth profile of the solution. The experimental determination of the probe depth in liquid samples is particularly challenging for a number of reasons, perhaps the most confounding of which is that unlike for a solid sample, the number of molecular layers present cannot be controlled for a liquid jet. This fact makes difficult the assignment of the relationship between a length scale and photoelectron kinetic energy.

In order to analyze PE signal intensities, we must understand the behavior of photoelectrons in condensed matter. Probing of the sample with incident beam energy can result in a number of processes in matter including single or collective excitations or ionization and the ejection of a photoelectron that can then undergo elastic or inelastic scattering off of the surrounding electron density. For the purposes of this study, we will focus on elastic and inelastic photoelectron scattering events, as the determination of the inelastic mean free path (IMFP) of a detected photoelectron is integral in obtaining a depth profile of the interrogated solution. This quantity, defined as the mean distance a photoelectron travels in a medium between successive inelastic collisions, will be used interchangeably with the terms "probe depth" and "electron attenuation length" in the remainder of this work. While these terms are not synonymous for materials with strong elastic scattering, we justify this approximation as the effects of elastic scattering in the particular energy regime studied here are negligible. Therefore, we assume that the scattering behavior of the majority of photoelectrons detected experimentally have not participated in elastic scattering events.

A large number of experimental studies have been performed to determine the dependence of

the IMFP on the electron kinetic energy (eKE) in many materials including metals, elements and organic compounds.[48,49,50,51,52,53,54] A general trend in the IMFP to eKE relationship can be observed in the universal curve - a trendline through a compilation of IMFP data from many materials - proposed in Reference.[49] While this universal curve removes any material dependence from the IMFP-to-eKE relationship, it is important to note that an IMFP minimum is observed in the 30 to 100 eV range.[49] This minimum in the IMFP curve, typically reported to be between 5 - 10 Å,[49,54] represents the maximum surface sensitivity of the XPS experiment. IMFP tends to increase sharply in the low kinetic energy range, and shows a more slowly increasing relationship on the high energy side of the IMFP minimum.

Theoretical methods for calculating IMFP curves as a function of electron kinetic energy using material-specific input parameters have been developed with varying degrees of agreement. Some examples include the predictive TPP formula[51] (used extensively in the NIST IMFP database[55]), as well as the use of the Lindhard dielectric function in calculating the energy-loss-function, the imaginary part of the inverse of which gives the inelastic mean free path function within the plane-wave first-Born approximation.[56] While these predictive methods are useful, agreement with experimental data is dependent on the material in study and/or may be limited to a specific kinetic energy range.

In this study, our aim is to establish an empirical relationship between IMFP and eKE to enable the quantitative comparison of experimental and simulation XPS data. Here, we chose to compare our simulation data to a recent experimental study performed by Ottosson *et al.* in which aqueous 4M NaI solution and neat water was interrogated via the liquid-microjet XPS technique. The present study involves several related analyses: (1) XPS signal intensity ratio plots are calculated from density profiles obtained from simulation, (2) a relationship between IMFP and electron kinetic energy is derived using a "calibration point" method and IMFP water curves, (3) experimental water PE data is mapped to an IMFP length scale and compared to various water PE data sets, (4) XPS signal intensity ratio plots from

Atom	q (e$^-$)	σ (Å)	ϵ (kJ/mol)	$N_{electrons}$	ξ (Å)	η
O	-0.8476	3.166	0.65	10	2.4	1.0
H	+0.4238	-	-	-	-	-
Na$^+$	+1.0	2.234	0.65	10	-	-
K$^+$	+1.0	2.945	0.65	18	-	-
I$^-$	-1.0	5.014	0.9846	54	2.7	3.35

Table 1.1: Simulation parameters

simulation and experiment are quantitatively compared using methods described in (2), and (5) an IMFP curve is derived for 4M NaI aqueous solution.

1.2 Methods

1.2.1 Molecular dynamics simulations

Specific ion effects are believed to be a result of several factors- the ion's size, charge, and polarizability - but the contribution of these factors to ion specificity have been analyzed with inconsistent and sometimes contradicting results.[57] The earliest simulations to exhibit a surface propensity of certain ions to the air/water interface employed polarizable models, demonstrating the importance of the energetic benefit resulting from the induction of a dipole.[58,59] Models that do not explicitly include polarization obviously cannot capture the induction effect itself (nor the energetics). However, this does not mean that a model that does not include polarization cannot be thermodynamically stable at the air/water interface. Indeed, as several researchers have pointed out, ions can be represented by non-polarizable models that capture certain thermodynamic properties including stabilization at the interface.[60,61,62,63] Here, we use one such non-polarizable model of Horinek *et. al*[60] parametrized to reproduce the solvation free energy and the first maximum in the ion-oxygen radial distribution function.

Two solutions of approximately 2 M KI and 4 M NaI were simulated with a layer of vacuum separating periodic images in the z dimension. This configuration is known as the slab geometry whereby two interfaces are created between liquid and vapor. The unit cell used was 30 Å × 30 Å × 140 Å with periodic boundary conditions implemented in all three dimensions, and the z-axis elongated to accommodate the vacuum layer. The solution consisted of 1728 water molecules and 68 and 147 ion pairs for the 2 M KI and 4 M NaI solutions, respectively. The GROMACS simulation package[64] was used to equilibrate and run MD simulation trajectories for 100 ns with a time step of 1 fs. A neat water slab consisting of 1728 water molecules was also run for 100 ns with identical system properties. The temperature was held constant at 300 K using a Berendsen thermostat with velocity rescaling to ensure correct kinetic energy distribution. Electrostatic interactions were calculated using Particle-mesh Ewald.[65] As mentioned above, we employ the non-polarizable sodium, potassium, and iodide models of Horinek *et. al* and the SPC/E water model.[60,66] Parameters are listed in Table 2.1.

The concentration of the solution simulated in this study was chosen in order to allow for a direct comparison of simulation results to recent experimental data. Experimental XPS data for the 4 M NaI solution was presented in Ref. 46, while experimental data for the 2 M KI solution was performed by Perrine and coworkers (manuscript in preparation). Surface tension values calculated from simulation data is shown in Figure 1.1 , compared to surface tension values measured experimentally in Ref. 67 as well as in Ref. 68. It can be seen in this figure that changes in surface tension with respect to neat water as a function of salt concentration agrees reasonably well with experimental surface tension data.
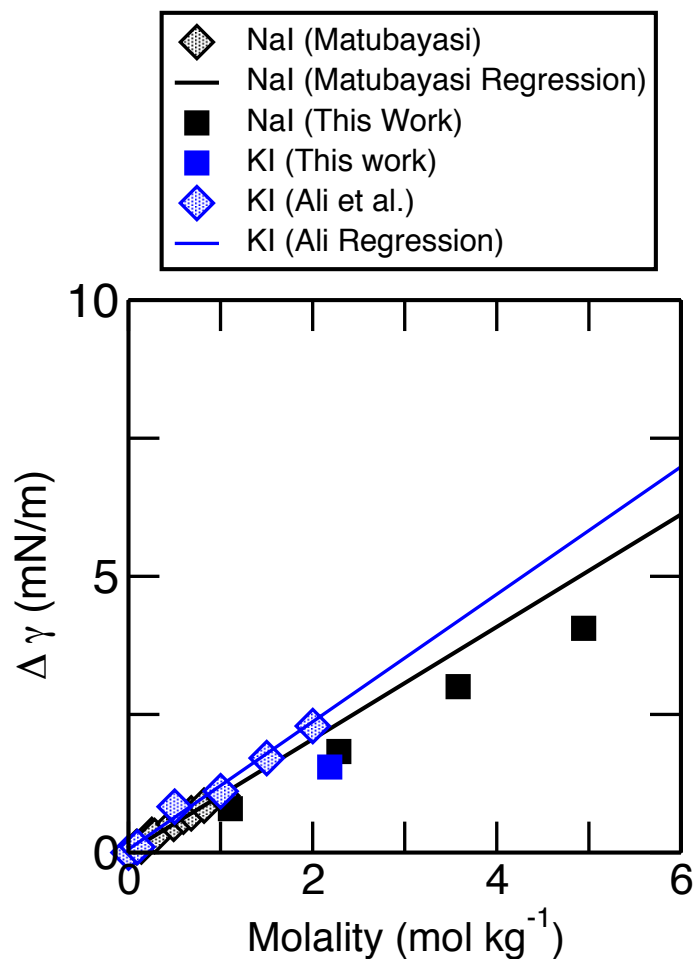
Figure 1.1: Surface tension values from experiment and simulation, plotted as a function of molality. Experimental data adapted from Matubayasi *et al.*[67] for NaI solution, and from Ali *et al.*[68] for KI solution.

1.2.2 Calculation of the XPS signal intensity ratio

The intensity of a measured XPS signal is dependent on several experimental parameters that include surface incidence angle, an experimental alignment factor, light polarization, photon flux, mean detection angle, and transmission function of the electron analyzer.[46] Similarly, characteristics of the species being probed must be accounted for in the analysis of experimental data, including energy-dependent parameters such as the elastic and inelastic

photoionization cross-section and anisotropy factor of the orbital from which the electron was ejected.[46]

Typically, experimental spectra plot the measured signal intensity as a function of the kinetic energy of the detected photoelectrons. Peak identities are assigned based on the binding energy (given by the relationship of the incident beam energy minus the electron kinetic energy of the detected photoelectron), then fitted with Gaussian distributions, integrated and normalized. In the case of the experimental data shown in this study, the XPS spectra at a particular kinetic energy was analyzed using the following equation:[46]

$$I = \alpha F \sigma T \int_{-\infty}^{0} \rho_{\mathrm{i}}(z') \{ e^{[-1/\mathrm{EAL}_{\mathrm{jet}}] \int_{0}^{z'} \rho_{\mathrm{tot}}(y)/\rho_0 \mathrm{d}y} \} \mathrm{d}z' \tag{1.1}$$

where ρ_i is the theoretical density profile of the probed species. The constants in front of the integral are experimental factors mentioned above, with F (photon flux), σ (photo ionization cross section of the species) and T (transmission function of the electron analyzer) being significantly energy dependent. It should be noted here that many of the parameters used in the analysis of the XPS spectra are based on gas-phase measurements of the species, and therefore may not well approximate the parameters for solvated ions.

To calculate the signal intensity of species i from simulation data, we use a method developed by Brown et al.[41] which plots the signal intensity S_i as a function of IMFP. This equation models the attenuation of the photoelectron signal intensity as an exponential decay function of the IMFP - an ansatz employed in most XPS analyses.

$$S_i(\mathrm{IMFP(KE)}) = \int_{0}^{+\infty} \rho_{\mathrm{i}}(z') \, \mathrm{d}z' + \int_{-\infty}^{0} \rho_{\mathrm{i}}(z') \{ e^{[-z'/\mathrm{IMFP(KE)}]} \} \mathrm{d}z' \tag{1.2}$$

12

In equation (1.2) the XPS signal intensity response S_i of an electron ejected from species i with a given kinetic energy-dependent inelastic mean free path (IMFP) in Angstroms, is related to the density profile of the species in solution. From simulation, we have access to the nuclear density profile of the species in solution therefore we can obtain information about the approximate distribution of the species of interest in the solution and how these species contribute to the measured signal intensity. In this case, positive z coordinates correspond to the vacuum, negative values correspond to the liquid phase, and $z = 0$ corresponds to the location of the surface. As we will discuss (*vide infra*), the sensitivity of this calculation to the precise location of the surface is a focal point of this study.

A modification to this equation was proposed to approximate the effects of electron density on the attenuation of electrons in the solution.[45] For solutions of high salt concentration or with regions of population enhancement of a particular species, the electron density will not be constant throughout the solution. Because ejected photoelectrons scatter off of the electron density, a modification to the attenuation function is a factor that approximates the electron density profile. In this case, the electron effective attenuation length is modified by a factor that takes into account the ratio of the electron density of the solution to that of neat water, integrated over the probe depth to the surface. The electron density is calculated by convoluting Gaussian functions onto each nucleus center, defined by their respective Lennard-Jones radii (see Table 2.1 for values), for both the neat water solution, and the alkali-iodide solutions. These convoluted density profiles are then scaled by their respective number of electrons. The electron density, ρ_{e^-}, is then integrated over the probe depth z'', respective to the instantaneous interface. The equation used to calculate the XPS signal intensity for species i is then given by Eq. 1.3.

$$S_i(\text{IMFP}(\text{KE})) = \int_0^{+\infty} \rho_i(z')\,dz' + \int_{-\infty}^0 \rho_i(z')\{e^{[-1/\text{IMFP}(\text{KE})]\int_{z'}^0 [\rho_{e^-,\text{soln}}(z'')]/[\rho_{e^-,\text{water}}(z'')]dz''}\}dz'$$

The relationship between electron IMFP in solution and the electron kinetic energy cannot be directly extracted from simulation data. Therefore, in order to obtain meaningful results about the atomic composition of the solution, XPS signal intensity ratios for I$^-$/cation and I$^-$/O will be plotted as a function of IMFP. It should be noted that experimental signal intensity ratio plots are given as a function of the electron kinetic energy of the ejected photoelectron.

1.2.3   The instantaneous interface

The XPS signal intensity, modeled here by equations 1.2 and 1.3, depends on the location of the interface. A widely used definition of the interface between two components is the Gibbs dividing surface. In the case of the air/water interface, the Gibbs dividing surface (GDS) is the point where the Gibbs excess is 0. The configuration of our simulation cell dictates that the GDS is a plane, the location of which is typically calculated from the time averaged density profile of the solvent. Although the GDS is simple and useful in many instances, we have shown that a planar definition of the interface can obscure structural organization of a solution.[63] Instead, by employing an "instantaneous" definition of the interface – that is to say, one that is not time-averaged and accounts for the molecular-scale roughness inherent to the surface of a liquid – structure of the solvent and solutes is able to be resolved.

Here, the air/water instantaneous interface was determined following the protocol developed by Willard & Chandler.[20] Density profiles are constructed by referring the positions of the atoms to the location of the instantaneous interface. The interface itself is calculated at each time step by locating the isodensity surface corresponding to half the bulk density. This is computed from the coarse-grained density field constructed by means of a convolution of the

atomic positions with a Gaussian given by:

$$\phi(r; \eta, \xi) = \eta(2\pi\xi^2)^{-3/2} \exp(-r^2/2\xi^2) \tag{1.4}$$

For the large iodide ion and the water oxygen, the half-width of the gaussian, ξ, was set to the values of 2.7 Å and 2.4 Å, respectively. The iodide ion was scaled by a factor, η set to 3.35 to obtain homogeneous local density throughout the solution. Due to the small size of the sodium and potassium cations, no convolution was performed on the atom centers as it was determined that they contribute little to the overall solution density.
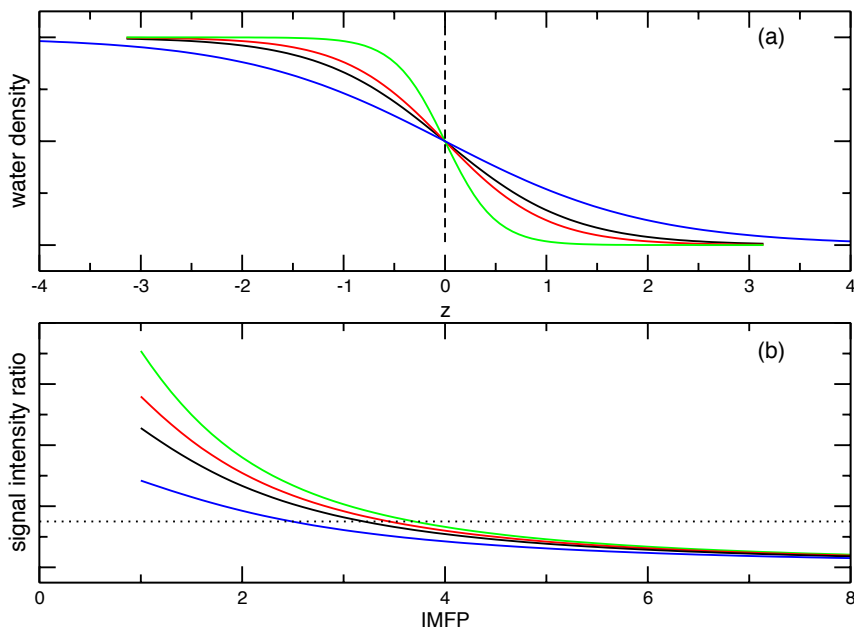
Figure 1.2: Illustrative figure depicting the dependence of the XPS SIR on the system size. Colored curves indicate systems of increasing size, with green being the smallest and blue the largest. Panel (a) shows changes in width of the interfacial region of the water density profile, using the GDS definition of the interface at z=0 Å. Panel (b) depicts anion-to-cation signal intensity ratios calculated from MD simulations of different system sizes. The dotted horizontal black line illustrates the choice of a signal intensity ratio value to be used as a calibration point, and the varied corresponding IMFP value depending on the system size.

Further justification for the implementation of the instantaneous interface as opposed to the Gibbs dividing surface stems from the dependence of the GDS width on the system size. This feature can be explained within capillary wave theory, which dictates that the root mean square dispersion of the dividing surface (GDS) is proportional to the square of the length of the interfacial plane.[69] Figure 1.2 is an illustration of system size effects on the width of the interfacial region and in turn, the effect on the shape of the XPS anion-to-cation signal intensity ratios. For larger system sizes, XPS signal intensity ratio curves become significantly shallower near the interface and would lead to smaller IMFP values for the

same signal intensity ratio value as system size increases. Density profiles referenced to the instantaneous interface are not subject to such system-size effects, and we therefore expect the XPS signal intensity ratios calculated from our MD simulations to reflect structural details that occur on the microscopic scale near the interface.

1.2.4   Mapping eKE to IMFP

As discussed in the introduction, the relationship between the inelastic mean free path and the energy of the ejected electron is not well defined in liquid samples. Using the liquid-jet technique, experimental PE data of liquid samples gives only information relating the PE signal (in arbitrary units) to the electron kinetic energy of the ejected particle. In order to make direct comparisons between experimental and simulation XPS data, it is necessary that both the calculated and the measured signal intensities (or ratios thereof) are plotted as functions of the same coordinate. Experimentally measured depth profiles are constructed as a function of the electron kinetic energy. On the other hand, due to the fact that the exact relationship between IMFP and photoelectron KE is unknown, theoretical XPS signal intensity ratios can only be calculated as a function of the IMFP. Thus, deriving a relationship between the inelastic mean free path and electron kinetic energy is critical in making a direct comparison between simulation and experiment. Methods for determining this relationship for liquid samples have been limited to simply estimating the relationship between IMFP and eKE by a best fit to MD simulation data. In this method, a linear relationship between the signal intensity and the inelastic mean free path is established by deducing the correspondence between eKE and IMFP at a single "calibration point" through the use of MD simulations.[46] While the method is simple to employ, it is very sensitive to the choice of the calibration point which, in turn, is sensitive to the force fields implemented in the MD simulations.

In this study, we propose an alternate method of estimating the relationship between eKE and IMFP. An essential feature of our methods is that rather than calibrating the solution response at a single coordinate in energy-length space, we account for relationship between IMFP and eKE using the complete domain of the function. This allows us to (a) from MD simulation, generate theoretical XPS SIR as a function of eKE for comparison to experiment, b) test various proposed IMFP-eKE curves, and (c) compute a theoretical eKE-IMFP curve that exhibits mutual agreement between experiment and simulation.

1.3   Results and Discussion

1.3.1   Density profiles from MD simulation
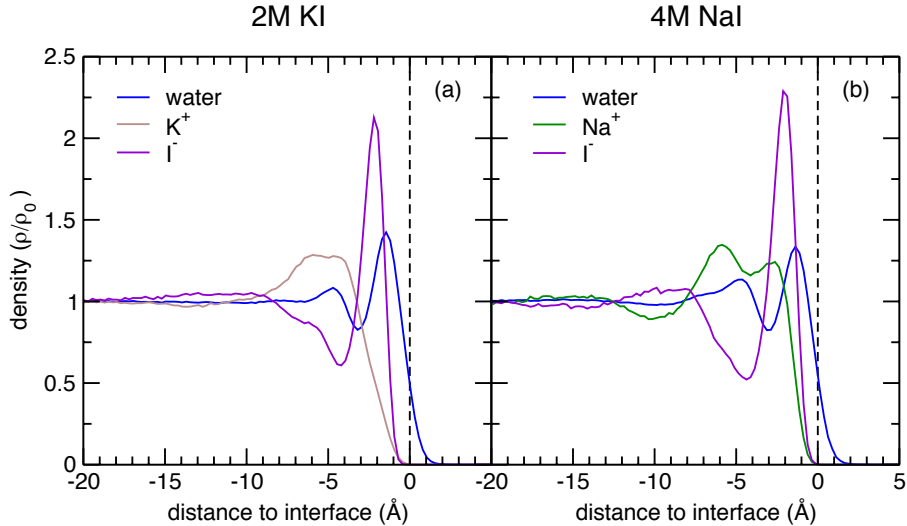
Figure 1.3: Density profiles in the z-direction of water, sodium ions and iodide ions referenced to the instantaneous interface for 2 M KI (panel (a)) and 4 M NaI solution (panel(b)). The bulk density is reached ~ 15 Å into the solution, and the center of slab is located ~ 35 Å from the interface. Density profiles are divided by the bulk density to show details of enhanced ion population at the interface. The instantaneous interface corresponds to 0 Å on the distance axis, indicated by the vertical black dashed line that intersects the water density profiles at approximately half the bulk density.

In this work, we will reference the work of Ottosson *et al.*, in which both experimental and simulation data is presented, with significantly different results than our findings. Some of these differences between the current study and that of Ottosson *et al.* can be attributed to the use of a different FF to model ion behavior. Additionally, the use of the instantaneous

definition of the interface gives a more structured and precise location of the surface that is otherwise washed-out using the time-averaged GDS.

We begin by examining the structural organization of the solution. Figure 1.3 shows the density profiles of the three species in solution along the z-coordinate, referenced to the instantaneous interface located at $z = 0$ Å. The structuring of water, evident in the density profile taken with respect to the instantaneous interface, is normally obscured in a similar profile referenced to the GDS. This is because height fluctuations of the interface (on the order of Ångstroms) can result in significantly different measurements of a molecule's measured position relative to each definition of the interface. In other words, due to height fluctuations, a water molecule located at the instantaneous interface may or may not be located at the GDS, which is essentially a fixed plane.

In both solutions, a surface enhancement of iodide can be seen at the interface within the first water layer, followed by a sub-surface depletion several angstroms into the solution. The iodide profile reaches its bulk value at approximately 15 Å below the surface. It is clear from the density profiles that the iodide population is not only enhanced near the interface, but the peak in iodide population density is nearly spatially coincident with the first maximum in the water population density. This indicates that the iodide ion approaches the instantaneous interface and resides in the topmost monolayer of water.

In panel (a), a broad single peak is observed for the potassium density, spanning from about 4 to 7 Å into the solution (coincident with the depleted iodide region), before slowly falling off to the bulk density ~ 20 Å into solution. In panel (b), a small enhanced double-layer appears in the sodium density profile, with the first and second peaks reaching their respective maximums around 3 Å and 6 Å into the solution. A small sub-surface depletion of sodium (with respect to bulk) is observed at ~ 10 Å from the interface which converges to the bulk value at a depth of 20 Å into solution.

The structural organization of electrolyte solutions of finite concentration is of particular interest.[70] While we know that the heavy halide ions move to the interface in aqueous solutions, this surface propensity can be modified with the addition of solutes or the use of other solvents.[71,72] Additionally, there is evidence for cation specific modification of the surface propensity of the halide ions. Cations in aqueous solutions have been studied with results suggesting that cation size and polarizability may affect the stability of halide ions, as well as affecting the organization of water molecules near the interface.[46] The presence of a small enhancement in the sodium profile (panel (b)) directly following the peak in iodide population can be partially attributed to electrostatic interactions between the negatively charged iodide ions and the positive sodium cations in order to maintain charge neutrality within the solution. The small size and high charge density of the sodium ion may offer a complementary explanation as to the presence of the double-layer structure as it has been shown to interact strongly with water molecules via the disruption of water-water hydrogen bonds.[46,73,74] This feature is much less prominent for potassium (panel (a)) which could be rationalized physically by the larger size and lower charge density of the cation.

1.3.2 XPS signal intensity ratios
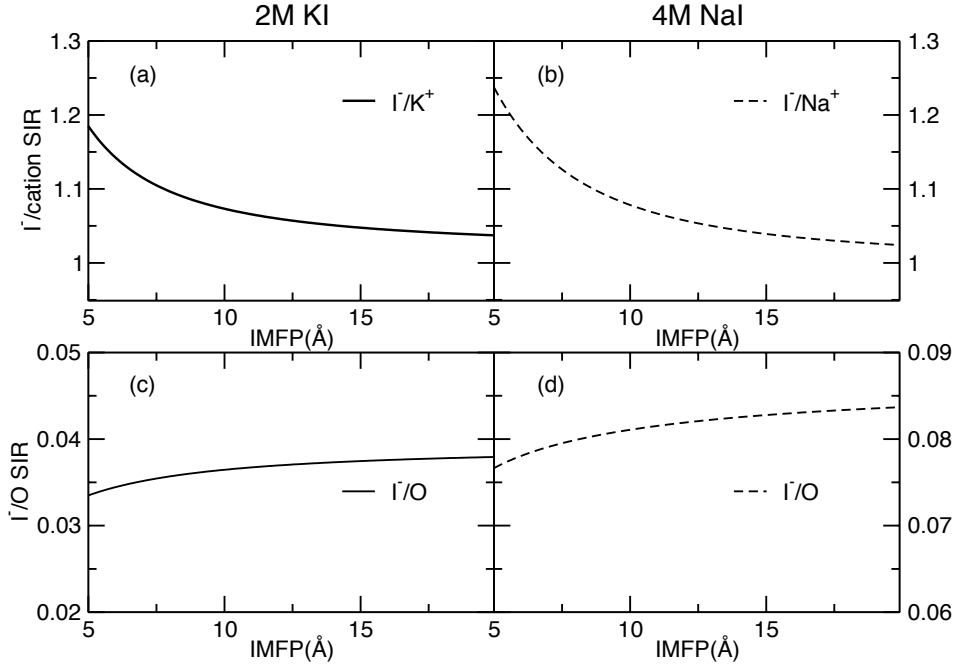
Figure 1.4: XPS signal ratio plots of I^-/cation and I^-/O_{water} plotted as a function of the inelastic mean free path (IMFP) calculated from simulation for 2M KI solution and 4M NaI solution. In the upper panels (a) and (b), the XPS signal ratio converges to the expected atomic ratio of 1 for equal Na^+ or K^+ and I^- concentrations in the bulk solution. In panel (c), the XPS signal ratio converges to 68/1728, ~ 0.039 for the bulk ratio of I^-/O for the 2M KI solution. In panel(d), the XPS signal ratio converges approximately to the expected atomic ratio of 147/1728, ~ 0.085 for the bulk concentration ratio of I^- to water.

The structural organization of the electrolyte solution is closely related to the measured XPS signal. Photoelectrons generated near the surface will be attenuated less than those generated in the bulk. The degree of attenuation depends sensitively on the depth from which the photoelectron is generated and the probability of generating a photoelectron is related to the differential cross section and the density of the species probed. Therefore, a more highly resolved density profile, such as the profile obtained by using the instantaneous

interface, should yield better agreement with XPS experimental data.

In Figure 1.4, XPS signal intensity ratios (SIRs) for iodide/sodium were calculated using equation 1.3 that takes into account the electron density of the solution in the attenuation of photoelectrons. From MD simulation, we are able to compute what is effectively the nuclear density profile. This is then convolved with a weighted Gaussian to approximate the charge distribution of the solution.

The calculated I^-/Na^+ and I^-/K^+ XPS signal ratios, shown in Figure 1.4, shows a ratio >1 at short probe depths. It should be noted that using Equation 1.3 to calculate signal intensity ratios allows for the choice of any value of inelastic mean free path, but the detection of a photoelectron with IMFP less than a few angstroms is not physically realistic. Therefore, we choose a minimum IMFP value of 5 Å to begin plotting the signal intensity ratio plots, as this is the minimum probe depth at 200 eV estimated from experiment. As the probing depth is increased, the signal intensity from both sodium and iodide are roughly equal, and thus the signal intensity ratio approaches unity. We emphasize here that the reason we plot XPS SIR as a function of IMFP is due to the fact that the relationship between IMFP and photoelectron KE is, as of yet, unknown.

As expected, iodide enhancement near the interface is reflected in the XPS signal intensity ratio plots, with a large XPS signal intensity originating from the iodide ions near the surface (IMFP = 5 Å). The rapid convergence of the signal ratio to unity indicates that the surface enhancement of iodide is very localized to the interfacial region, with iodide enhancement occurring within only the first 5 to 10 Å of the interface. This is consistent with the surface enhancement observed in the density profile in which the maximum density occurs at approximately $z = -2.5$ Å, *i.e.* 2.5 Å below the surface, and by $z = -12$ Å, the number densities of sodium or potassium and iodide are nearly equal.

The ability to detect such localized surface ion enhancement is a direct consequence of

the use of the instantaneous interface definition of the air/water boundary. Simulations that implement the Gibbs Dividing Surface definition of the interface tend to show ion enhancement over a broad interfacial region and obscure the movement and localization of ions at the surface as a part of a thermally fluctuating aqueous system. As seen in various studies of similar systems,[63] XPS signal intensity ratios derived using the instantaneous interface definition exhibit much more sharply peaked spectra near the interface, and indicate a very localized surface enhancement.

1.3.3   Comparison of water PE data sets
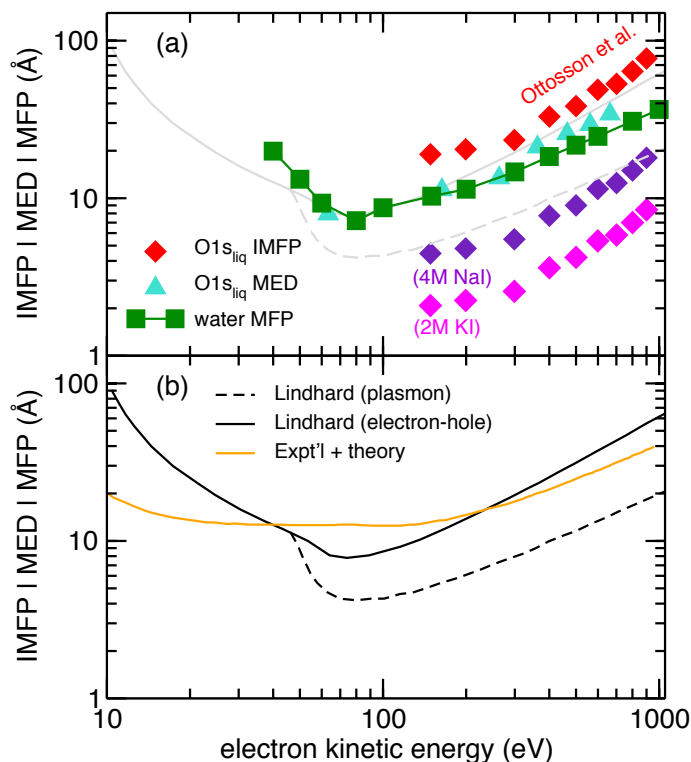
Figure 1.5: Experimental and theoretical IMFP values plotted as a function of kinetic energy (note Log-Log scale). Experimental and calculated inelastic mean free path (IMFP), mean escape depth (MED), and mean free path (MFP) for O1s water valence electrons in neat water are plotted in panel (a). Red diamond data points are taken from Ref. 46 and plotted using a "calibration point" to obtain the relationship between IMFP and electron kinetic energy. Indigo and magenta data points use "calibration points" discussed in this section to determine IMFP to eKE relationship. Cyan triangle data points are experimental O1s water presented in Ref. 75 using a "calibration point" to estimate the mean escape depth of the detected photoelectrons. Green diamond data points correspond to theoretical values calculated for the mean free path of a photoelectron in neat water from Ref. 76. In panel (b) black curves correspond to the IMFP for neat water, calculated using the electron-hole and plasmon contributions to the Lindhard dielectric function from Ref. 56. These curves are also shown in gray in panel (a) for comparison. The orange curve corresponds to the IMFP* curve presented in Ref. 77 from the combination of experiment and theoretical methods in the low eKE region.

As we have noted, the relationship between IMFP and eKE for liquid solutions is an open question. However, several attempts have been made to estimate or calculate the relation-

ship, the most relevant of which are shown in Figure 1.5.

In panel (a), red diamond data points correspond to the experimental water O1s core-level ionization data, mapped with a calibration point from simulated I^-/Na^+ signal intensity ratio plots presented in Ref. 46. The magenta data points correspond to the same O1s experimental data using a calibration point from the simulated 2M KI solution to define the IMFP-to-eKE relationship, while the indigo points are mapped using the calibration point from the 4M NaI solution. Surprisingly, the remapped data using the calibration point from the 2M KI data shifted the IMFP scale of the water data significantly lower than the shift using the 4M NaI calibration point. This is counterintuitive, as we would expect the effect of the ion population at the interface in a more concentrated solution to result in more inelastic scattering. Green and cyan data points correspond to IMFP-vs.-KE data obtained for water samples via several different experiments from references 76, 75, respectively. These points appear to agree well with each other and with theoretical curves shown in gray and in black in panel (b).

In panel (b), the orange curve corresponds to an IMFP curve proposed for water in Ref. 77 based on a combination of experiment and theory. In this study, an IMFP curve similar to the curve plotted in black was scaled down in the low KE region to agree with some angular-dependent PE measurements that suggested a much smaller IMFP value. The black curves correspond to a theoretical IMFP curve for water based on the Lindhard dielectric function presented in Ref. 56. The solid black curve for eKE $>\sim$ 50 eV takes into account only the electron-hole contribution to the Lindhard dielectric function, whereas the dashed curve in this region takes into account the plasmon contribution.

As is evident in this plot, water PE data mapped to an IMFP length scale using the calibration-point method can differ significantly, even from the same XPS experiment. Similarly, water IMFP curves derived from theory or a combination of theory and experiment show minimal agreement. To test the wide range of estimates for the IMFP curve for liquid,

we selected two results of the ones shown in Figure 1.5. The result of Thürmer *et al.*[77] was chosen because the experiment was conducted using a liquid microjet and the effects of elastic scattering and angular dependence were explicitly accounted for. We also chose to compare to the theoretical IMFP calculations of Emfietzoglou *et al.*[56] in which they employ the Lindhard dielectric function to estimate electron IMFP in water over a wide range of energies.

1.3.4 I^-/Na^+ and I^-/K^+ SIR as a function of eKE
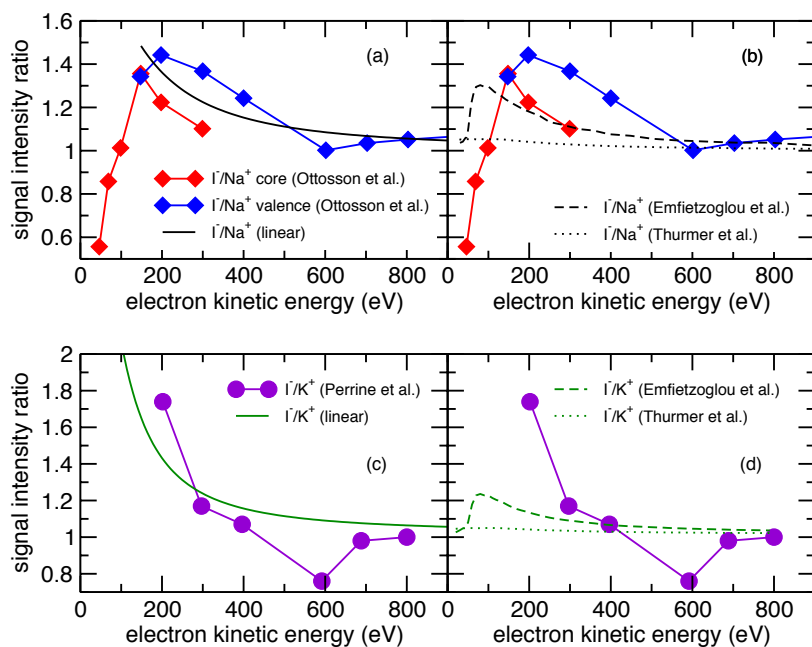
Figure 1.6: XPS signal intensity ratio plots for I^-/Na^+ and I^-/K^+ solutions. Red and blue data points represent experimental NaI data while violet points represent experimental KI data. Black and green curves correspond to NaI and KI simulation data mapped to eKE scale.

Once the relationship between IMFP and energy is known for the photoelectron, the transformation between these coordinates can be made. Thus, the simulated XPS SIRs that we have computed as a function of electron IMFP may be directly compared to experimental XPS profiles measured as a function of photoelectron KE. As stated, IMFP curves from Thürmer et al.[77] and Emfietzoglou et al.[56] are used to establish the IMFP–to–eKE relationship over the kinetic energy range of 80 – 1000 eV. Performing this transformation is straightforward as a composition of functions. In other terms, to perform this transformation a kinetic energy value is chosen, and the corresponding IMFP value determined by the water IMFP curve is found. The signal intensity ratio value for I$^-$/cation (see Figure 1.4) corresponding to this IMFP value is then plotted at the kinetic energy value. This procedure is then carried out over the aforementioned kinetic energy range.

Panel (a) in Fig. 1.6 shows both experimental I$^-$/Na$^+$ signal intensity ratio data adapted from Ref. 46, and mapped simulation signal intensity ratio data as a function of electron kinetic energy.

The linearly remapped simulation I$^-$/Na$^+$ SIR data follows the trend of experimentally measured I$^-$/Na$^+$ ratios in that iodide enhancement is observed at kinetic energy ~ 175 eV and drops to unity at higher kinetic energies. In this kinetic energy range, probe depth is proportional to electron kinetic energy. Therefore, a I$^-$/Na$^+$ >1 indicates an enhancement of iodide population near the interface. Similarly, I$^-$/Na$^+$ ~ 1 indicates equal iodide and sodium concentrations in the bulk region. An identical analysis for I$^-$/K$^+$ signal intensity plots was performed using experimental and simulation data in panels (c) in Fig. 1.6. Of course, agreement between mapped simulation data and experiment is enforced at the calibration point, but the general trend and extent of ion enhancement at the interface agrees nicely with experiment. Comparison of simulation SIR data calculated in this work to that of Ottosson et al. shows significantly different ion distributions, with much more iodide enhancement near the interface in the Ottosson et al. data.

In panel (b) and (d) of Fig. 1.6, simulated XPS SIRs are transformed from an IMFP to an eKE scale using one of two selected IMFP water curves and is again shown against experimentally measured XPS SIR profiles. In (b) and (d), the dashed curves correspond to the IMFP-to-eKE remapping using the Emfietzoglou *et al.* water curve, while the dotted curves correspond to the transformation with the Thürmer *et al.* curve. The Emfietzoglou *et al.* remapping shows iodide enhancement that has a maximum at ~ 100 eV before dropping sharply for lower electron kinetic energy values. The turn-over observed in the remapped simulated SIR profile mirrors the minimum in the water IMFP curve, but the physical meaning of this feature with respect to ion distribution is unclear. For kinetic energy values greater than the SIR maximum, the SIR curve decays to 1 much more slowly than what is observed in experimental data.

In the profile remapped using the Thürmer *et al.* curve, virtually no iodide enhancement is seen over the entire range of electron kinetic energy. This is a consequence of the broad flat region in the Thürmer IMFP water curve for low kinetic energy values (<100 eV). This would usually be interpreted as an indication that sodium and iodide are present at the interface in equal quantities. However, this contradicts well-established evidence regarding iodide adsorption to the air/water interface[23, 59, 22, 38] and suggests that this IMFP curve is not appropriate for determining the relationship between IMFP and eKE for this solution.

1.3.5 Deriving 4M NaI IMFP curve as a function of eKE
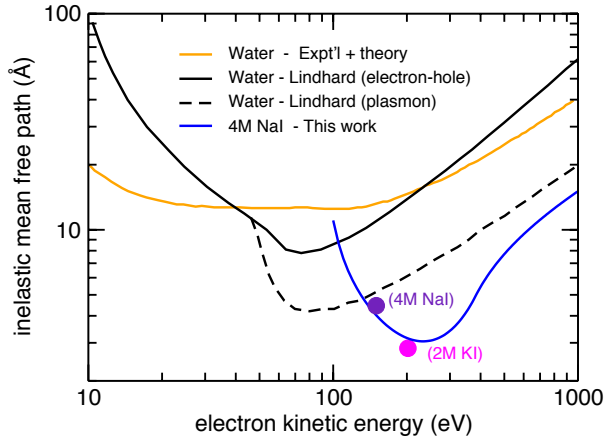
Figure 1.7: Comparison of IMFP curve derived for 4M NaI solution to IMFP curves for pure water. The black solid and dashed curves represent the IMFP function calculated using the electron-hole and plasmon contributions to the Lindhard dielectric function, presented in Ref. 56. The calibration points from the 4M NaI solution and the 2M KI solution used in Sec. 1.2.4 are denoted by purple and pink circles, respectively.

Finally, we propose an IMFP curve for 4M NaI solution that would produce agreement between experimentally measured I^-/Na^+ SIR and those calculated from MD simulation. Figure 1.7 depicts the derived IMFP curve in blue, plotted alongside water IMFP curves from Emfietzoglou *et al.* and Thürmer *et al.* in black and orange, respectively. This IMFP curve was derived over the kinetic energy range of 100 to 1000 eV by numerically computing the transformation that yields agreement between I^-/Na^+ SIR from MD (Figure 1.4) and that measured experimentally. Rigorously, this procedure is a straightforward composition of functions. However, it may be more easily understood as plotting IMFP values as a function of eKE by determining equivalent SIR values between experimental and simulated SIR curves for discretized points over the eKE range. This same analysis was not performed for the 2M KI data because some experimental SIR values fell outside of the range of those observed from simulation (i.e. some experimental SIR values are less than 1) in the kinetic energy range of interest.

We observe a minimum of about 2.5 Å in the 4M NaI IMFP curve around 250 eV, which is much smaller and shifted higher in energy from the minimum in the water IMFP curve. General trends in the IMFP to eKE relationship are consistent with those observed for water and other materials, with a slow monotonic increase in the eKE range greater than the IMFP minimum, and a more sharply increasing curve below the IMFP minimum.[49] As discussed in the previous section, differences between water and aqueous salt IMFP curves are not surprising due to the presence of ionic species, particularly with large, electron-rich species, such as iodide, near the interface.

Interestingly, the calibration points derived from the 4M NaI and 2M KI solutions agree well with the IMFP-to-eKE relationship predicted by the IMFP curve of the 4M NaI solution. While it is expected that the 4M NaI IMFP curve passes through the calibration point defined by the 4M NaI solution, the close agreement of the IMFP curve with the 2M KI calibration point was not expected. This would support the argument that the large iodide species near the air/water interface play a significant role in the scattering behavior of photoelectrons generated in the solution, especially when compared to scattering behavior in neat water.

1.4   Conclusions

The scattering behavior of photoelectrons in liquids is vital to our interpretation of XPS spectra. In particular, the IMFP curve as a function of photoelectron kinetic energy tells us the depth from which the detected electron was generated. Thus, the IMFP-to-eKE relationship is the link between XPS SIR measurements made as a function of eKE and the density profile of the solution.

Using molecular simulation, we can simulate a solution and its interface with air or vacuum. However, the close correspondence between XPS SIR and the solution density profiles makes

it critical that the simulated density profiles are as accurate as possible. Indeed, we have employed models for the ions that have been parametrized to reproduce the thermodynamics of solvation[60, 61] and recapitulate our understanding of the behavior of ions at the air/water interface.[63, 22]

Several of researchers' efforts toward estimating IMFP curves are presented in Fig. 1.5. It is obvious from the large variations between the data sets that there is an overall lack of agreement between experimental, theoretical, and collaborative approaches. While some experimental PE water data mapped to the IMFP length scale using the "calibration point" method may agree reasonably well with other select data sets (i.e. Emfietzoglou *et al.* Lindhard (plasmon) water curve), it is evident that this remapping is very sensitive to the force field used in simulation and the choice of calibration point.

We have calculated XPS signal intensity ratios for the simulated electrolyte solution and compared simulated SIR plots to experimental data. Quantitative comparison of this data was made possible using a "calibration point" and IMFP water curve method to derive an IMFP–to–eKE relationship, thus enabling simulation SIR data to be plotted as a function of eKE. We have determined that the "calibration point" method of IMFP-to-eKE remapping yields good agreement between experimental and simulation SIR data but suffers from the problems that (1) selection of the point to use to calibrate is somewhat arbitrary, and (2) agreement between experiment and simulation are enforced which can mask inaccuracy. However, the method is effective in determining a probe depth for the experiment.

By employing the IMFP curves for water published by other groups, we were able to determine if either of these were able to recapitulate the experimental XPS SIR measurements for a sodium iodide solution. It is evident from the transformations that we show in panel (b) of Fig. 1.4 that neither shows satisfactory agreement with the experiment. Use of IMFP curves for neat water from both Emfietzoglou *et al.* and Thürmer *et al.* to determine the IMFP-to-eKE relationship fails to capture iodide enhancement effects in the eKE region of

$\sim$ 175-200 eV as is observed in experimental data. Of the possible reasons for this, we believe the most likely is that the published IMFP curves, while likely correct for water, are inappropriate for a concentrated electrolyte solution.

Finally, the derived IMFP curve for 4M NaI solution presented in Fig. 1.7 serves as an illustration of the differences in electron attenuation between neat water and electrolyte solutions. While we do not assert that this curve reflects the true IMFP-to-eKE relationship in 4M NaI solution, we can infer some information regarding changes in probe depth - most notably, at low kinetic energy (150 eV) the probe depth into solution is approximately 5 Å, as opposed to 15 Å predicted by Thürmer *et al.* and 7 Å and 10 Å predicted by the electron-hole and plasmon contributions of the Emfietzoglou *et al.* curve for water. Further progress on this issue would likely require the experimental determination of an IMFP curve for 4M NaI solution. Similarly, experimental determination of the photoelectron angular distribution may elucidate changes in ion solvation and subsequent effects on elastic and inelastic scattering cross-sections, therefore enabling improved experimental data analysis.

Chapter 2

Quantitative Interpretation of Molecular Dynamics Simulations for X-ray Photoelectron Spectroscopy of Aqueous Solutions

2.1 Introduction

Core-level X-ray photoelectron spectroscopy (XPS) is a chemical-specific analytical technique that many consider to be the workhorse of surface and interface science. Major advantages of XPS are its surface sensitivity,[78] its ability to detect every element of the periodic table except hydrogen, and the fact that many compounds can be analyzed without significant decomposition by the incident X-ray beam. In order, however, to interpret XPS signal intensities quantitatively, a comprehensive understanding of the attenuation and scattering of the photoelectrons in the sample is required. One important sample parameter in this regard is the electron inelastic mean free path (IMFP), which together with the photoelectron emission angle determines in large part the surface sensitivity of XPS experiments.[78] In solids, appropriate models and the required data are available for accurate predictions of IMFPs for energies greater than 50 eV,[79,80,81] many of which have been confirmed experimentally.[82] In liquids, more specifically in aqueous solutions, consensus remains elusive and several publications report substantially different values for the electron IMFP.[83,46,77,84,85] This poor understanding of the electron IMFP limits the ability to quantitatively interpret XPS signal intensities from aqueous solutions.

In order to quantitatively describe the structure of an aqueous solution interface, it is commonplace to turn to molecular dynamics (MD) simulations for confirmation of depth-resolved, a term that is interchangeable with energy-dependent, XPS signal intensities.[46,24,86,87,72] MD simulations yield molecular-level solute (typically an electrolyte) and solvent (most often water) distributions with respect to depth and, over the past decade, have contributed enormously to our microscopic understanding of the vapor (or vacuum)-aqueous electrolyte interface.[23] Direct comparison of MD simulations with XPS signal intensities are, however, not straightforward. MD simulations provide an atomic-scale description of molecular distributions in the vicinity of the interface, whereas XPS is an integrated technique that samples

a depth that depends on the IMFP for the photoelectron energy, the photoelectron emission angle, and a parameter describing the strength of elastic scattering.[78] The crux of the problem is, therefore, to relate water and solute distributions obtained from MD simulations to the XPS signal intensities measured for different photoelectron energies. The solution requires better knowledge of the IMFP as a function of energy for water and aqueous solutions. In this article we describe what we believe to be the first quantitative interpretation of MD simulation profiles for XPS signal intensities of aqueous solutions of 2 mol/L KI and 1 mol/L NaI.

The present contribution is not intended to entirely resolve the debate surrounding the energy dependence of the probe depth in XPS experiments on aqueous solutions (the resolution will most likely come from novel experiments), but rather sets out to establish a straightforward and consistent protocol using the National Institute of Standards and Technology (NIST) database for the Simulation of Electron Spectra for Surface Analysis (SESSA)[88,89] to enable a direct interpretation of MD simulations with XPS signal intensities. As our understanding of electron IMFPs and elastic-scattering effects in aqueous solutions continues to evolve, the calculations reported herein can be updated.

2.2 Methods

2.2.1 Molecular Dynamics Simulations

MD simulations of $\approx$ 2 mol/L KI (68 ion pairs and 1728 water molecules) and $\approx$1 mol/L NaI (32 ion pairs and 1728 water molecules) solutions were performed using the Gromacs simulation suite,[90,91,92,93,64] version 4.6.3. The ions and water molecules were placed in a simulation cell of dimensions 3 nm $\times$ 3 nm $\times$ 14 nm in the x, y, and z directions, respectively. The simulations were carried out with three-dimensional periodic boundary conditions and

a timestep of 2 fs for 100 μs (excluding equilibration time) for the 1 mol/L NaI solution and 80 ns for the 2 mol/L KI solution. Two interfaces formed spontaneously during the equilibration. The average temperature was held at 300 K using a Berendsen thermostat with an additional stochastic term that ensures the correct kinetic energy distribution.[94] The non-polarizable force field developed by Horinek et al.[60] was used to model the ions, and the Simple Point Charge/Extended (SPC/E) model was used for the water molecules.[66] The Lennard-Jones parameters σ and ϵ, and charges associated with each atom type are listed in Table 2.1. Electrostatic interactions were calculated using the smooth particle-mesh-Ewald method,[95] and a cutoff of 0.9 nm was used for the Lennard-Jones interactions and the real-space part of the Ewald sum. Water molecules were held rigid by using the SETTLE algorithm.[96] The average bulk concentrations are computed from the compositions of the innermost 2 nm of the simulated slabs: 0.96 mol/L for NaI and 2.07 mol/L for KI.

Ion	Charge	$\sigma(\text{nm})^{60}$	$\epsilon(\text{kJ/mol})^{60}$	$\xi(\text{nm})$	η
O	-0.8476	0.3166	0.65	0.24	1.0
H	+0.4238	-	-	-	-
Na$^+$	+1	0.2234	0.65	-	-
K$^+$	+1	0.2945	0.65	-	-
I$^-$	-1	0.5014	0.9846	0.27	3.35

Table 2.1: Molecular dynamics (MD) simulation parameters.

The ion force fields used here were optimized in conjunction with SPC/E water to reproduce ion solvation free energies and entropies, as well as the positions of the first peaks in the ion-water radial distribution functions.[60] The resulting models were used to calculate potentials of mean force for the adsorption of single ions to the vapor/water interface, which served as input to extended Poisson-Boltzmann calculations of ion concentration profiles.[60] The latter were used to calculate surface tension increments (difference between the surface tension of a salt solution and the surface tension of neat water). The surface tension increments obtained from the parameter set employed herein agreed well with experimental data up to 1 mol/L.[60] The surface tension increments calculated from our simulations, 0.79 mN/m

for 0.96 mol/L NaI and 1.55 mN/m for 2.07 mol/L KI, are in decent agreement with the experimental values of 1.01 mN/m for 1.0 mol/L NaI and 1.92 mN/m for 2.0 mol/L KI at 293 K,[97] especially considering that surface tension decreases with increasing temperature. In addition, the bulk solution densities calculated from our simulations, 1085 kg/m^3 for 0.96 mol/L NaI and 1263 kg/m^3 for 2.07 mol/L KI, agree very well with the experimental values of 1106 kg/m^3 and 1246 kg/m^3, respectively, interpolated from tabulated measurements at 298 K.[98]

2.2.2 Interface Definitions

Due to thermal fluctuations, the surface boundary separating the liquid and vapor phases is a dynamic and rough interface that evolves along with the movement of the molecules in solution. A common definition of the location of the interface is the Gibbs dividing surface (GDS). In MD simulations, the GDS is located first by computing the water O atom density profile in a static coordinate system, which averages over the thermal fluctuations. The GDS is the position along the coordinate (z) normal to the interface at which the solvent density is equal to half its bulk value. In this study, we implement an additional definition of the interface, the so-called instantaneous interface, proposed by Willard and Chandler.[20] The use of the instantaneous interface as the origin of the interfacial coordinate yields density profiles with molecular-scale resolution. To locate the instantaneous interface, the nuclear positions of each water molecule and ion are convoluted with three-dimensional Gaussian density distributions, with standard deviations ξ and magnitudes η listed in Table 2.1, to construct a density field over the entire simulation cell. The instantaneous interfaces are then determined at each time step as the locus of points at which the density field is equal to half the bulk solution density. To compute the density profiles, the positions of each water molecule and ion are then referenced to the nearest instantaneous interface (above or below). Further details on the implementation of the instantaneous interface

for interfaces of vapor (vacuum) and water or aqueous salt solutions are available in the literature.[20,63] In light of the fact that the escape of photoelectrons from solution at the kinetic energies and information depths of relevance in this study is extremely fast ($\approx 0.5 \times 10^{15}$ second) compared to the thermal fluctuations of the interface ($\approx 10 \times 10^{12}$ second[20]), the instantaneous interface representation is considered more appropriate for comparing MD simulations with XPS data.

2.2.3   Simulation of Electron Spectra for Surface Analysis (SESSA)

XPS signal intensities are simulated using the SESSA software developed by Werner et al.[88,89] SESSA is a NIST standard reference database that contains all data needed for quantitative simulations of XPS and Auger-electron spectra. Data retrieval is based on an expert system that queries the databases for each needed parameter. SESSA performs simulations of photoelectron intensities for user-specified conditions such as the morphology of the sample, the composition and thickness of each layer of a film or the composition and dimensions of a nanostructure, the X-ray source and its polarization, and the experimental configuration. SESSA provides the spectral shape of each photoelectron peak using a model of signal generation in XPS that includes multiple inelastic and elastic scattering of the photoelectrons. In order to minimize the computation time, an efficient Monte Carlo code is employed based on the trajectory-reversal method.[72] In contrast to conventional Monte Carlo codes where electrons are tracked based on their trajectories from the source to the detector, the trajectory-reversal approach tracks electrons in the opposite direction, starting from the detector and working back to the point of origin. Thus, all electrons contribute to the signal, which results in significantly decreased simulation times.

For the SESSA simulations reported in this article, the orientation of the analyzer axis is perpendicular to the X-ray source, while the sample surface normal is oriented in the same

direction as the analyzer axis. The excitation source is a linearly polarized X-ray beam. The polarization vector is rotated 54.7° from the analyzer detection axis, which corresponds to the so-called magic angle in which the XPS intensity is independent of the emission angle. The acceptance solid angle for the detector is $\pm 11°$ and the illuminated area on the sample is independent of the emission angle. The last condition is valid when the X-rays are focused in a relatively small area, as is the case for synchrotron or monochromatic laboratory sources. Our calculations employ electron IMFPs calculated via the semi-empirical TPP-2M formula of Tanuma et al.[80] integrated within SESSA. The calculated IMFPs, which depend on the material density (ρ), atomic or molecular mass, number of valence electrons per atom or molecule, and the band-gap energy, are expected to have uncertainties of about 10 %, although the uncertainty could be larger for a small number of materials.[99] XPS spectra are simulated for two orbitals of each of the elements present in the solutions (O 1s and O 2s; K 2p and K 3p; I 4d and I 3d; Na 2p and Na 2s) using different x-ray wavelengths such that the photoelectron energies of particular lines of interest have the same kinetic energies. This procedure is employed so that the IMFPs of the photoelectrons for the different components within a given solution are the same. The photoelectron energy is varied between 65 eV, where a pronounced minimum in the probing depth of dilute aqueous solution has been proposed[100] and 1500 eV. The latter corresponds roughly with the energy of a laboratory X-ray Al K-α source (1487 eV) and with what is available from most soft X-ray synchrotron beamlines with useful flux. A total of 26 photoelectron energies were simulated. The simulated intensities are then normalized by the atomic photoionization cross sections (built in to SESSA) of Yeh and Lindau.[101]

2.3 Result and Discussion

2.3.1 The Information Depth of XPS

The information depth (ID) or sampling depth is a measure of the surface sensitivity in a particular XPS experiment and is defined as the maximum depth, normal to the specimen surface, from which useful signal information is obtained.[102] Jablonski and Powell developed the following empirical equation for the ID, S:[103]

$$S = \lambda \; cos \; \alpha(1 - 0.787\omega)ln\left[\frac{1}{1 - (P/100)}\right] \tag{2.1}$$

where λ is the IMFP, α is the photoelectron emission angle with respect to the surface normal, P is a specified percentage of the detected signal, and ω is a convenient measure of the strength of elastic-scattering effects on the photoelectron trajectories.[78,104] The ω parameter has a complicated dependence on electron energy and material[78,79] but is typically small (< 0.1) for low atomic numbers (Z $<$ 13) at an energy of 1500 eV but can be larger ($\approx$ 40.4) at much lower energies (e.g., 65 eV). We note that Eq. 2.1 was derived for a homogeneous sample and is normally used for estimating IDs for the detection of most of the photoelectron signal of interest. Values of P $=$ 90 %, P $=$ 95 %, or P $=$ 99 % are typically used.

The majority of XPS experiments from aqueous solutions are performed at soft X-ray synchrotron beamlines where the energy range of practical interest varies from roughly 65 eV to 1500 eV.[83,46,77,85,24,86,87,72] The ID for a semi-infinite, structureless slab (a bulk liquid with no structure at the interface) of pure liquid water was calculated from Eq. 2.1 and is
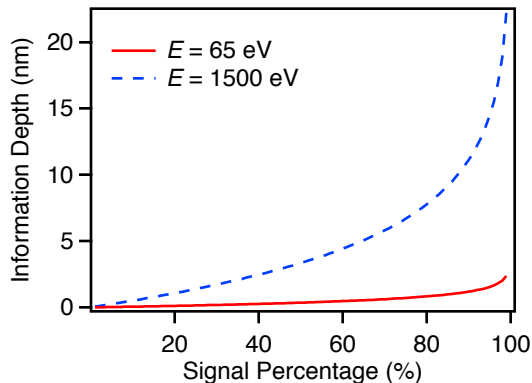
Figure 2.1: Plot of the information depth for liquid water from Eq. 2.1 as a function of the percentage, P, of the detected XPS signal for photoelectron energies, E, of 65 eV (red solid line) and 1500 eV (blue dashed line).

shown in Figure 2.1 for an emission angle $\alpha = 0°$. The ω parameter was obtained from IMFP values at 65 eV (0.77 nm) and 1500 eV (5.03 nm) that were calculated from the predictive TPP-2M equation[80] and from values of the transport mean free path (TMFP) that were retrieved from the SESSA database (1.07 nm and 92.74 nm for energies, E, of 65 eV and 1500 eV, respectively). These IMFP and TMFP values result in $\omega = 0.418$ at 65 eV and $\omega = 0.052$ at 1500 eV, with the larger ω highlighting the importance of elastic-scattering at lower energies. As expected, the surface sensitivity is significantly higher at 65 eV than it is at 1500 eV.

The contribution of the outermost molecular layer of water (0.3 nm) to the overall photoelectron signal can be determined from Figure 2.1. We find this layer contributes only 6 % at an energy of 1500 eV (S = 14.5 nm for P = 95 %) but 44 % at 65 eV (S = 1.5 nm for P = 95 %). The former value reveals the lack of surface/interface sensitivity when working at 1500 eV in aqueous solution, whereas the latter value demonstrates the inability of XPS to probe exclusively the outermost molecular layer of solution for normal emission of the photoelectrons ($\alpha = 0°$). Analogous contributions can be determined for the outermost 1.5 nm of solution (the thickness of the interface region for 2 mol/L KI from the MD simulations, see Section 1.3.3). At 1500 eV, the outermost 1.5 nm of solution contributes 27 % to the

overall signal intensity, whereas at 65 eV virtually all the signal (96 %) originates from this region and almost none of the bulk solution is sampled.

2.3.2   Relation Between Electron Kinetic Energy and Electron IMFP

Photoelectron experiments using X-rays from a synchrotron source are attractive in that the surface sensitivity can be varied simply by changing the X-ray wavelength so that the energy of a particular photoelectron peak corresponds to a desired value of the IMFP for a given material.[105, 106]

The energy-dependent IMFPs from the TPP-2M equation[80] for semi-infinite structureless slabs of water (blue circles), and 1 mol/L (green diamonds) and 10 mol/L (red squares) aqueous solutions of NaI are shown in Figure 2.2 and tabulated in Table 2.2. The command line inputs in SESSA for composition and density are /H2/O/ and $\rho = 9.90 \times 10^{22}$ atoms/cm^3 for water, (/H2/O/)98.78(/Na/)0.61(/I/)0.61 and $\rho = 9.42 \times 10^{22}$ atoms/cm^3 for 1 mol/L NaI, and (/H2/O/)81.65(/Na/)9.17(/I/)9.17 and $\rho = 6.54 \times 10^{22}$ atoms/cm^3 for 10 mol/L NaI, and the band-gap energy (E_g) is assumed constant (7.9 eV) for all three solutions (further discussion on E_g is given in Section 1.3.7). The numbers after each species specify the fractional contribution of each atom to the total atom density of the solution. The electron IMFP monotonically increases in all cases from a minimum at an energy of 65 eV to a maximum at 1500 eV. The calculated electron IMFPs become systematically lower over the entire energy range going from pure water to 1 mol/L and finally 10 mol/L NaI. This result makes clear that a universal curve of electron IMFP as a function of energy likely does not exist for aqueous solutions and, therefore, electron IMFPs will have to be calculated (or determined experimentally) for a wide range of solution compositions.
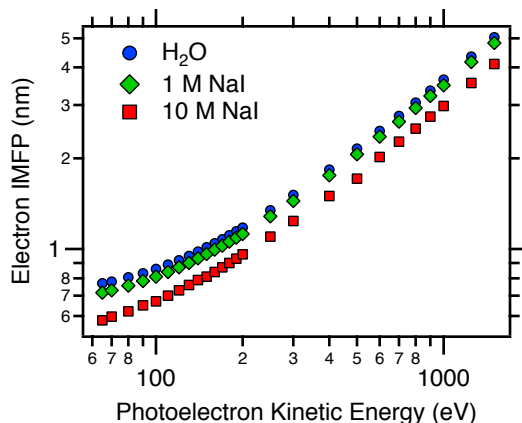
Figure 2.2: Dependence of the electron IMFP on photoelectron kinetic energy. IMFPs for bulk solutions of neat water (blue circles), 1 mol/L (green diamonds) and 10 mol/L NaI (red squares) were calculated with the TPP-2M formula[80] in SESSA. The simulated systems comprise semi-infinite structureless slabs.

2.3.3   Molecular Dynamics Simulations

Ion populations in the vicinity of a solution/vapor interface are often different from the bulk solution composition, and their distributions are typically depicted as density profiles. Here we consider a MD simulation of a 2 mol/L KI solution, a snapshot from which is shown in Figure 2.3. Density profiles have been calculated in the GDS and in the instantaneous-interface representations. Figure 2.3 plots the number density of water (blue), I^- (green) and K^+ (red) as functions of the distance to the GDS, which is the location along z where the mean water density is equal to half its bulk value. Figure 2.3(c) plots the same quantities as a function of the distance to the instantaneous interface, which varies from one configuration to another. In both Figure 2.3(b) and Figure 2.3(c), the density profiles have been positioned such that the interface is at z = 0 nm. Negative values of the horizontal axis indicate depth into the solution.

In both the GDS and instantaneous-interface representations, we observe an enhancement in the ion populations in the vicinity of the interface relative to the bulk. In the GDS representation (Figure 2.3), the density of iodide is enhanced (with respect to the bulk density) with

| Energy | IMFP (nm) | IMFP (nm) | IMFP (nm) |
(ev)	Water	1 mol/L NaI	10 mol/L NaI
65	0.77	0.72	0.58
70	0.78	0.73	0.60
80	0.81	0.76	0.62
90	0.83	0.78	0.65
100	0.86	0.81	0.67
110	0.89	0.84	0.70
120	0.92	0.87	0.73
130	0.95	0.90	0.76
140	0.98	0.93	0.79
150	1.01	0.96	0.81
160	1.05	0.99	0.84
170	1.08	1.03	0.87
180	1.11	1.06	0.90
190	1.14	1.09	0.93
200	1.18	1.12	0.96
250	1.34	1.28	1.10
300	1.51	1.44	1.24
400	1.83	1.76	1.50
500	2.15	2.06	1.71
600	2.46	2.36	2.02
700	2.76	2.65	2.27
800	3.06	2.93	2.51
900	3.35	3.21	2.75
1000	3.64	3.49	2.98
1250	4.35	4.17	3.55
1500	5.03	4.82	4.11

Table 2.2: Electron IMFPs from the TPP-2M equation[80] for water, 1 mol/L NaI, and 10 mol/L for electron energies from 65 eV to 1500 eV.

a maximum occurring approximately -0.25 nm from the interface. An enhancement in the potassium density is observed in the depletion layer of the iodide profile, with a maximum number density at approximately -0.7 nm. The densities of both potassium and iodide ions converge to bulk values at about -1.2 nm. In the water density profile, bulk behavior is observed until approximately -0.2 nm, above which it decreases monotonically to zero.

In the instantaneous interface representation (Figure 2.3), a clear structuring in the water and ion density profiles is observed near the interface. The water density exhibits two pronounced
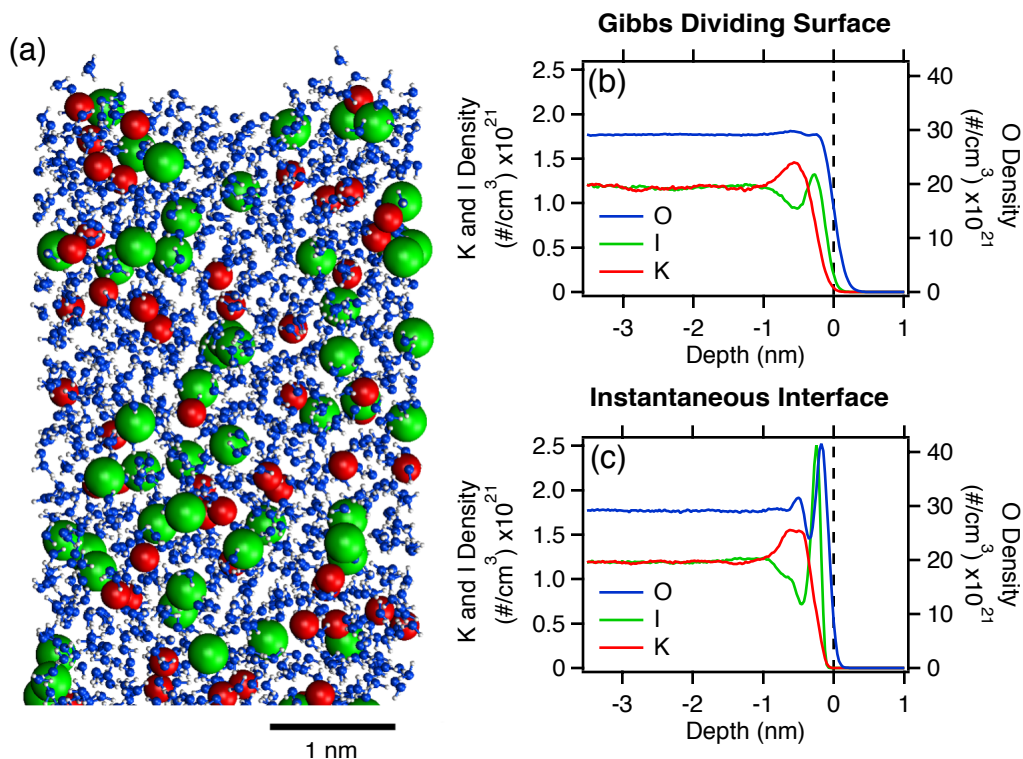
Figure 2.3: Molecular dynamics (MD) simulation results. (a) Snapshot (side view) of an equilibrated simulation of 2 mol/L KI. The solution/vapor interface is at the upper end of the image. Red: potassium cations. Green: iodide anions. Blue/white: water molecules. (b) Atomic density profiles using the Gibbs dividing surface (GDS) definition of the interface. (c) Same as in (b) except with the instantaneous definition of the interface. Note that both (b) and (c) are derived from the same simulation of the system shown in (a).

layers with density maxima at -0.1 nm and -0.6 nm from the interface, respectively. A significant enhancement in the iodide density occurs just behind the first water peak, at -0.15 nm. Potassium density fills the depletion layer following the iodide enhancement, with the enhancement spanning the region between -0.4 and -0.7 nm into the solution. Bulk behavior is reached at approximately -1.5 nm. The instantaneous interface gives a more structurally detailed view of the density of each species. In the GDS representation, much of the water and ion structure is averaged out over the thermal fluctuations in the position of the interface.

2.3.4   Input of MD Atom Density Profiles as the SESSA Sample Geometry

SESSA requires a layer-by-layer description of the aqueous solution starting with the bulk and going towards the vapor (or vacuum) interface. There are no restrictions on the number of allowed layers, or on the thickness of each layer. In the present case, we use the atomic-density profiles obtained from MD simulations as input for the sample geometry required by SESSA with an assumed atomically flat (smooth) interface. In order to decrease the length of the command line input in SESSA, the MD density profiles are coarse grained into wider bins, the smallest of which is 0.05 nm. Each layer (composition and thickness) is tabulated in Table 1.3 of the supplementary material.[107] Figure 2.4(a) shows the input atom density profiles for 2 mol/L KI using the GDS definition of the interface for each layer included in SESSA. Note the overall similarity with the MD profiles of Figure 2.3(b). The corresponding atom density profiles for the instantaneous interface are shown in Figure 2.4(b) (compare with Figure 2.3(c)). The bulk solutions in both cases are modeled as semi-infinite slabs with densities and compositions averaged from the innermost 1.5 nm of the MD simulations. Twenty-one layers are used in both the Gibbs dividing surface and the instantaneous definitions of the interface. Using bin sizes of half the thicknesses in Table 1.3 yields no change in the SESSA simulation results; however, doubling the bin size results in an atom density profile that visibly differs from that of the MD simulations and results in non-negligible changes in the SESSA results (not shown and the results are not discussed herein).
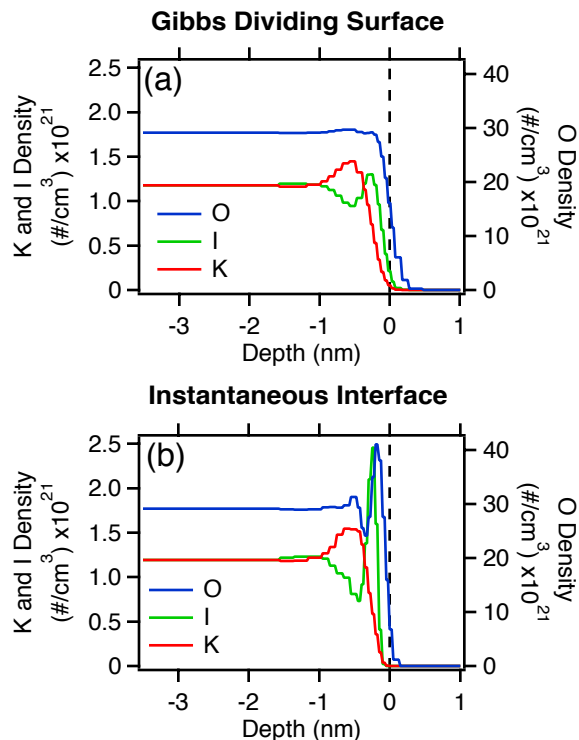
Figure 2.4: Layer-by-layer atom densities used as SESSA sample input for 2 mol/L KI. (a) Gibbs dividing surface (GDS) definition of the interface (compare with Figure 2.3(b)). (b) Instantaneous definition of the interface (compare with Figure 2.3(b)). Red: Potassium. Green: Iodide. Blue: Oxygen.

2.3.5 SESSA Simulation Results

Ratios of peak intensities of 2 mol/L KI from SESSA simulations, normalized in each case by the ratio of atomic photoionization cross sections, are shown in Figure 2.5 for both the GDS (black open diamonds) and instantaneous (red closed circles) definitions of the interface as a function of energy (increasing probe depth). We show ratios of the I 4d to K 2p intensities in Figure 2.5(a), ratios of the I 4d to O 1s intensities in Figure 2.5(b), and ratios of the K 2p to O 1s intensities in Figure 2.5(c). Identical results were obtained from corresponding ratios with the I 3d, K 3p, and O 2s peak intensities.

Figure 2.5 shows the calculated anion-to-cation (I 4d/K 2p) ratio as a function of energy (probe depth). Only minor differences are evident between the two definitions of the in-

terface. At low energies, where the simulation is most sensitive to the composition of the outmost layers of solution, the iodide concentration is enhanced relative to that of potassium, consistent with the density profiles computed directly from the MD simulations shown in Figure 1.3. This preferential enrichment of iodide (relative to potassium) at the vapor (vacuum)-water interface is now well established by numerous computational and experimental studies,[23] although the driving forces for ion adsorption to the interface are still being debated.[22] The SESSA simulations predict a maximum enhancement in the I 4d/K 2p ratio of 16 % (for a photoelectron energy of 65 eV) based on the atom-density profiles from the MD simulations. This enhancement decreases monotonically with increasing energy until an asymptotic I 4d/K 2p ratio of 1.01 is reached at ≈ 800 eV. At higher energies, the ratio remains constant.

Figures 1.5(b) and 1.5(c) show the ion-to-oxygen atomic ratios, I 4d/O 1s and K 2p/O 1s, respectively. The O 1s signal is representative of water. In these ratios, pronounced differences between the two definitions of the interface are evident. In all cases, the ion-to-water ratios decrease relative to their bulk value at 1500 eV as the energy is decreased. This result suggests that, on a relative scale, the concentration of ions near the solution- vapor (or vacuum) interface, for the ID of the chosen experimental conditions (cf. Figure 2.1), is depleted relative to that in the bulk. This finding seems, at least qualitatively, at odds with the atom-density profiles of Figure 2.3 where the maximum ion concentrations near the interface peak at densities that exceed those in the bulk. One would perhaps naively expect this ion distribution to manifest itself as an increase in the I 4d/O 1s and K 2p/O 1s ratios as the interface sensitivity of the simulation is increased, not a decrease. This expectation would, however, be at odds with the measured positive surface tension increment of 2 mol/L KI.[68] The latter result is explained thermodynamically by a net depletion of ions over the entire interfacial length of the system.[108] The interfacial length is defined as the depth over which the ion and water density profiles differ from bulk (-1.2 nm for the GDS and -1.5 nm in the instantaneous definition, see Section 1.3.3). A simple integration of the density profiles

of Figure 2.3 confirms a net decrease in the ion concentrations over the interfacial lengths. The SESSA simulations capture this decrease.

The more pronounced decrease in the ion to oxygen ratios for the GDS is rationalized qualitatively by analyzing the relative ion depletions between the two interface definitions. In the GDS definition, I^- and K^+ concentrations are depleted (over the -1.2 nm interfacial length) relative to the bulk by 10.6 % and 8.8 %, respectively, whereas the depletions are 8.2 % and 8.4 %, respectively, for the instantaneous definition. These differences are captured by the SESSA simulations, which predict lower signal intensities for the GDS than the instantaneous interface definition of the interface (Figures 1.5(b) and 1.5(c)), however, they are small and may be difficult to reproduce in an XPS experiment at a liquid interface.
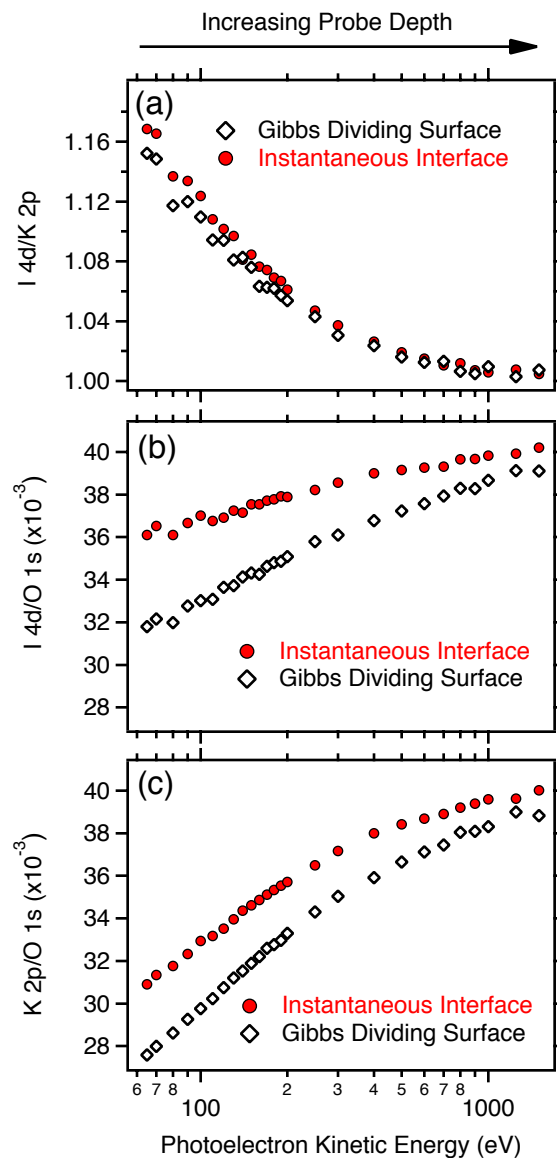
Figure 2.5: SESSA simulation results of peak-intensity ratios, normalized in each case by ratios of atomic photoionization cross sections, for 2 mol/L KI. (a) I 4d/K 2p ratio. (b) I 4d/O 1s ratio. (c) K 2p/O 1s ratio. Red circles: Instantaneous definition of the interface. Black diamonds: Gibbs dividing surface definition of the interface.

2.3.6   Comparison of SESSA Results with Other Approaches

SESSA is not unique in its ability to calculate XPS signal intensities using atom-density profiles from MD simulations, although it does offer several distinct advantages over the

more traditional convolution-integral approach employed by Brown et al.[41] and Ottosson et al.[46] Here we describe the latter approach and subsequently make a direct comparison with results from SESSA simulations using as example an aqueous solution of 1 mol/L NaI where the density profiles are computed from a MD simulation using the instantaneous definition of the interface.[107]

The XPS signal of atom n can be calculated from MD simulations by integrating the atomic density profile according to[87]

$$I_n(E) = \int_0^{+\infty} \rho_n(z)dz + \int_{-\infty}^0 \rho_n(z)e^{-z/\lambda(E)}dz \tag{2.2}$$

where $I_n(E)$ is the XPS signal intensity of the n-th species at the photoelectron kinetic energy E, is the density profile of atom n (from the MD simulations), and is the distance from the interface. The integration limit of zero defines the position of the interface. The first integral in Eq. 2.2 accounts for the vapor (vacuum)-side of the interface where the total atomic density is low and the electron IMFP term is assumed to vanish: the probability of a photoelectron in this region to undergo an inelastic scattering event is assumed to be zero. The second integral in Eq. 2.2 accounts for the solution side of the interface. Here photoelectrons have a non-negligible probability to undergo an inelastic scattering event, and the intensity is attenuated with a probability governed by the IMFP. The effects of elastic scattering are neglected in Eq. 2.2.[87]

The results of performing the integrations of Eq. 2.2 using the I and Na^+ atom-density profiles from the MD simulation of 1 mol/L NaI are shown in Figure 2.6 (solid blue line). The calculated XP intensities were normalized by the corresponding atomic photoionization cross sections, as before, to give the anion-to-cation ratio, I/Na. The abscissa in Figure 2.6

has been converted to photoelectron energy using the relation between λ and energy provided by the TPP-2M formula for this solution (see Figure 2.2, Table 2.2). The corresponding ratios from the SESSA simulations are also shown in Figure 2.6 (solid green circles). Pronounced differences in the predicted ion ratios are seen for energies below ≈ 300 eV, with the SESSA ratios systematically higher than those from Eq. 2.2. At an energy of 65 eV (where the IMFP is 0.72 nm), a maximum difference of about 12 % is observed.
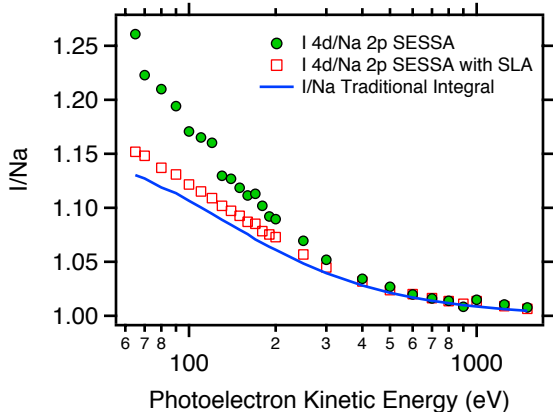
Figure 2.6: Iodide-to-sodium ratio in 1 mol/L NaI. Green circles: SESSA simulation results (I 4d/K 2p) using atomic-density profiles computed from MD simulations using the instantaneous definition of the interface. Red squares: SESSA simulation results (I 4d/K 2p) in the straight-line approximation (elastic scattering turned off). Solid blue line: Iodide-to-potassium ratio calculated using Eq. 2.2.

The effect of neglecting elastic scattering events in Eq. 2.2 can be demonstrated by repeating the SESSA simulations in the straight-line approximation (SLA) where elastic-scattering events are turned off. While these events cannot be turned off in an experiment, it is nonetheless useful here for comparing different theoretical approaches. The results from SESSA simulations with the SLA are shown in Figure 2.6 as open red squares. The maximum difference between the Traditional Integral and SESSA with SLA results is reduced to a mere 2 %, and this indicates that elastic scattering for this solution may be significant for energies below ≈ 300 eV.

Other differences between the traditional-integral approach and SESSA are more difficult

to quantify and likely account for the remaining 2 %. For instance, each layer in Eq. 2.2 is assumed to have the same IMFP (as for the bulk of the solution). In SESSA, the IMFP is explicitly calculated for each layer of the solution and we find that IMFPs vary for the near-surface layers (for this 1 mol/L NaI solution) by up to 16 % from the bulk values. Specifically, for an energy of 65 eV, the TPP-2M formula predicts an IMFP of 0.83 nm for the layer at a depth of -0.1 nm and 0.72 nm in the bulk.
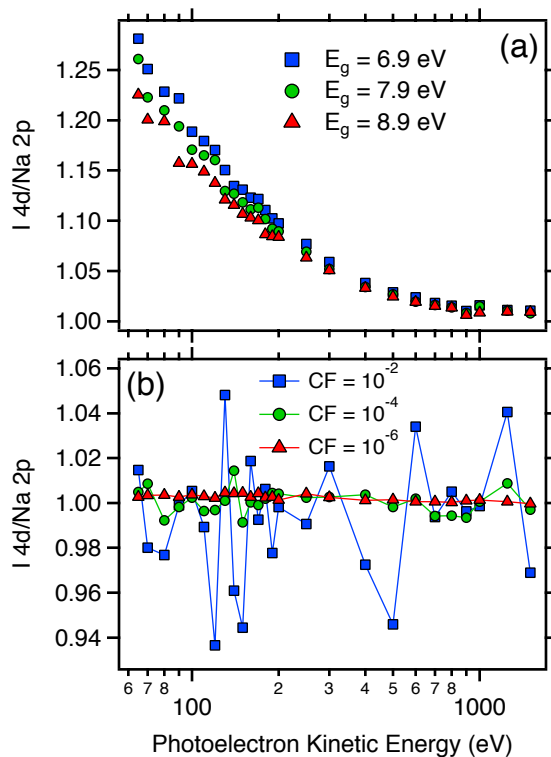
Figure 2.7: Band gap (E_g) and convergence factor (CF) dependencies. (a) SESSA simulated I 4d/Na 2p ratios as a function of photoelectron energy for band-gap energies of 6.9 eV (blue squares), 7.9 eV (green circles), and 8.9 eV (red triangles). The simulations were performed for 1 mol/L NaI using the density profiles from MD simulations. (b) SESSA simulated I 4d/Na 2p ratios as a function of energy for convergence factors of 10^{-2} (blue squares), 10^{-4} (green circle), and 10^{-6} (red triangles). The system is a semi-infinite structureless slab of 1 mol/L NaI.

2.3.7   Technical Considerations for SESSA

The band-gap energy (E_g) of the solution is a required input in SESSA for calculation of the IMFP from the TPP-2M equation. In the above SESSA simulations, Eg was assumed to be constant, 7.9 eV. We note, however, that E_g values for water in the literature vary by about $\pm$ 1 eV,[109,110,111,112] roughly centered around 7.9 eV. Databases for band-gap energies of aqueous electrolyte solutions do not exist. In order to quantify the influence of the solution band-gap energy on the SESSA results, we have carried out additional simulations for 1 mol/L NaI using the instantaneous definition of the interface and Eg values of 6.9 eV, 7.9 eV (as for the previous results) and 8.9 eV. Figure 2.7(c) shows plots of the I 4d/Na 2p atomic ratios (derived in the same way as those in Figure 2.6) as a function of photoelectron energy. Differences in the I 4d/Na 2p ratios do arise for energies below $\approx$200 eV; however, these differences are small, with variations of only $\pm$ 3 % from the results for the $E_g = 7.9$ eV simulation.

The convergence criterion for the SESSA simulation is a user-defined setting. Using a semi-infinite slab of 1 mol/L NaI, the effect of the convergence factor (CF) on the simulated I 4d/Na 2p ratios was assessed (Figure 2.7(b)). We find that CFs larger than 10^{-6} are insufficient to provide a satisfactory level of statistical accuracy ($< 0.5\%$ from the stoichiometric ratio). This level of accuracy is not without computational expense: the series of simulations needed to construct the data set in Figure 2.7b with a CF of 10^{-6} required about 13 minutes (on a personal laptop computer), whereas a CF of 10^{-4} required only 1 minute. Simulating an entire 21-layer system, as was done for Figure 2.5, took $\approx$ 45 minutes with a CF of 10^{-6}.

2.4 Conclusions

A straightforward and systematic protocol that uses SESSA for the direct interpretation of MD simulations with XPS signal intensities was presented. Using the TPP-2M predictive formula, the electron IMFP was calculated as a function of photoelectron kinetic energy and shown to depend on solution composition, varying by up to 30 % at 65 eV between pure water and 10 mol/L NaI. The information depth, or surface sensitivity, of the experiment for different photoelectron kinetic energies was calculated using pure water as an example. Even at the lowest kinetic energies routinely employed in XPS experiments from aqueous solutions, 65 eV, the outermost monolayer of solution is responsible for less than half of the total signal intensity. The expected ion signal intensity ratio (I/K) and ion-to-water signal intensity ratios (I/water and K/water) for 2 mol/L KI were calculated as a function of photoelectron kinetic energy. The corresponding ion ratio for 1 mol/L NaI is compared with that obtained from an ad hoc integral approach widely used within the community. The SESSA results show that the traditional approach for calculating XPS signal intensities from MD atom-density profiles systematically underestimates the preferential enhancement of the anion (over the cation) at the vapor (vacuum)-aqueous electrolyte interface. This difference can be primarily traced to the neglect of elastic-scattering events in the traditional approach.

SESSA is straightforward to use and shows promise for enabling quantitative comparisons between energy- dependent X-ray photoelectron spectroscopy signal intensities and the results of MD simulations. In on-going work, we are carrying out a systematic comparison of MD/SESSA simulation results with experimental data on a variety of aqueous salt solutions.

| Layer | Layer width | I$^-$ fraction | K$^+$ fraction | H$_2$O fraction | Total density |
#	(nm)	%	%	%	(# / cm^3)
1	0.2	0.00	0.00	100.0	6.92×10^{20}
2	0.1	0.03	0.00	99.97	5.55×10^{21}
3	0.1	0.12	0.02	99.86	1.82×10^{22}
4	0.05	0.26	0.06	99.68	3.48×10^{22}
5	0.05	0.44	0.11	99.46	4.86×10^{22}
6	0.05	0.64	0.17	99.18	6.28×10^{22}
7	0.05	0.90	0.27	98.83	7.49×10^{22}
8	0.05	1.15	0.41	98.44	8.36×10^{22}
9	0.05	1.34	0.60	98.06	8.81×10^{22}
10	0.05	1.45	0.83	97.72	8.96×10^{22}
11	0.05	1.45	1.07	97.49	8.96×10^{22}
12	0.05	1.34	1.26	97.40	8.94×10^{22}
13	0.1	1.15	1.47	97.39	9.02×10^{22}
14	0.1	1.03	1.58	97.39	9.15×10^{22}
15	0.1	1.07	1.56	97.37	9.16×10^{22}
16	0.1	1.17	1.49	97.35	9.11×10^{22}
17	0.1	1.24	1.41	97.35	9.06×10^{22}
18	0.1	1.29	1.36	97.35	9.01×10^{22}
19	0.2	1.32	1.32	97.36	8.98×10^{22}
20	0.4	1.33	1.30	97.37	8.97×10^{22}
Substrate	Semi-infinite	1.31	1.31	97.38	8.98×10^{22}

Table 2.3: SESSA input parameters for 2 mol/L KI using the GDS interface.

2.5 Supplementary Material

| Layer | Layer width | I^- fraction | K^+ fraction | H_2O fraction | Total density |
#	(nm)	%	%	%	(# / cm^3)
1	0.85	0.00	0.00	100.00	2.78×10^{19}
2	0.1	0.00	0.00	100.00	3.53×10^{21}
3	0.05	0.00	0.00	100.00	2.05×10^{22}
4	0.05	0.00	0.01	99.99	4.78×10^{22}
5	0.05	0.02	0.04	99.93	8.29×10^{22}
6	0.05	0.35	0.13	99.52	1.15×10^{23}
7	0.05	1.28	0.29	98.43	1.25×10^{23}
8	0.05	2.28	0.55	97.17	1.08×10^{23}
9	0.05	2.45	0.97	96.59	8.57×10^{22}
10	0.05	1.84	1.48	96.68	7.49×10^{22}
11	0.05	1.17	1.73	97.11	7.90×10^{22}
12	0.05	0.81	1.68	97.51	9.03×10^{22}
13	0.1	0.84	1.60	97.56	9.62×10^{22}
14	0.1	1.08	1.68	97.23	9.18×10^{22}
15	0.1	1.15	1.63	97.21	9.05×10^{22}
16	0.1	1.24	1.47	97.28	9.08×10^{22}
17	0.1	1.33	1.40	97.27	9.06×10^{22}
18	0.2	1.37	1.36	97.26	8.96×10^{22}
19	0.2	1.38	1.33	97.30	8.93×10^{22}
20	0.2	1.36	1.32	97.32	8.94×10^{22}
Substrate	Semi-infinite	1.33	1.33	97.35	8.98×10^{22}

Table 2.4: SESSA input parameters for 2 mol/L KI using the instantaneous interface.

Layer	Layer width	I$^-$ fraction	K$^+$ fraction	H$_2$O fraction	Total density
#	(nm)	%	%	%	(# / cm^3)
1	0.37	0.00	0.00	100.00	7.83×10^{19}
2	0.1	0.00	0.00	100.00	4.00×10^{21}
3	0.07	0.00	0.00	100.00	2.82×10^{22}
4	0.07	0.01	0.00	99.99	7.59×10^{22}
5	0.05	0.19	0.00	99.77	1.17×10^{23}
6	0.05	0.73	0.04	99.14	1.28×10^{23}
7	0.05	1.32	0.13	98.37	1.12×10^{23}
8	0.05	1.40	0.31	98.08	9.05×10^{22}
9	0.05	1.02	0.52	98.29	8.00×10^{22}
10	0.05	0.64	0.69	98.64	8.42×10^{22}
11	0.07	0.41	0.72	98.90	9.67×10^{22}
12	0.07	0.42	0.68	98.83	1.00×10^{23}
13	0.1	0.48	0.75	98.58	9.61×10^{22}
14	0.1	0.50	0.93	98.62	9.47×10^{22}
15	0.1	0.53	0.88	98.70	9.53×10^{22}
16	0.1	0.58	0.77	98.67	9.51×10^{22}
17	0.1	0.63	0.74	98.67	9.42×10^{22}
18	0.7	0.65	0.70	98.72	9.39×10^{22}
19	0.6	0.63	0.63	98.76	9.40×10^{22}
20	0.4	0.60	0.63	98.78	9.43×10^{22}
Substrate	Semi-infinite	0.61	0.61	98.79	9.42×10^{22}

Table 2.5: SESSA input parameters for 1 mol/L NaI using the instantaneous interface.
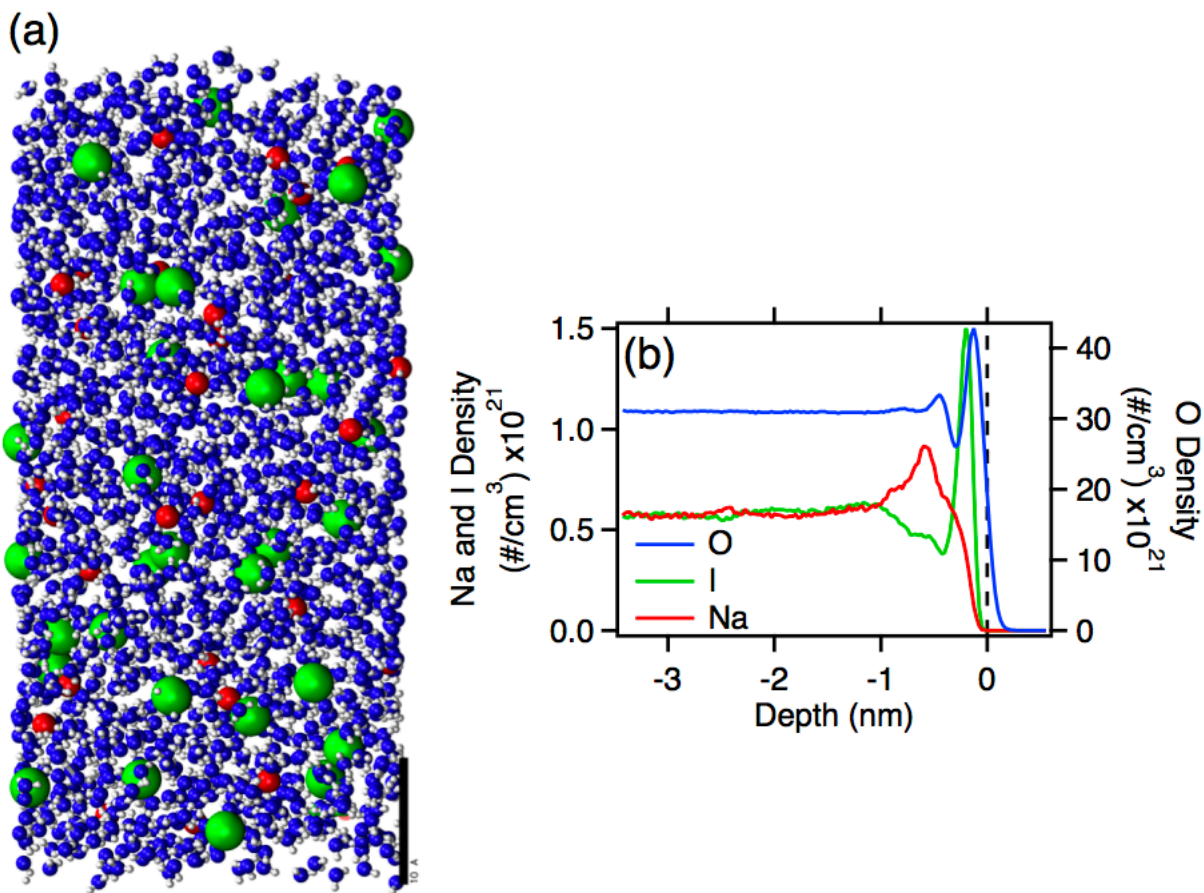
Figure 2.8: Molecular dynamics (MD) simulation results. (a) Snapshot (side view) of equilibrated simulation of 1 mol/L NaI. The solution/vapor interface is at the upper end of the image. Red: sodium cations. Green: iodide anions. Blue/white: water molecules. (b) Atomic density profiles using the instantaneous interface definition of the interface.

Chapter 3

Specific Anion Effects on Na$^+$ Adsorption at the Aqueous Solution Air Interface: MD Simulations, SESSA Calculations and Photoelectron Spectroscopy Experiments

---

3.1 Introduction

The chemistry and physics of many aqueous electrolyte interfaces are governed by the physical distribution of ions within a few molecular layers of the solution surface. Often subtle changes to these distributions, brought about, for example, by changing the identity of the ion (specific ion effects), can have profound implications on the structure and reactivity of aqueous interfaces.[12,13,14,15,16,17,18,19] Molecular dynamics (MD) simulations have the potential to accurately describe, and ultimately predict, atom distributions at aqueous electrolyte interfaces.[23,59] In order, however, to validate the performance of the force fields used in MD simulations, a direct comparison of the predicted atom distributions against those measured experimentally is required. Unfortunately, the depth-resolved molecular-level atom distributions afforded by MD simulations are nontrivial to interpret as physical observables of spectroscopy and, therefore, no direct validation has been reported to date. This inability to directly validate the force fields of MD simulations against $interface - specific$ spectroscopy ultimately limits their predictive power for more complex interfaces that are, at present, beyond the scope of interrogation by state-of-the-art experiment.

The air-water interface (AWI) is ubiquitous in environmental and atmospheric sciences, and the distribution of halide ions (I^-, Br^-, Cl^-, and to a lesser extent F^-) at this interface is well documented to deviate from those predicted by dielectric continuum theory.[113] In general, as the size of the anion increases, so does its propensity to segregate to the interface.[23,114] To some degree, counter-ion effects can modify the surface behavior of the anions via ion-ion and ion-water interactions, but the extent of these effects are not well-known as much less attention has been devoted to the spatial distribution of the cations in alkali halide solutions.[114,106,115] This is, in part, because the interfacial chemistry of sea salt aerosols is driven primarily by reactions involving halide ions,[12,35,116] but also because the variations in spatial distributions of the cations (such as Na^+ or K^+) as the halide ion is exchanged (specific

anion effects) are predicted by MD simulations to be substantially less pronounced than the differences between different halide ions (for a given cation). Accurately predicting these differences in cation distributions at the AWI is a formidable challenge to MD simulations.

Here, for the first time, we show that the relative sodium ion (Na^+) populations predicted by MD simulations at the AWI of solutions of NaCl, NaBr and NaI are in quantitative agreement with those measured by photoelectron (PE) spectroscopy when a particular non-polarizable force field is employed in the simulations. Predictive PE signal intensities are generated from the atom-density profiles of MD simulations using the Simulation of Electron Spectra for Surface Analysis (SESSA) software[88,89] of the National Institute of Standards and Technology (NIST) and compared directly to the results of PE spectroscopy experiments using a liquid jet. Interpreting the density profiles of MD simulations as physical observables of spectroscopy[1] permits direct comparison with experiment and, thus, should enable a convenient benchmark by which force fields can be validated, enabling a paradigm shift towards quantitative descriptions of the AWI. We demonstrate this capability by showing that a polarizable force field employed in previous studies of the AWI of sodium halide solutions predicts ion distributions near the interface that deviate substantially from those inferred from PE spectroscopy.

3.2 Methods and Materials

3.2.1 Non-polarizable force field-based MD simulations.

MD simulations of nominal concentrations of 0.7 and 1 M NaI, NaBr and NaCl systems are performed using the GROMACS simulation suite[64] by placing 1728 water and 22 ion pairs and 32 ion pairs, respectively, into a 30 Å × 30 Å × 140 Å simulation cell. Periodic boundary conditions are applied in all three dimensions. The temperature is held

Atom	q (e$^-$)	σ (Å)	ϵ (kJ/mol)
O	-0.8476	3.166	0.65
H	+0.4238	-	-
Na$^+$	+1.0	2.234	0.65
I$^-$	-1.0	5.014	0.985
Br$^-$	-1.0	4.834	0.2106
Cl$^-$	-1.0	4.394	0.416

Table 3.1: Charges (q) and Lennard-Jones parameters (σ and ϵ), used in the non-polarizable force field-based molecular dynamics simulations.

constant at 298 K using a Berendsen thermostat with an additional stochastic term that ensures the correct kinetic energy distribution.[94] The 0.7 M simulations are run for at least 80 ns, and the 1 M simulations for at least 100 ns. The water molecules are modeled using the SPC/E water model,[66] and the non-polarizable parameters developed by Horinek et al.[60] are used for the ions. The force field parameters used for the non-polarizable simulations are tabulated in Table 3.1. Electrostatic interactions are calculated using the smooth particle mesh Ewald method,[95] and a cutoff of 0.9 nm is used for the real-space part of the Ewald sum and the Lennard-Jones interactions. The SETTLE[96] algorithm is used to keep the water molecules rigid. Actual concentrations calculated by integrating atomic density profiles over a portion of the bulk region of the non-polarizable simulations are as follows: $[\text{I}^-]_{NaI,0.7M} = [\text{Na}^+]_{NaI,0.7M} = 0.71$M; $[\text{Br}^-]_{NaBr,0.7M} = [\text{Na}^+]_{NaBr,0.7M} = 0.75$ M; $[\text{Cl}^-]_{NaCl,0.7M} = [\text{Na}^+]_{NaCl,0.7M} = 0.78$ M; $[\text{I}^-]_{NaI,1M} = [\text{Na}^+]_{NaI,1M} = 1.00$ M; $[\text{Br}^-]_{NaBr,1M} =[\text{Na}^+]_{NaBr,1M} = 1.06$ M; $[\text{Cl}^-]_{NaCl,1M} = [\text{Na}^+]_{NaCl,1M} = 1.11$ M.

3.2.2   Polarizable force field-based MD simulations.

Polarizable MD simulations of ~1 M NaI, NaBr and NaCl are performed using the Amber 8 simulation package.[117] For the NaBr and NaI solutions, 36 ion pairs and 1728 water molecules are placed into a 30 Å × 30 Å × 180 Å simulation cell. For the NaCl solution, 144 ion pairs and 6912 water molecules are placed into a 60 Å × 60 Å × 180 Å simulation cell. The

Atom	q (e$^-$)	σ (Å)	ϵ (kJ/mol)	α (Å^{-3})
O	-0.7300	1.7980	0.6530	0.528
H	+0.3650	0.000	0.000	0.170
Na$^+$	+1.0	2.3501	0.5439	0.25
I$^-$	-1.0	5.15	0.4184	6.90
Br$^-$	-1.0	4.603	0.4184	4.533
Cl$^-$	-1.0	4.3105	0.4184	3.25

Table 3.2: Charges (q), Lennard-Jones parameters (σ and ϵ), and polarizabilities (α) used in the polarizable force field-based molecular dynamics simulations.

polarizable POL3 water force field is adapted from Ref. 118. The Na$^+$ and Cl$^-$ parameters are adapted from Ref.58, Br$^-$ from Ref. 119, and I$^-$ from Ref. 120. The force field parameters used for the polarizable MD simulations are tabulated in Table 3.2. The temperature is held constant at a temperature of 300 K using a Berendsen thermostat.[121] The smooth particle mesh Ewald summation[95] is used to compute the electrostatic interactions, and the SHAKE[122] algorithm is used to keep the water molecules rigid. A cutoff of 12 Å is used for the van der Waals interaction and the real part of the Ewald sum. Trajectories for the NaI, NaBr, and NaCl solutions are run for at least 3 ns. Concentrations are calculated by integrating atomic density profiles over the bulk region of the solutions and are as follows: $[\text{I}^-]_{NaI} = 0.963$ M, $[\text{Na}^+]_{NaI} = 0.916$ M; $[\text{Br}^-]_{NaBr} = 1.155$ M, $[\text{Na}^+]_{NaBr} = 1.221$ M; $[\text{Cl}^-]_{NaCl} = 1.226$ M, $[\text{Na}^+]_{NaCl} = 1.287$ M.

3.2.3   Instantaneous interface.

As described in previous works,[1,63] all MD simulation results are referenced to the instantaneous solution-air interface. The first step in defining the instantaneous interface is to construct a coarse-grained density field, as described in Ref. 20, by convoluting three-dimensional Gaussians on to the atomic coordinates r, with scaling factor, η, and Gaussian

Atom	ξ (Å)	η
O	2.4	1.0
H	0.0	0.0
Na$^+$	0.0	0.0
I$^-$	2.7	3.35
Br$^-$	2.55	0.477
Cl$^-$	-0.0	0.0

Table 3.3: Instantaneous interface convolution parameters.

half-width of ξ:

$$\phi(r; \eta, \xi) = \frac{\eta}{(2\pi\xi^2)^{3/2}} exp \left(\frac{-r^2}{2\xi^2} \right) \tag{3.1}$$

At each time step, the instantaneous interface is found by parsing the density field along the vertical directions (from above and below) to find the location where the density of the solution is half the bulk solution density. The depth of the atom into the solution is defined as the absolute distance between the atom and the nearest interface. The η and ξ parameters used to calculate the coarse-grained density field for both the non-polarizable and polarizable force field-based simulations are listed in Table 3.3.

3.2.4 SESSA simulations.

PE signal intensities are simulated using the SESSA software package developed by Werner et al.[88] SESSA is a NIST standard reference database[89] that contains all data needed for quantitative simulations of PE and Auger-electron spectra. Data retrieval is based on an expert system that queries the databases for each needed parameter. SESSA provides the spectral shape of each photoelectron peak using a model of signal generation in PE spectroscopy that includes multiple inelastic and elastic scattering of the photoelectrons.

In order to minimize the computation time, an efficient Monte Carlo code is employed based on the trajectory-reversal method. In contrast to conventional Monte Carlo codes where electrons are tracked based on their trajectories from the source to the detector, the trajectory-reversal approach tracks electrons in the opposite direction, starting from the detector and working back to the point of origin. Thus, all electrons contribute to the signal, which results in significantly decreased simulation times.

For the SESSA simulations reported herein, the orientation of the analyzer axis is perpendicular to the photon source, while the sample surface is oriented parallel to the analyzer axis. The excitation source is a 100% linearly polarized beam. The polarization vector is rotated 54.7° from the analyzer detection axis, which corresponds to the so-called magic angle in which the PE intensity is independent of the emission angle. Since we are simulating synchrotron-based experiments in which the photon beam is focused in a relatively small area, the illuminated area on the sample is independent of the emission angle. The analyzer acceptance angle is set at ± 22°.

The AWI is modeled as an atomically flat interface (average emission angle = 0°) following the finding of our recent work,[123] which revealed that the jet curvature has a negligible effect on the ion intensity ratio. The atomic-density profiles obtained from MD simulations are used as input for the sample geometry after coarse graining them into wider bins since the number of possible layers in SESSA is limited to 54. The bulk solutions are modeled as semi-infinite slabs with density and composition averaged from the innermost 1.5 nm of the MD simulations. Each layer of the solutions is modeled as being amorphous in structure and any anisotropy that may be present in the solutions cannot be accounted for by SESSA.

Other details of the SESSA simulations have been discussed previously.[1] A convergence factor of 10^{-6} is used for all simulations and the Mott approximation for elastic- scattering effects is assumed. The band gap of the electrolyte solutions is 7.9 eV. The SESSA simulations employ electron IMFPs calculated via the semi-empirical TPP-2M formula of Tanuma

et al.[80] The calculated IMFPs, which depend on the material density, atomic or molecular mass, number of valence electrons per atom or molecule, and the band gap energy, are expected to have uncertainties of about 10%, although the uncertainty could be larger for a small number of materials. The photon energy of the simulations set to 122 eV, the same as used in the experiments, and yields to a simulated kinetic energy of 82.6 eV and 82.5 eV for the Na $2p_{1/2}$ and Na $2p_{3/2}$ respectively (the spin orbit splitting is not resolved in the experiment) relative to the Fermi energy. The 4 eV difference between the Na 2p simulated value and the measured one ($\sim$86.5 eV) corresponds roughly to the work function of the analyzer.[123]

3.2.5   Photoelectron (PE) spectroscopy.

The PE spectroscopy measurements reported herein are performed to the SIM beamline of the SLS (Swiss Light Source) using a liquid jet[124] and the NAPP (Near-Ambient Pressure Photoemission) endstation. A detailed description of this endstation is given elsewhere.[125, 100] In the experimental chamber the direction of the liquid jet flow, the axis of the photoelectron analyzer and the direction of the photon beam are mutually orthogonal. The photon beam has a linearly horizontal polarization, i.e. the polarization axis is parallel to the axis of the analyzer, and a spot size of approximately 100 (h) $\times$ 250 (v) μm.[126] All experiments are performed in vacuum ($\sim$1 $\times$ 10^{-4} mbar). The liquid jet is expanded to hit a liquid N2 trap where it freezes immediately while the measurement chamber is continuously pumped by a turbo molecular pump (Agilent TwisTorr 700). Experiments are performed using a 19 m liquid jet operating at 279 K with a flow rate of 0.35 mL/min. The entrance cone of the Scienta hemispherical analyzer has an aperture of 0.5 mm with a working distance to the surface of the liquid microjet of 0.5 mm. The analyzer is operated at 50 eV pass energy in steps of 100 meV. Aqueous solutions of 0.75 M NaCl, NaBr and NaI and 0.05 M KCl are prepared by dissolving commercial salts (Sigma Aldrich) in Milli-Q water. The photon

energy of the beamline is set at 122 eV to collect the Na 2p peak at $\sim$86.5 eV relative to the vacuum level of the analyzer.

3.3 Results and Discussion

3.3.1 Atom density profiles from non-polarizable MD simulations.

The bulk-normalized atom density profiles obtained from non-polarizable MD simulations of 0.7 M (nominal concentration) aqueous solutions of NaCl, NaBr, and NaI are shown in Figure 3.1 with respect to the instantaneous AWI at nm. To a depth of approximately -1.5 nm into the solution (the interfacial length, IL), the density profiles of all constituents from all three solutions are structured. At larger depths the density profiles are flat, as expected in the bulk region of the solutions. Consistent with previous studies,[23,59] the density profiles predict that Cl^-, Br^-, and I^- are all present in the topmost layer of the solution, with populations increasing in the order $Cl^- < Br^- < I^-$. In contrast to early studies employing polarizable force fields that predict Br^- and I^- are both enhanced at the AWI,[59,127,24,46] Figure 3.1 reveals that only I^- is enhanced at the AWI when the non- polarizable force field of Horinek et al.[60] is used. The Na^+ population is enhanced (compared with the bulk) in the region beneath the surface anion layer. The magnitude of the Na^+ enhancement and its distribution in the subsurface layer depends on the identity of the anion. Integrating the Na^+ density profiles over the IL of -1.5 nm gives surface densities of 0.592 nm^{-2} for NaI, 0.574 nm^{-2} for NaBr (97% of that in NaI), and 0.560 nm^{-2} for NaCl (95% of that in NaI). While the integrated Na^+ densities deviate by only up to 5% between solutions, it is clear from Figure3.1 that the distributions of Na^+ within the IL depend strongly on the identity of the anion. It is this anion-specific dependence of the Na^+ populations near the AWI predicted by these MD simulations that is the focus of this study.
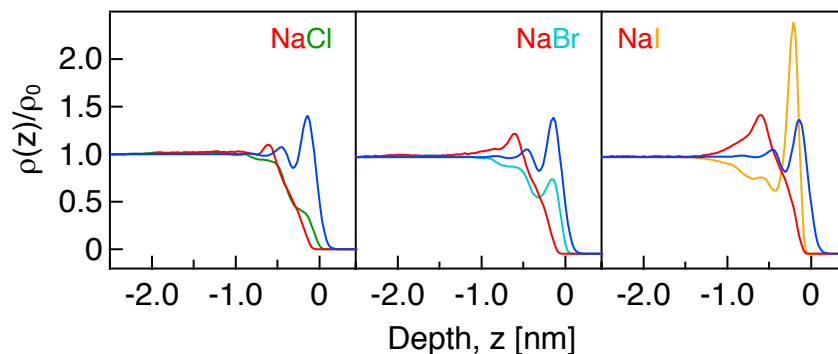
Figure 3.1: Atom density profiles (color coded) from MD simulations of 0.7 M aqueous solutions of NaCl, NaBr, and NaI. The oxygen density profile is shown in blue for all solutions. The instantaneous interface is at z = 0 and negative z indicates depth into the solution.

3.3.2 Interpretation of atom density profiles in terms of a spectroscopic observable.

In order to quantify the anion-specific dependence of the Na^+ density near the AWI predicted by the non-polarizable MD simulations, we use SESSA to simulate the Na 2p photoelectron (PE) intensities from the atom density profiles depicted in Figure 3.1. This additional step (a simulation of a simulation) is required because PE spectroscopy is an integrated technique that exponentially-weights signal from several molecular-layers into the solutions and, therefore, cannot be directly compared with the layer-by-layer molecular description afforded by the MD simulations.[1] The SESSA simulated Na 2p PE intensities at 82.5 eV photoelectron kinetic energy (KE) from the 0.7 M NaBr and NaCl electrolyte solutions relative to that of NaI are shown in Figure 3.2a (open red squares). This KE is chosen because the information depths (IDs), that is the depths into solution over which photoelectrons escape and contribute to the main photoelectron lines of the simulations, are ca. 1.5 nm at this energy for all three solutions (see Supporting Information and Figure 3.7 for calculation details). At this KE the IDs of the SESSA simulations (and the PE experiments, which are performed at the same KE, see next subsection) are essentially the same as the ILs predicted by the

70

MD simulations. Because the IDs are virtually identical for all three solutions investigated herein (photoelectrons are primarily scattered by water at these relatively dilute electrolyte concentrations), the local relative concentration of Na^+ at the AWI can be quantified for the different electrolyte solutions simply by integrating the Na 2p PE signal. The SESSA simulated Na 2p PE intensities decrease in the order. Specifically, our SESSA simulations of the atom density profiles from the non-polarizable force field-based MD simulations shown in Figure 3.1 predict a decrease in the Na^+ 2p photoelectron signal within the ID of 11% (NaBr) and 17% (NaCl) relative to that of NaI. The substantially larger difference between the three solutions from the SESSA predicted intensities and those obtained from simple integration of the MD density profiles over the entire IL (recall NaCl varied by only 5% from NaI) originates from the unique distributions of Na^+ near the AWI, and how each layer contributes to PE intensity. In the following section we evaluate the accuracy of these SESSA predictions by using PE spectroscopy in conjunction with a liquid jet to measure the relative concentration of Na^+ at the AWI for 0.75 M aqueous solutions of NaCl, NaBr, and NaI.

3.3.3 Photoelectron (PE) spectroscopy.

The inner valence region PE spectrum from a 0.75 M aqueous solution of NaI is shown in Figure 3.2b. Spectra of 0.75 M NaBr and NaCl are shown in Figure 3.8. The photon energy, 122 eV, is chosen such that the KE of the Na 2p peak is at ∼86.5 eV (relative to the vacuum level of the analyzer), which corresponds to an ID of 1.5 nm and matches the IL predicted by the MD simulations of Figure 3.1. The NaI spectrum is characterized by components assigned to I 4d5/2 and I 4d3/2, Na 2p and O 2s. The O 2s region of the spectrum is comprised of both liquid and gas phase peaks, but we are unable to resolve the different contributions.14 A straightforward integration of the Na 2p peak is not possible because of its partial overlap with the O 2s peak, and because the complex baseline shape in this region of the spectrum prevents easy background subtraction. In order to accurately
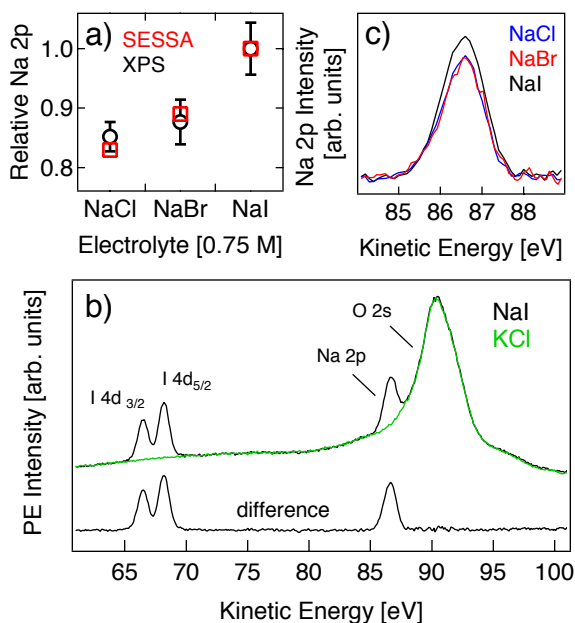
Figure 3.2: (*a*) Red squares: SESSA determined by simulating the Na 2p intensities at 68.5 eV kinetic energy using the atom density profiles from the non-polarizable MD simulations. Black circles: Relative concentration of sodium within the information depth of the XPS experiments performed with an incident photon energy of 122 eV as derived from the integrated area of the Na 2p peaks of *c*). *b* Photoelectron spectra of 0.75 M NaI (black) and 0.05 M KCl (green). The KCl spectrum serves as reference that after subtraction removes the O 2s peak and the sloping background that is characteristic of liquid water. The difference spectrum (lower trace) has a flat background over the entire energy range. *c*) Experimental O 2s background- subtracted Na 2p peaks for 0.75 M NaCl (blue), 0.75 M NaBr (red), 0.75 M NaI (black).

and reproducibly quantify the Na 2p peak area we chose to subtract a reference spectrum of 0.05 M KCl. This spectrum, shown in Figure 3.2b (green trace), contains the same O 2s components as the NaI spectrum but none of the ion specific peaks. The resulting difference spectrum has a remarkably flat background that allows for simple quantification of the Na 2p peak area by integration. The analogous procedure was performed for 0.75 M solutions of NaBr and NaCl. Figure 3.2c shows the background subtracted Na 2p peak for all three solutions. The solution dependent Na 2p integrated peak areas are shown in Figure 3.2a (open black circles) relative to that of the NaI solution. The error bar associated with the relative peak area of each electrolyte solution is the standard deviation of three

different measurements. Our experimental results, within their reproducibility, validate the predictions of the SESSA simulations for the local Na^+ concentration at the AWI based on the atom density profiles provided by the MD simulations of Figure 3.1.
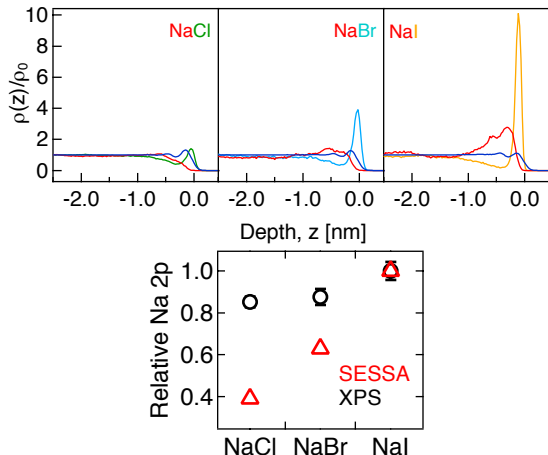
Figure 3.3: (Top) Density profiles from MD simulations of 1 M aqueous NaI, NaBr, and NaCl solutions using polarizable force fields. The oxygen density profile is shown in blue for all solutions. The instantaneous interface is at $z = 0$ depth and negative z-values indicate depth into solution. (Bottom, red triangles) SESSA results determined by simulating the Na 2p intensity at 86.5 eV kinetic energy using the atom density profiles from the polarizable MD simulations.

3.3.4 A comparison of polarizable and non-polarizable force fields.

We now turn to assessing the performance of MD simulations based on a particular type of polarizable force field. Specifically we consider the induced dipole model used in the pioneering studies that first predicted that the heavier halide anions adsorb to the AWI,[23, 59] an observation that had implications for the chemistry for marine aerosol particles in the atmosphere.[12] The atom density profiles from polarizable MD simulations of 1 M (nominal concentration) NaCl, NaBr, and NaI solutions are shown in Figure 3.3 and all display significantly larger surface enhancement of the anions compared to the non-polarizable density profiles (see Figure 3.1). Simulating the Na 2p PE intensities using SESSA with an analogous procedure to that used for the atom density profiles of the non-polarizable MD

Salt	Bulk Concentration	MD	Experiment
NaCl	1.11	2.02	2.31^a
NaBr	1.05	1.35	1.94^b
NaI	1.00	0.84	1.23^c

Table 3.4: Comparison of surface tension increments ($\Delta\gamma$) from non-polarizable MD simulations with experimental measurements. [a] using d($\Delta\gamma$)/dc = 2.08 mN/m or NaCl from Weissenborn and Pugh.[129] [b] using d($\Delta\gamma$)/dc = 1.83 mN/m or NaBr from Weissenborn and Pugh.[129] [c] using d($\Delta\gamma$)/dc = 1.23 mN/m or NaI from Weissenborn and Pugh.[129]

simulations shows that the relative concentration of Na^+ near the AWI form the polarizable MD simulations are not in agreement with the experimental results (bottom panel of Figure 3.3). The polarizable MD models result in predicted Na^+ concentrations for NaCl and NaBr relative to NaI that are far too low. These results reinforce the sensitive nature of SESSA simulations to the atom density profiles used as input.

The comparison of the predicted SESSA Na 2p peak areas with the PE data clearly show that the non-polarizable force field is superior to the polarizable force field in its ability to accurately predict the relative Na^+ concentration at the AWI. The non-polarizable force field employed herein has been shown, by using a combination of single ion potentials of mean force computed from MD simulations in conjunction with Poisson- Boltzmann theory, to reasonably accurately reproduce the experimentally measured concentration dependence of the surface tension increments (STIs) for sodium halide solutions up to 1 M.[60] In Tables 3.4 and 3.5, we compare STIs for 1 M (nominal concentration) NaCl, NaBr, and NaI solutions obtained from non-polarizable and polarizable MD simulations, respectively. Consistent with experimental measurements, the STIs computed from our non-polarizable MD simulations are all positive and decrease in the order NaCl > NaBr > NaI. Given the much greater ion adsorption predicted by the polarizable MD simulations, it is not surprising that the STIs do not agree with experimental data (Table 3.5).The negative values of the STIs are a clear indication that the ion adsorption predicted by the polarizable force field is too strong, presumably due to over-polarization.[128]

Salt	Bulk Concentration	MD	Experiment
NaCl	1.26	-0.90	2.62^b
NaBr	1.19	-4.36	2.18^c
NaI	0.94	-6.71	1.16^d

Table 3.5: Comparison of surface tension increments ($\Delta\gamma$) from polarizable MD simulations with experimental measurements.[a] using $d(\Delta\gamma)/dc = 2.08$ mN/m or NaCl from Weissenborn and Pugh.[129] [b] using $d(\Delta\gamma)/dc = 1.83$ mN/m or NaBr from Weissenborn and Pugh.[129] [c] using $d(\Delta\gamma)/dc = 1.23$ mN/m or NaI from Weissenborn and Pugh.[129]
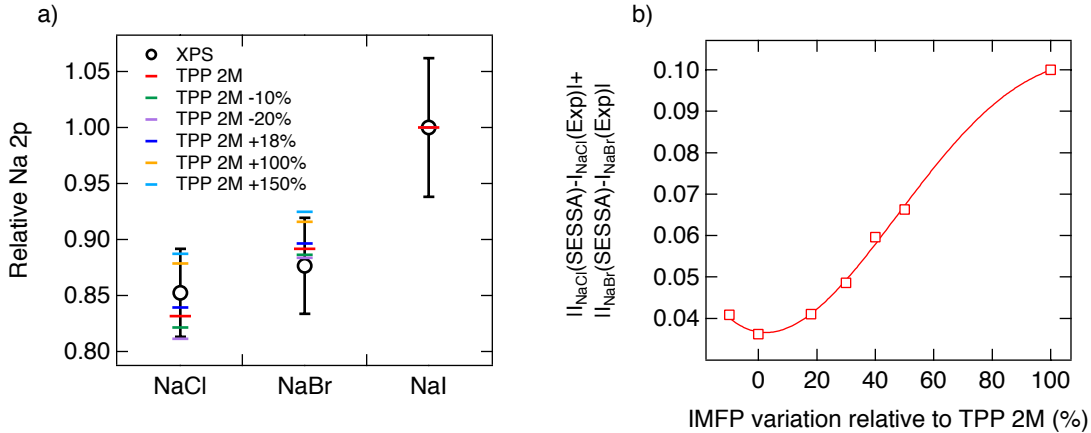
Figure 3.4: a.) Relative Na 2p intensity (integrated peak area) as predicted by SESSA simulations as the IMFP is systematically varied from that of the semi-empirical TPP 2M formula. The atom density profiles generated from the MD simulations of Figure 3.1 are used as input in SESSA. b) Sum of the differences between the calculated and measured Na 2p intensities for NaCl and NaBr as a function of the percentage variation of the IMFP relative to that implemented in SESSA and calculated using the TPP-2M formula. The continuous line serves as a guide for the eyes. This result suggests that the TPP-2M derived IMFP is the best fit to the experimental results.

3.3.5   Inelastic mean free path (IMFP) in aqueous solution.

The SESSA simulated Na 2p PE intensities shown in Figure 3.2a depend on the inelastic mean free path (IMFP) of the photoelectron, which, in turn, depends on KE and the properties of the system (material density, atomic or molecular mass, number of valence electrons per atom or molecule and the systems band gap). In SESSA, IMFPs are calculated using the semi-empirical TPP-2M formula of Tanuma et al.,[80] and its performance for predicting IMFPs of aqueous solutions (the TPP-2M formula was originally developed to calculate

IMFPs for solid materials) is assessed by systematically varying the IMFP from its nominal value while evaluating the predictions against experiment. At 82.5 eV and in bulk solution the IMFPs of the three ($\sim$0.7 M) electrolyte solutions are 0.80 nm, 0.78 nm and 0.77 nm for NaCl, NaBr and NaI, respectively (in pure water the IMFP is 0.81 nm). The effect of varying this IMFP by -20%, -10%, +18%, +100% and +150%, in otherwise equivalent SESSA simulation conditions, are shown in Figure 3.4. Shortening the IMFP by 20% (this has the effect of decreasing the ID) shifts the predicted Na 2p intensity from the NaCl aqueous solution outside the error bars of the experiment. Increasing the IMFP by 18% yields a result that remains in agreement with experiment, whereas an increase by 150% shifts the predicted Na 2p PE intensity of the NaBr aqueous solution outside the error bar of the experiment. These results are consistent with recent IMFP calculations for liquid water based on the full Penn algorithm (fPa), which is believed to be more accurate than the semi-empirical TPP-2M formula for KEs below $\sim$300 eV and predicts an IMFP that is 18% longer at 80 eV KE (0.96 nm) versus the TPP-2M value (0.81 nm) for pure liquid water.[130]The results of Figure 3.4 restrict the range of IMFPs for dilute aqueous electrolyte solutions that are consistent with the experimental results. We find acceptable IMFPs at ca. 80 eV KE to be in the range between 0.72-1.60 nm for NaCl, 0.71-1.57 nm for NaBr and 0.7-1.55 nm for NaI. This range of IMFPs can be compared with Suzuki and coworkers recent estimate of the effective attenuation length (EAL) of 1.89 nm at 79 eV for an aqueous solution of 0.14 M NaCl.[49] Since EAL is an upper bound of the IMFP (in the limit of no elastic scattering) and the best fit to our experimental results comes from the TPP-2M IMFPs, which are on the lower side of the ranges provided (Figure 3.9), our results suggest that their estimate was likely too high. Finally, since we do not anticipate significant change to the IMFP between dilute electrolyte solutions ($<$ 1 M) and pure water, our results reveal that the estimates of Bradforth and Winter, that pre-date those of Suzuki and coworkers, are also likely too high.[77]

3.3.6 Molecular-level origin of anion specific dependence of Na$^+$ concentration at the AWI.

The agreement of the STIs and the Na$^+$ enhancement at the AWI from the non-polarizable MD simulations with experimental data prompted us to use those simulations to seek additional insights into the origins of the anion-specific effects on the Na$^+$ distributions at the AWI. Given that the anion adsorption decreases in the order I$^-$ > Br$^-$ > Cl$^-$, the Na$^+$ adsorption must decrease in the order Na$^+$ in NaI > Na$^+$ in NaBr > Na$^+$ in NaCl due to the requirement that the interfacial region be electroneutral. As expected, this trend in Na$^+$ adsorption is observed in both our experimental and simulation results. In the remainder of this section we provide additional insights into the origins of the differences between the Na$^+$ distributions in the interfacial region.

The driving forces for ion adsorption include cavity formation, which promotes ion adsorption, and the loss of dispersion and hydration shell electrostatic interactions, which opposes ion adsorption.[131] When point charge models such as those employed in the present study are used, there is an electrochemical surface potential contribution, arising from electrostatic interactions, that opposes the adsorption of cations and favors the adsorption of anions.[131, 132] In addition, if ion-ion interactions are different at the AWI compared with in the bulk, they could contribute to the driving force for ion adsorption.

We limit our discussion to the energetic contributions that differ between the bulk solution and the position of the maximum in the Na$^+$ density profile, which is at a depth of ∼-0.6 nm into the solutions (Figure 3.1). Since we are seeking to rationalize the adsorption propensity of a particular ion, Na$^+$, the cavity contribution is irrelevant. Moreover, dispersion interactions are also not relevant since ion-pairing is negligible (¡ 5%) and constant from the bulk up to the topmost layer of each solution. In addition, the number of water molecules in the Na$^+$ solvation shell (∼5.8) is constant over the region of interest in all three solutions.

Next we turn to electrostatic interactions, starting with the total electrostatic potential energy (V_{elec}) of Na^+ ions. Contributions to for Na^+ arise from three different interactions, namely Na^+Na^+, Na^+X^-, and Na^+H_2O, where X^- are the different halide ions. Figure 3.5 shows the sum of these interactions for the three different 0.7 M aqueous solutions referenced to the bulk of each solution . All three solutions show a minimum in near the AWI that coincides with the maximum in Na^+ density predicted by the non-polarizable MD simulations shown in Figure 3.1 (marked by a dashed line in Figure 3.5). The magnitude of the minimum in reveals an anion-specific dependence, $V_{elec}(NaCl) < V_{elec}(NaBr) < V_{elec}(NaI)$.

To gain additional insights into the origin of the anion specificity of the Na^+ adsorption propensity, we decomposed V_{elec} into contributions from Na^+-Na^+, Na^+-X, and Na^+- H_2O interactions in Figure 3.6. The positive (unfavorable) Na^+- Na^+ interactions (Figure 3.6a) almost completely cancel the Na^+-X (favorable) interactions (Figure 3.6b) near the AWI, in and throughout all three solutions (Figure 3.10). Consequently, the Na^+-H_2O electrostatic potential energy profiles (Figure 3.6c) look very similar to the total profiles (Figure 3.5) and, hence, the specific anion effect on Na^+ adsorption propensities is an indirect effect wherein the identity of the anion affects the strength of the attractive Na^+-H_2O electrostatic interactions.
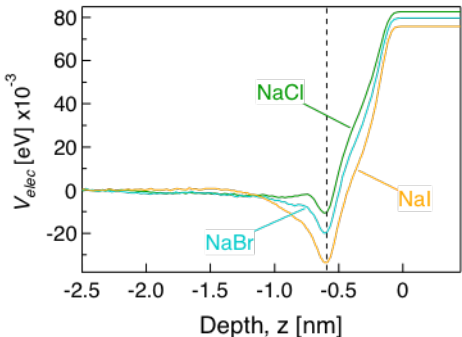
Figure 3.5: Total Na^+ electrostatic potential energy in 0.7 M aqueous solutions of NaCl, NaBr, and NaI using the non-polarizable force field. The instantaneous interface is at $z=0$ and negative depth is into the solution.
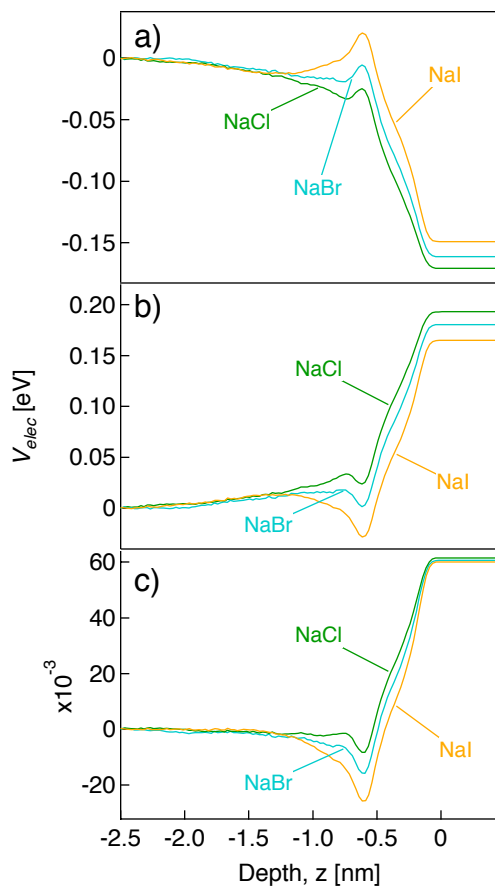
Figure 3.6: Decomposition of the total electrostatic potential energy of Na^+ into a) Na^+-Na^+, b) Na^+-X^-, and c) Na^+-water contributions, referenced to bulk values.

3.4   Conclusions

In the previous work[1] the SESSA protocol was demonstrated to be a straightforward methodology for directly calculating PE spectra from MD simulation. The present study validates the SESSA protocol as an accurate predictor of photoelectron spectra of the aqueous solution-air interface of sodium halide solutions. Additionally, the trend in relative surface enhancement of Na^+, namely, $NaI > NaBr \approx NaCl$, observed in experimental PE measurements, can be quantitatively reproduced using the SESSA protocol in conjunction with atom density profiles derived from MD simulations based on the non- polarizable force field of Horinek et al.[60] The comparison of the variability in the non- polarizable and polarizable MD/SESSA

results, and the failure of the polarizable MD simulation results to capture the same trend as the experiments highlight the importance of using physically realistic density profiles as input to the SESSA protocol. Moreover, given vastly different input density profiles from the non-polarizable and polarizable MD simulations, the possibility that SESSA could replicate the experimental result coincidently can be safely ruled out. This conclusion is supported by calculated surface tension increments, which agree semi-quantitatively with experimental data for the non-polarizable MD simulations, but have the wrong sign for the polarizable MD simulations. Thus, the work presented here validates a straightforward protocol for directly comparing MD simulation data to experimental PE data.

By varying the IMFPs used in the SESSA simulations we established a range of IMFPs consistent with the PE spectroscopy results. Our findings suggest earlier estimates are likely too long, which suggests the probe depth at low KE (here $\sim$85 eV) is significantly shorter than currently thought. Perhaps surprisingly we find the TPP-2M derived IMFPs yield better agreement with the experiments than those that approximate the fPa model.

Analysis of the MD simulations revealed a correlation between the Na^+ enhancement and Na^+H2O electrostatic interaction energies near the AWI.

3.5   Supplementary Information.

3.5.1   Information Depth (ID).

The IDs of Figure S1 are calculated for 0.7 M NaCl, NaBr and NaI solutions using SESSA. For this purpose the MD profiles have been sliced into layers and the photoelectron intensity of the O 2s has been simulated for each layer separately for a photoelectron kinetic energy of 87 eV. By doing this operation the total photoelectron signal is obtained as a function of depth and it is then easy to convert it into an ID as a function of the signal percentage. The number of slices needed to calculate the ID is larger than those used for a normal simulation of a peak intensity because in addition to the slices needed to accurately reproduce the interfacial region also part of the bulk has to be sampled in order to have enough points where the total signal percentage approaches 95%. Due to this procedure and due to the limitations of the number of slices that can be simulated in SESSA, the IDs for the three solutions are calculated at slightly different signal percentage. In particular we have ID=1.575 nm at a signal percentage of 95.3% for NaCl; ID=1.475 nm at a signal percentage of 95.1% for NaBr; ID=1.55 nm at a signal percentage of 95.3% for NaI.
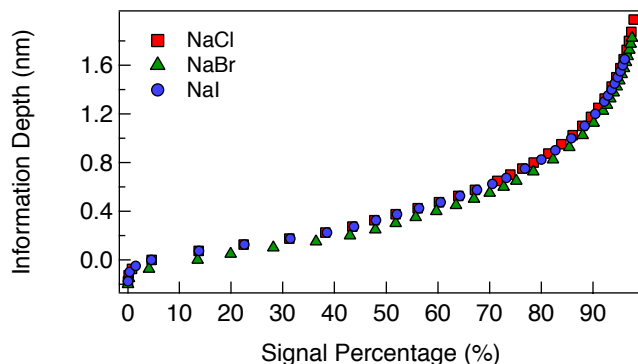
Figure 3.7: Information depth at 87 eV kinetic energy as a function of the percentage of the detected signal for a solution of 0.7 M (nominal concentration) of NaCl (red squares), NaBr (green triangles) and NaI (blue circles).
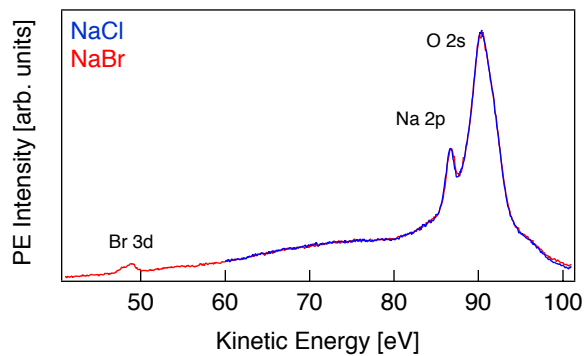
Figure 3.8: Photoelectron spectra of 0.75 M NaCl (blue) and 0.75 M NaBr (red).
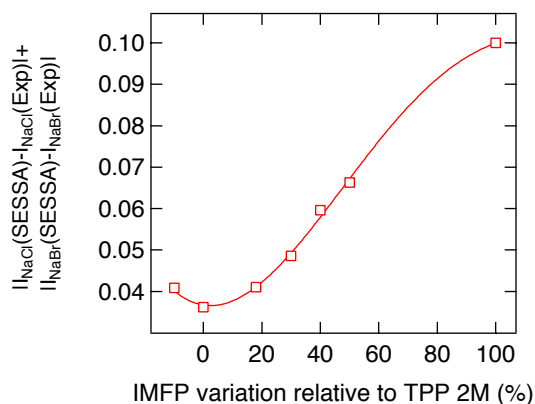
Figure 3.9: Sum of the differences between the calculated and measured Na 2p intensities for NaCl and NaBr as a function of the percentage variation of the IMFP relative to that implemented in SESSA and calculated using the TPP-2M formula. The continuous line serves as a guide for the eyes. This result suggests that the TPP-2M derived IMFP is the best fit to the experimental results.
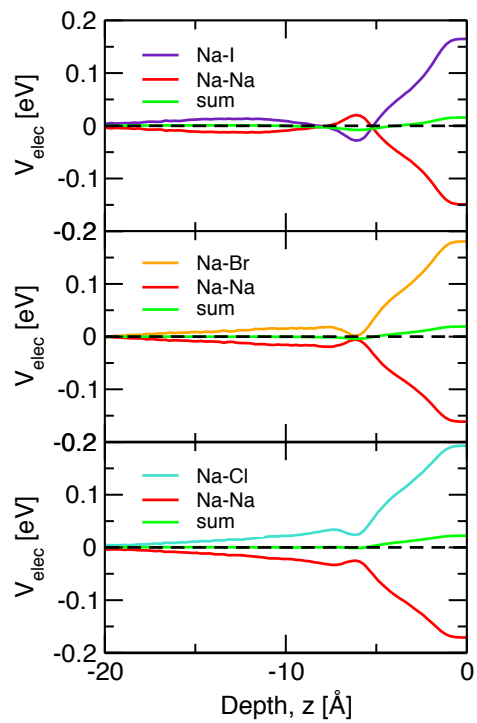
Figure 3.10: Na$^+$-Na$^+$ and Na$^+$-X$^-$ electrostatic interaction energies and their sum from non-polarizable MD simulations of 0.7 M (nominal concentration) NaI (top), NaBr (middle), and NaCl (bottom) solutions.

Chapter 4

Specific Cation Effects at the Aqueous Solution-Air Interface: Surfactant-Like Behavior of Li$^+$ Revealed by Experiments and Simulations

4.1 Introduction

Myriad chemical and biochemical processes that occur in aqueous salt solutions exhibit trends that depend systematically on the identities of the salt ions. These trends, which are commonly referred to as specific ion effects, generally follow the Hofmeister series, a ranking of the ability of salt ions to precipitate proteins that was developed by Franz Hofmeister and co-workers in the late 1800s.[5] The Hofmeister series applies to a wide range of seemingly unrelated phenomena, such as colloidal stability, critical micelle concentrations, chromatographic selectivity, protein denaturation temperatures, and the interfacial properties of aqueous salt solutions.[133, 134] Early attempts to explain the Hofmeister series relied on the notion that salt ions have a long-range effect on the structure of water, with ions on one side of the series acting as structure makers and ions on the other side as structure breakers.[133, 135] However, more recently, several experimental and computational studies have questioned the role of long-range ordering/disordering effects,[135, 136, 137, 33, 138, 139] and have provided compelling evidence that ion-specific behavior at aqueous interfaces must be taken into consideration when attempting to explain Hofmeister effects.[33, 140, 141, 142, 31]

Specific anion effects on the interfacial properties of aqueous salt solutions, such as surface tensions and surface potentials, closely follow the Hofmeister series for anions.[23] For example, surface tension increments (differences between the surface tension of a salt solution and that of neat water) of sodium salts at the same concentration decrease in the order: $SO_4^{2-} > Cl^- > Br- > NO_3^- > I^-$.[143, 144] Molecular dynamics (MD) simulations have predicted that the propensity of anions to adsorb to the solution-air interface follows the Hofmeister series in reverse,[33, 23, 145] and this prediction has largely been confirmed experimentally.[23, 27, 24, 146, 147, 148] Moreover, MD simulations have shown that, with few exceptions, anions adsorb more strongly to the solution-air interface than their counter-cations and, consequently, electrical double layers are formed near the interface, with the anions residing in

or near the topmost layer of the solution, and the cations below the anions.[23,149,59] Surface potentials,[150] phase-sensitive vibrational sum frequency generation (PS-VSFG) spectra (22, 26, 27), and x-ray photoelectron spectroscopic (XPS) data[24,151,152,127,87] are consistent with the double layer picture.

Compared to anion-specific effects, cation-specific effects at the solution-air interface are generally observed to be relatively weak. For example, the concentration dependence of the surface tension increments of LiCl, NaCl, and KCl are very similar.[106] In one of the few studies that directly determined cation-specific effects on ion distributions in the interfacial region, XPS spectra and MD simulations revealed that Na^+ approaches the solution-air interface more closely than Rb^+, and that the interfacial population of Cl^- is greater in NaCl vs. RbCl solutions.[127] PS-VSFG measurements, which provide indirect information on interfacial ion distributions via surface electric fields inferred from the imaginary part of the nonlinear susceptibility, have provided evidence of cation-specific effects on the strength of the electric double layer at the solution-air interfaces of nitrate, sulfate, and halide salt solutions.[148,153,154]

In almost all aqueous solutions of inorganic salts, cations are excluded from the topmost layer of the solution.[23] It has been suggested, based on MD simulations,[129,60,155] that Li^+ may be an exception. Presently, Li^+ is the only metal cation that has been observed in MD simulations to exhibit the surfactant-like behavior displayed by certain anions. However, this theoretical prediction has not been confirmed experimentally. Here we report liquid-jet XPS (LJ-XPS) measurements of the interfacial ion distributions in potassium and lithium halide solutions that provide direct experimental evidence that, indeed, Li^+ adsorbs to the solution-air interface, while K^+ does not. We also report MD simulations that qualitatively reproduce the LJ-XPS results and provide molecular-level insights into the origin of the differences in the behavior of Li^+ and K^+ at the solution-air interface.

4.2 Results and Discussion

4.2.1 Depth-dependent cation/water oxygen ratios from LJ-XPS spectra.

LJ-XPS signals originating from the I4d and K2p orbitals in 2 M KI and I4d and Li1s orbitals in 2 M LiI are shown in Fig.4.1 A-C for both low (probing the surface) and high (probing the bulk) photoelectron kinetic energies (KE). Comparison of the low and high KE spectra reveals that the I^- signal is greater at low KE than at high KE for both the KI (Fig. 4.1A) and LiI (Fig. 4.1C) solutions, consistent with the now well-established notion that the population of I^- ions is greater at the surface vs. the bulk in alkali iodide solutions.[23,24,59] The K^+ signal is lower at low KE than at high KE (Fig. 4.1B), indicating a depletion of K^+ ions at the surface relative to the bulk of the KI solution, which is also consonant with the prevailing picture of ion distributions near the surfaces of aqueous alkali halide solutions.[23,59] In contrast, the Li^+ signal at low KE is significantly higher than that at high KE (Fig. 4.1C). Thus, the spectra in Fig. 4.1C provide the first direct experimental confirmation of the prediction, made on the basis of MD simulations,[129,60,155] that Li^+ ions adsorb to the aqueous solution-air interface.

The integrated area under each spectral curve in Figures 4.1A-C provides a measure of the concentration of each ion at a particular probe depth of the experiment. To this end, the peak areas are first normalized by their respective photoionization cross section, photon flux, detection angle, and the electron transmission of the analyzer, as described in detail in the Materials and Methods section.(28, 36, 37) To obtain ion concentrations, the normalized ion spectral peak areas are divided by the normalized water O1s peak area at the same photoelectron KE. Fig. 4.1D compares the ratio of normalized cation/O1s signals from 2 M KI and LiI solutions as a function of photoelectron KE (eV) or experimental probe depth.
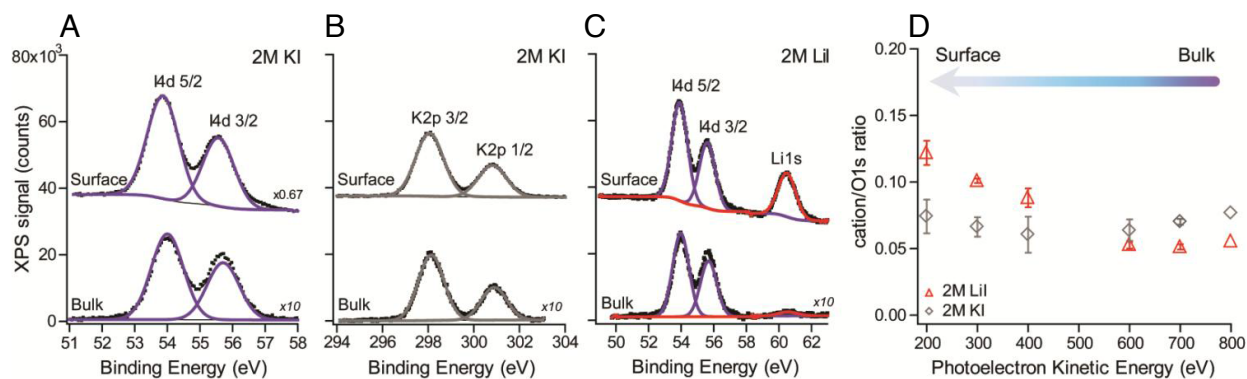
Figure 4.1: (A) Surface (200 eV KE) and bulk (600 eV KE) LJ-XPS spectra for (A,B) 2 M KI solutions and (C) LiI solutions. (D) Ratios of normalized cation/O1s signals plotted vs. photoelectron KE (probe depth).

The cation to oxygen ratios in the bulk (photoelectron KE $\geq$ 600 eV) of both the KI and LiI solutions exhibit the expected bulk stoichiometry within experimental statistics, thus validating our approach for obtaining depth profile information using LJ-XPS. While the K2p/O1s ratio remains essentially constant at all depths probed, the Li1s/O1s ratio exceeds the bulk stoichiometric ratio in the interfacial region (photoelectron KE $\leq$ 400 eV) and increases as the probing depth (photoelectron KE) decreases. Thus, the data in Fig. 4.1C clearly show that the concentration of Li$^+$ ions near the surface of a 2 M LiI solution is greater than in the bulk, i.e., that Li$^+$ is displaying surfactant-like behavior.

The cation to water oxygen ratios shown in Fig. 4.1C as a function of photoelectron KE for 2 M KI and LiI solutions are compared to the corresponding results for other 2 M K$^+$ and L$^+$ halide salt solutions (KCl, KBr, LiCl, and LiBr) in Fig. 4.7A-B. In all cases, the K2p/O1s ratios are essentially constant at all depths probed (200 eV to 800 eV) (Fig. 4.7A). As in the case of LiI (Fig. 4.1C), the Li1s/O1s ratios also increase with decreasing probe depth in LiCl and LiBr (Fig. 4.7B). At the lowest photoelectron KEs considered, the Li1s/O1s ratio increases in the order LiCl < LiBr < LiI. Thus, the extent of Li$^+$ adsorption tracks the reverse Hofmeister ordering of anion adsorption (Cl$^-$ < Br$^-$ < I$^-$) observed in previous XPS experiments[24] and MD simulations,[149] as well as the new anion/O1s ratios measured as a function of photoelectron KE reported in Fig. 4.7C-D.
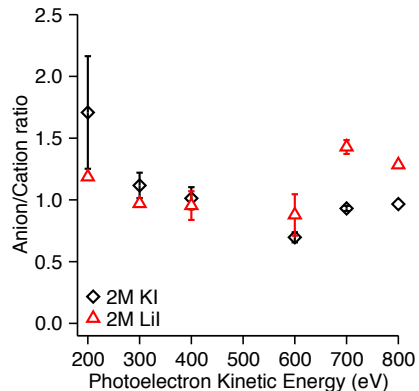
Figure 4.2: Ratios of normalized XPS signals (I4d/K2p for KI and I4d/Li1s for LiI) plotted vs. photoelectron KE (probe depth) for 2 M KI and 2 M LiI solutions.

4.2.2 Depth-dependent anion/cation ratios from LJ-XPS spectra.

Anion/cation ratios were determined from the XPS spectra by following the same procedure used to obtain the cation/O1s ratios. The I4d/K2p and I4d/Li1s ratios in the 2 M KI and 2 M LiI solutions, respectively, are plotted vs. photoelectron KE (probing depth) in Fig. 4.2. The I^-/K^+ ratio is greater than unity at the lowest photoelectron KE (200 eV) measured, indicating an excess of I^- anions over K^+ cations near the surface of the KI solution. This result is qualitatively consistent with previous XPS measurements,[24] but the surface I/K ratio in the present study is lower, presumably, in part, because the previous measurements were carried out on a deliquesced solid (saturated solution), whereas the measurements reported herein were carried out on a 2 M solution. The I^-/Li^+ ratio in 2 M LiI remains essentially constant near unity over the entire range of photoelectron KE (Fig. 4.2). This result is consistent with our observation that both the Li^+/water O (Fig. 4.1A) and I^-/water O (Fig. 4.7D) ratios are greater, to roughly the same extent, at the solution surface than in the bulk. Thus, the anion/cation ratios confirm that Li^+ exhibits surfactant-like behavior, similar to I^-, while K^+ does not.

The LJ-XPS data reported in Figs. 4.1 and 4.2 were measured at a 20° angle between the polarization vector and the detection axis. To confirm that our findings are not affected by

electron emission anisotropy, in a separate experiment we measured the depth profile of 2 M LiI in comparison to 2 M NaI solutions at the magic angle (54.7°), where electron emission anisotropy is eliminated. In this case, only the orbital photoionization cross sections are needed to obtain the ion concentration ratios.[154, 101] The data measured at the magic angle for 2 M NaI and LiI solutions (Fig. 4.6)(ref)) confirm that the ion concentration ratios are independent of the experimental geometry. Since the measured signals are higher at the 20° scattering angle, we will focus on those data in the remainder of this paper.

Anion/cation ratios for 2 M KCl, KBr, and KI solutions are compared in Fig. 4.5A and those for 2 M LiCl, LiBr, and LiI solutions are compared in Fig. 4.5B. The anion/K^+ ratio at the lowest photoelectron KE measured decreases in the order KI > KBr $\sim$ KCl (Fig 4.5A). The anion/Li^+ ratios at the lowest photoelectron KE are slightly less than one for the LiCl and LiBr solutions (Fig. 4.5B), indicating that Li^+ ions are present with the anions in the interfacial region of those solutions.

4.2.3 Density profiles from MD simulations.

Density profiles for ions and water oxygen atoms, computed from MD simulations of 2 M KI and 2 M LiI solutions and divided by the corresponding bulk densities (ρ_0), are plotted in Fig. 4.3 vs. the distance from the instantaneous solution-air interface (i.e., depth into the solution). Referring the density profiles to the instantaneous interface (see SI Appendix for definition and method of calculation) reveals structure in the interfacial region that is obscured when mean density profiles are computed on a static grid.[77, 1] The water density profiles in Fig. 4.3 each display two peaks, one at $\sim$2 Å and the other at $\sim$5 Å below the interface, and the iodide density profiles display sharp peaks on the inner side of the topmost water layer, followed by a depletion zone centered around 5 Å below the interface, in which the ion density is lower than in the bulk. To maintain the electroneutrality of
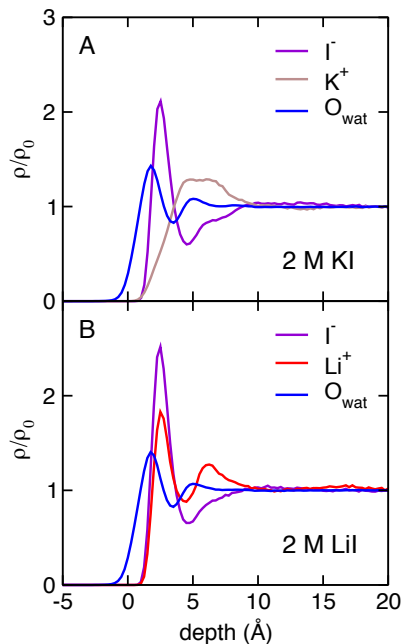
Figure 4.3: Density profiles of ions and water oxygen atoms from MD simulations of (A) 2 M KI and (B) 2 M LiI solutions. The density profile of each species has been calculated with respect to the instantaneous solution-air interface and divided by the corresponding bulk density, ρ_0. The interface is located at depth = 0.

the interfacial region, the density profiles of the cations also contain peaks corresponding to enhanced ion populations in the interfacial region vs. the bulk. Both the K^+ (in KI) and Li^+ (in LiI) density profiles indicate enhanced populations in the zone of I^- depletion below interfacial peak in the I^- density profiles. In addition, the Li^+ density profile displays a more prominent peak that is coincident with I^- interfacial peak. Thus, the MD simulation of 2 M LiI recapitulates the surfactant-like behavior of Li^+ inferred from the LJ-XPS data (Figs. 4.1 and 4.2).

The anion density profiles for K^+ and Li^+ solutions of all three halides considered show signal corresponding to surface-adsorbed anions that decreases in the order $I^- > Br^- > Cl^-$ (Figure S4). As for K^+ in the KI solution, the K^+ density profiles from the KBr and KCl solutions do not contain peaks corresponding to surface-adsorbed K^+ ions (Figure S4A-C). On the other hand, as in the case of Li^+ in LiI, the Li^+ density profiles from the LiBr and LiCl solutions display a peak (for LiBr) or shoulder (for LiCl) corresponding to surface-adsorbed anions

(Figure S4D-F). Thus, the surfactant-like behavior of Li^+ adsorption observed in the LiI solution is also seen in the LiBr and LiCl solutions, albeit to a lesser extent, and decreasing in the order LiI > LiBr > LiCl.

4.2.4 Origins of the different interfacial propensities of Li^+ and K^+ ions.

We can use our MD simulations to address the question of why Li^+ adsorbs to the topmost layer of water but K^+ does not. Although the relative importance of the various forces that drive ions toward or away from aqueous solution-air interfaces is a subject of on-going inquiry,[1,156,20,63,131,132] there is broad consensus that cavity formation promotes ion adsorption, and the loss of dispersion and local (hydration shell) electrostatic interactions accompanying ion desolvation opposes ion adsorption. In addition, when point-charge models are used for the ions and water molecules, as in the present study, there is an electrochemical surface potential, arising from broken symmetry in the water structure at ion-water and air-water interfaces, that favors the adsorption of anions and opposes the adsorption of cations.[156,20] In finite concentration solutions, such as those considered here, it is also possible that ion-ion interactions are different in bulk solution than in the interfacial region; in this case, there will be an additional electrostatic contribution to an ions adsorption propensity.

The cavity term clearly does not contribute to the greater adsorption propensity of Li^+ vs. K^+ because K^+ is larger than Li^+. As we shall see below, Li^+ retains its full solvation shell even when it is in the topmost water layer, while K^+ sheds part of its solvation shell as it approaches the surface of the solution. Due to the loss of water molecules in the K^+ solvation shell, the concomitant loss of dispersion interactions opposes K^+ adsorption. On the other hand, since Li^+ retains its full solvation shell at the interface, the difference in dispersion interactions between Li^+ at the interface and in the bulk should be negligible.

Thus, dispersion interactions are not expected to play an appreciable role in the adsorption of Li^+.

Next we examine the ion-ion and ion-water electrostatic interactions. The total electrostatic potential energy of K^+ ions in 2 M KI and Li^+ ions in 2 M LiI, as well as the contributions of cation-cation, cation-anion, and cation-water interactions, are plotted as functions of depth into the solutions in Fig. 4.4 A-B. Not surprisingly, the cation-cation electrostatic interaction energies are repulsive throughout each solution, and the shapes of the energy profiles resemble the shapes of the cation density profiles (Fig. 4.4C-D). The cation-anion electrostatic interaction energies are attractive throughout each solution, and the cation-anion interaction energy profiles are essentially mirror images of the cation-cation profiles. Thus, since these cation interactions balance throughout the solution the, cation-ion electrostatic interactions do not contribute considerably to the adsorption propensity of either K^+ in 2 M KI or Li^+ in 2 M LiI.

The cation-water electrostatic interactions are attractive throughout each solution, and relatively very weak compared to the cation-cation and cation-anion electrostatic interactions (Fig. 4.4A-B). For K^+ in the KI solution, there is a very shallow minimum in the cation-water electrostatic interaction energy profile (Fig. 4.4A), spanning roughly the same range of depth ($\sim$ 4-9 Å) as that of the enhanced K^+ density corresponding to the subsurface layer of K^+ ions (Fig. 4.4 C). Upon moving closer to the interface the K^+ water electrostatic energy rises to zero as the number of water molecules in the K^+ hydration shell drops from its bulk value of six (Fig. 4.4E). Thus, desolvation constitutes a small penalty to the adsorption of K^+ ions to the solution surface. Likewise, the Li^+ water electrostatic interaction energy profile displays minima (Fig. 4.4B) where the Li^+ density profile contains maxima (Fig. 4.4D), with the deepest minimum coinciding with the surface layer of Li^+ ions. The Li^+ ion is able to maintain attractive Li^+ water interactions all the way up to the solution surface because it retains its full hydration shell, consisting of four water molecules, throughout the
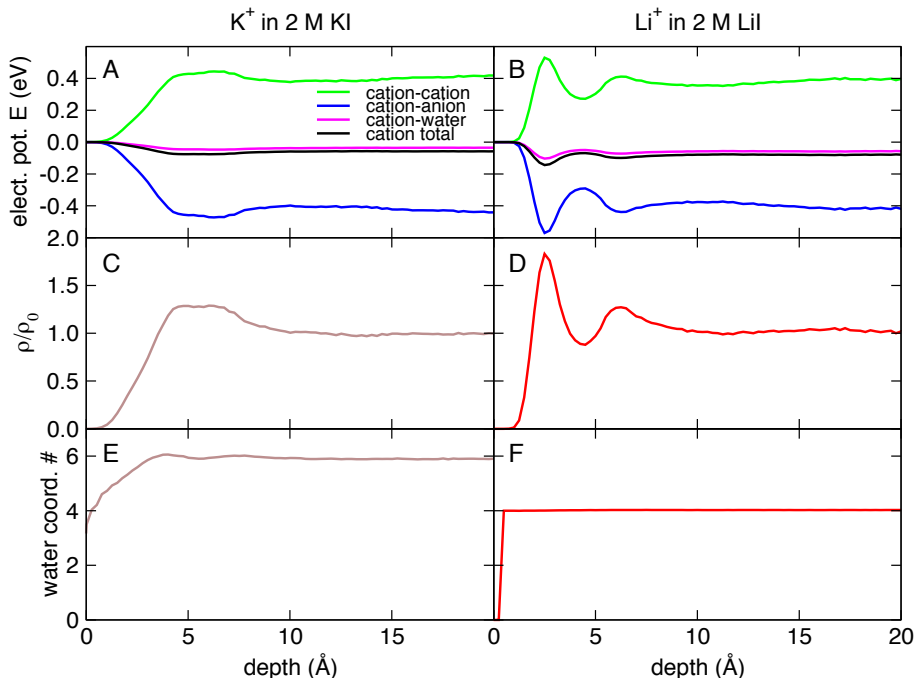
Figure 4.4: Depth-dependence of the electrostatic interaction energies of (A) K^+ ions in 2 M KI and (B) Li^+ ions in 2 M LiI. The green curves are contributions from cation-cation interactions, the blue curves from cation-anion interactions, and the magenta curves from cation-water interactions. The black curves are the total electrostatic interaction energies. (C) Density profile for K^+ ions in 2 M KI. (D) Density profile for Li^+ in 2 M LiI. (E) Number of water molecules in the first solvation shell of K^+ in 2 M KI. (F) Number of water molecules in the first solvation shell of Li^+ in 2 M LiI. All quantities in this figure were calculated with respect to the instantaneous solution-air interface. The interface is located at depth = 0.

solution (Fig. 4.4F; see also[129]). The same picture emerges from our MD simulations of potassium and lithium bromide (Fig. 4.9) and chloride (Fig. 4.10) solutions: in all cases attractive cation-anion electrostatic interactions are essentially canceled by repulsive cation-cation electrostatic interactions throughout each solution, K^+ loses favorable electrostatic interactions with water due to desolvation as it approaches the solution surface, and Li^+ retains its solvation shell and favorable electrostatic interactions with water molecules in the topmost layer of solution.

4.3 Conclusions

We employed a combination of LJ-XPS experiments and MD simulations to investigate specific cation effects at the aqueous solution-air interfaces of potassium and lithium halide solutions. The cation/oxygen and anion/cation ratios from the LJ-XPS experiments and the density profiles from the MD simulations show that Li^+ ions adsorb to the interface, but K^+ does not. Consistent with previous studies,[23,24,59] both the LJ-XPS experiments and MD simulations also show that the iodide anion exhibits surfactant-like behavior. Moreover, the simulations predict that the halide anion adsorption propensity decreases in the order $I^- >$ $Br^- > Cl^-$ in both K^+ and Li^+ solutions, and that the extent of anion adsorption does not depend significantly on the identity of the counter-cation in the solutions considered here. The simulations provide evidence that the primary reason Li^+ ions are able to approach the interface more closely than K^+ is that Li^+ ions retain their full hydration shell, and the associated favorable ion-water electrostatic interactions, even in the topmost layer of the solution. In contrast, while K^+ ions retain their complete hydration shell up to the subsurface layer beneath the surface anion layer, as they approach the surface more closely they shed part of their hydration shell and lose stabilizing electrostatic interactions with water molecules.

4.4 Materials and Methods

4.4.1 Liquid Jet X-ray Photoelectron Spectroscopy experiments.

Salt solutions were prepared by weighing out each salt and dissolving with highly demineralized water (conductivity $\sim$0.2 μS/cm, 18.2 MΩ, deionized water), up to 100 mL. Salts were purchased and included potassium iodide (puriss. p.a., 99.5%, Sigma Aldrich), lithium

iodide (99.9% trace metals basis, Sigma Aldrich) and sodium iodide (Sigma Aldrich). All solutions were sonicated for 5 minutes to finish dissolving the salt in the solution. The solutions were filtered, as necessary, to remove residual debris in the solutions, using sterile 0.45 μm polyethersulfone membrane (VWR International) filters and sterile syringes. Each filtered solution was then degassed in the sonicator for an additional 3 minutes.

LJ-XPS is a surface sensitive technique that can determine the relative ion distributions near the surface and in the bulk of aqueous solutions. Liquid jet experiments were performed at the Molecular Environmental Sciences beamline (11.0.2) at the Advanced Light Source (ALS) at Lawrence Berkeley National Laboratory.[157,158,22,159,160] A laminar flowing micro liquid jet (Microliquids Inc.) of 21μm diameter was pumped using a 0.5 mL/min flow rate using a pulse-dampened dual piston high pressure liquid pump to allow for continuous flow of solution. An external chiller was used to hold the liquid solution at a constant temperature of 6° C. An injection valve was used to inject 25 mL of each salt solution into the jet to keep the jet at continuous flow.

A four-stage differentially pumped lens and hemispherical analyzer system (Phoibios 150, Specs) was used for X-ray photoelectron analysis of the liquid microjet. The liquid jet was oriented normal to the axis of the near ambient pressure analyzer. The liquid jet position was placed within 0.5 mm of the analyzer aperture. The X-ray beam was oriented 70 degrees with respect to the analyzer, resulting in a 20° angle between the polarization of the horizontally polarized photon beam and the electron detection axis. The differential pumping and focusing of the lenses were used to allow photoelectrons to be detected by the hemispherical analyzer, kept at a base pressure of 3×10^{-9} torr with the jet in probe position with liquid water. A temperature-controlled catch basin was mounted below the liquid jet to catch the solutions. This basin was initially filled with 500 mL of a 40 wt % NaCl solution that was kept at a temperature of approximately -10°C, controlled by an external ethanol chiller. The temperature controlled catch basin filled the liquid-jet chamber with 1 torr of

water vapor.

Tunable linearly polarized X-ray radiation from the light source was used to probe the interface layers and the near surface region of the liquid microjet. The energy resolution of the ALS beamline varied between 150 and 853 meV for the range of photon energies used (203 to 1335 eV) for a 60 μm x 50 μm spot size. The analyzer was set to a pass energy of 20 eV with a 0.05 eV/step and a 0.1 ms dwell time. At low photoelectron kinetic energies (~200 eV), photoelectrons can escape from the interface of the flowing liquid microjet with an inelastic mean free path of approximately 10 Å.[161]

A photoelectron kinetic energy of 200 eV, used to probe the interface layers, resulted in the following photon energies for each region: 253 eV for the I4d and Li1s regions, 495 eV for the K2p region, and 735 eV for the O1s region. At high photoelectron kinetic energies (~800 eV), photoelectrons with inelastic mean free paths of up to ~30 can escape from deeper in the solution, characteristic of the bulk.[161] A depth profile was determined by using increasing photoelectron kinetic energies including 200 eV, 300 eV, 400 eV, 600 eV, 700 eV and 800 eV. A 600 eV photoelectron KE for the bulk measurements corresponded to the following photon energies for each region: 653 eV for the I4d and Li1s regions, 895 eV for the K2p region and 1135 eV for the O1s region.

The normalization factor, as described by Yeh and Landau[162] and Ottosson et al.,[151] was computed to normalize recorded XPS signals to the photon flux, transmission of the X-ray beam through 1 torr of water vapor, the atomic photoionization cross section of each respective element, and the β factor, an asymmetry factor for the electron detection that depends on orbital geometry. Although the data was not collected at the magic angle, for the photoelectron kinetic energies greater than 100 eV used in these experiments, the photoelectron anisotropy is expected to be minor.[101] The normalized peak areas are shown to provide an accurate measure of relative concentrations for bulk measurements, and may also be applied to the surface data. The photon flux was recorded for each beam time using a

photodiode. The X-ray transmission through water vapor was computed using the resources from the Center for X-ray optics on-line program provided by the Center for X-ray Optics at LBNL.[163]

4.4.2   Molecular Dynamics Simulations.

MD simulations of $\sim$ 2 M aqueous LiCl, LiBr, LiI, KCl, KBr, and KI solutions consisted of 1728 water molecules and 68 ion pairs. The dimensions of the simulation cell were 30 Å $\times$ 30 Å $\times$ 140 Å for each system. Periodic boundary conditions were applied in all three dimensions, resulting in solution slabs $\sim$70 Å thick with two solution-vacuum interfaces at z $\sim \pm35$ Å. The SPC/E model was used for water,[164] and the ion force field parameters were taken from Horinek et al.[129] (see Table 4.1 for a full listing of the force field parameters employed in this study). The MD trajectories were generated using the Gromacs simulation suite[165] for 80 ns each with a timestep of 1 fs; the last 70 ns of each trajectory was used for analysis. The temperature was held constant at 300 K using a Berendsen thermostat[166] with velocity rescaling to ensure the correct kinetic energy distribution.[90] Water molecules were held rigid using the SETTLE algorithm.[121] The electrostatic energies and forces were calculated using the particle-mesh Ewald method,[94] and a cutoff of 9 Å was used to truncate the Lennard-Jones interactions and the real-space part of the Ewald sum.

4.5 Supplementary Information

4.5.1 Materials and Methods

Definition and calculation of the instantaneous interface

All of the results from the molecular dynamics (MD) simulations are plotted vs. depth in solution. The solution surface is located using the instantaneous interface construction devised by Willard and Chandler,[20] which involves convoluting the instantaneous density field of the water oxygen atoms and ions with Gaussian distributions:

$$\phi(r; \eta, \xi) = \eta(2\pi\xi)^{-3/2} exp(-r^2/2\xi^2) \tag{4.1}$$

to obtain a coarse-grained density field. The location of the interface in each configuration is then taken to be the isodensity surface defined by the locus of points at which the coarse-grained density field is equal to half the bulk density of the solution. The width (ξ) and scaling (η) parameters of the Gaussians are listed in Table 4.1. The width parameter for the water O atoms was taken from Willard and Chandler.[20] The parameters for the anions were chosen such that the local density field in a simulation of a single bulk solvated ion was homogeneous.[63] The cations were not included in the convolutions because, due to their relatively small size, their contribution to the overall solution density is negligible.

Water survival function and residence time in the cation solvation shells

The survival function, $n(t)$, for water molecules in the solvation shell of a specific ion is a time correlation function proportional to the probability that a given water molecule, chosen by chance, is present in the coordination shell of the ion at time given that it was present at time t = 0:[167]

$$n(t) = \frac{1}{N} \sum_{n=0}^{N-n} \sum_{j} P_j(t_n, t) \tag{4.2}$$

where $P_j(t_n,t) = 1$ if the jth water molecule is present in the solvation shell of the ion at times t_n and $t_n + t$, $P_j(t_n,t) = 0$ otherwise, and N is the total number of configurations. Two survival functions were computed for water molecules in the solvation shell of each cation in the 2 M KI and LiI simulation systems by partitioning the MD simulation configurations in two groups according to the ion location in either bulk solution or the surface region, as indicated by the ion depth with respect to the instantaneous air-solutions interface. Water residence times, τ, were computed, using a normalized form of the corresponding survival function, as $n(t=\tau) = e^{-1}$.

Liquid Jet X-ray Photoelectron Spectroscopy experiments.

Photoelectron spectra measured at the magic angle.

It is possible that the geometrical anisotropy of the photoelectron emission process[152,77] in the XPS experiments could lead to results that suggest an enhancement of the Li^+ ion concentration (relative to the I^- anion) near the surfaces of lithium halide solutions when in fact such an enhancement does not exist. To rule out this possibility, we carried out
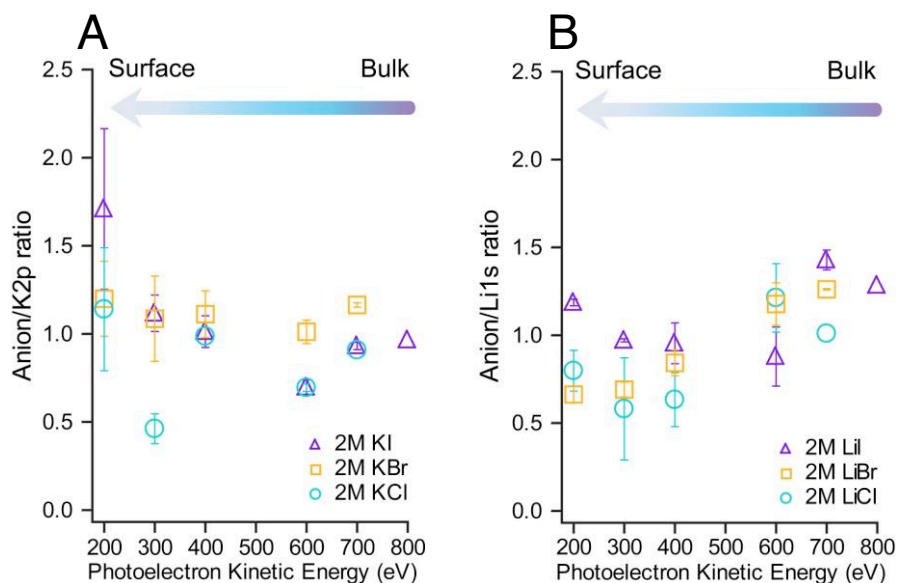
Figure 4.5: Ratios of normalized anion and cation XPS signals plotted vs. photoelectron KE (probe depth) for (A) 2 M potassium halide and (B) 2 M lithium halide solutions.

experiments in which the instrumental geometry was modified so that the polarization of the X-ray beam was at an angle of 54.7° with respect to the electron detection axis, i.e., at the so-called magic angle, where the angular anisotropy vanishes.[152,77] To determine depth profiles of the anion/cation ratios for 2 M NaI and 2 M LiI solutions, XPS spectra were measured at the magic angle for photoelectron kinetic energies ranging from 150 eV to 700 eV. At the magic angle, only the photoionization cross sections are required to obtain the anion/cation ratios. As can be seen in Fig. 4.7, where we plot the anion/cation ratios vs. photoelectron KE obtained from XPS spectra measured at the magic angle, the observation that Li^+ ions are present near the solution surface, while Na^+ ions are depleted, persists in the absence of photoelectron emission anisotropy.

101
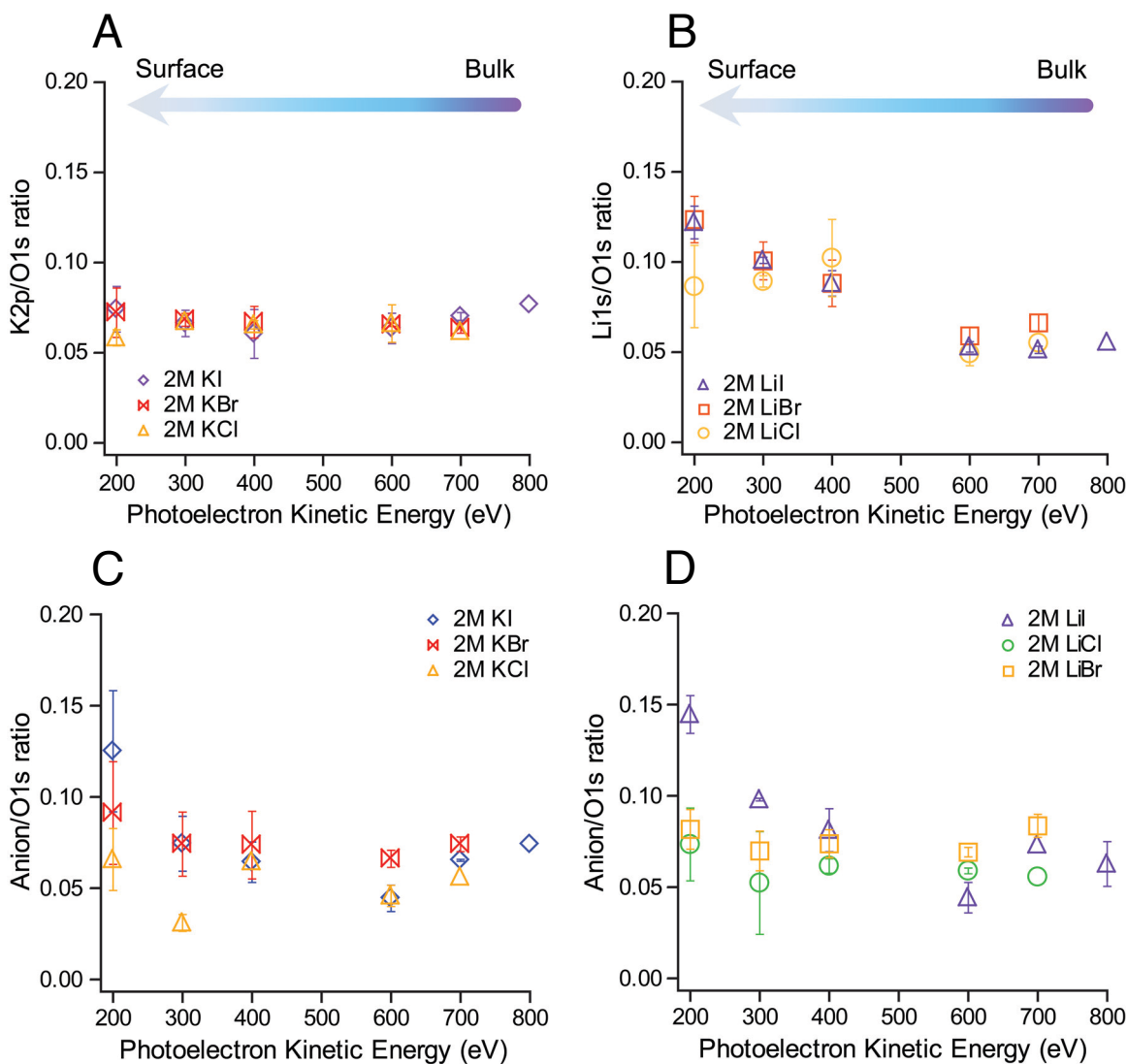
Figure 4.6: Ratios of normalized cation and water oxygen XPS signals plotted vs. photoelectron KE (probe depth) for (A) 2 M potassium halide and (B) 2 M lithium halide solutions. Ratios of normalized anion and water oxygen XPS signals plotted vs. photoelectron KE (probe depth) for (C) 2 M potassium halide and (D) 2 M lithium halide solutions.
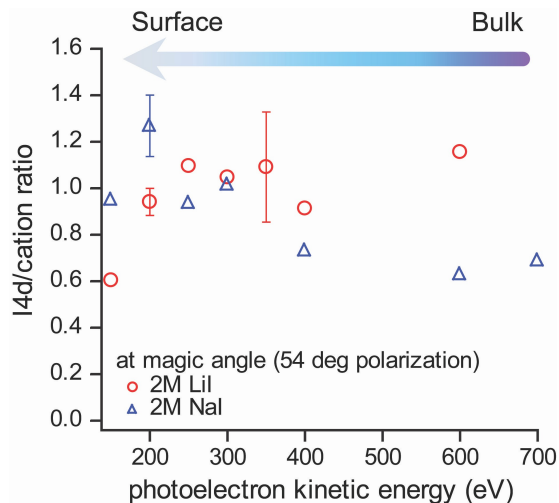
Figure 4.7: Ratios of normalized XPS signals (I4d/Na2s for NaI and I4d/Li1s for LiI) plotted vs. photoelectron KE (probe depth) for 2 M NaI and 2 M LiI, obtained from XPS spectra measured with a 54.7° angle between the polarization of the horizontally polarized photon beam and the electron detection axis. These data are similar to the results shown in Fig. 4.2 of the main manuscript, indicating that our experimental observation that Li^+ ions adsorb to the solution-air interface is not an artifact of electron emission anisotropy.

Atom	q (e)	σ (Å)	ϵ (kJ/mol)	ξ (Å)	η
O	-0.847	3.166	0.65	2.4	1.0
H	+0.4238	-	-	-	-
Li^+	+1.0	1.474	0.65	0.0	0.0
K^+	+1.0	2.945	0.65	0.0	0.0
Cl^-	-1.0	4.394	0.416	0.0	0.0
Br^-	-1.0	4.834	0.2106	2.55	0.477
I^-	-1.0	5.014	0.985	2.7	3.35

Table 4.1: Force field parameters and instantaneous interface convolution parameters. The force field parameters for water O and H atoms are from the SPC/E water model.[66] The ion force field parameters are from Horinek et al. (set 2 for Li^+, K^+, and I^-; set 1 for Cl^- and Br^-).[60]
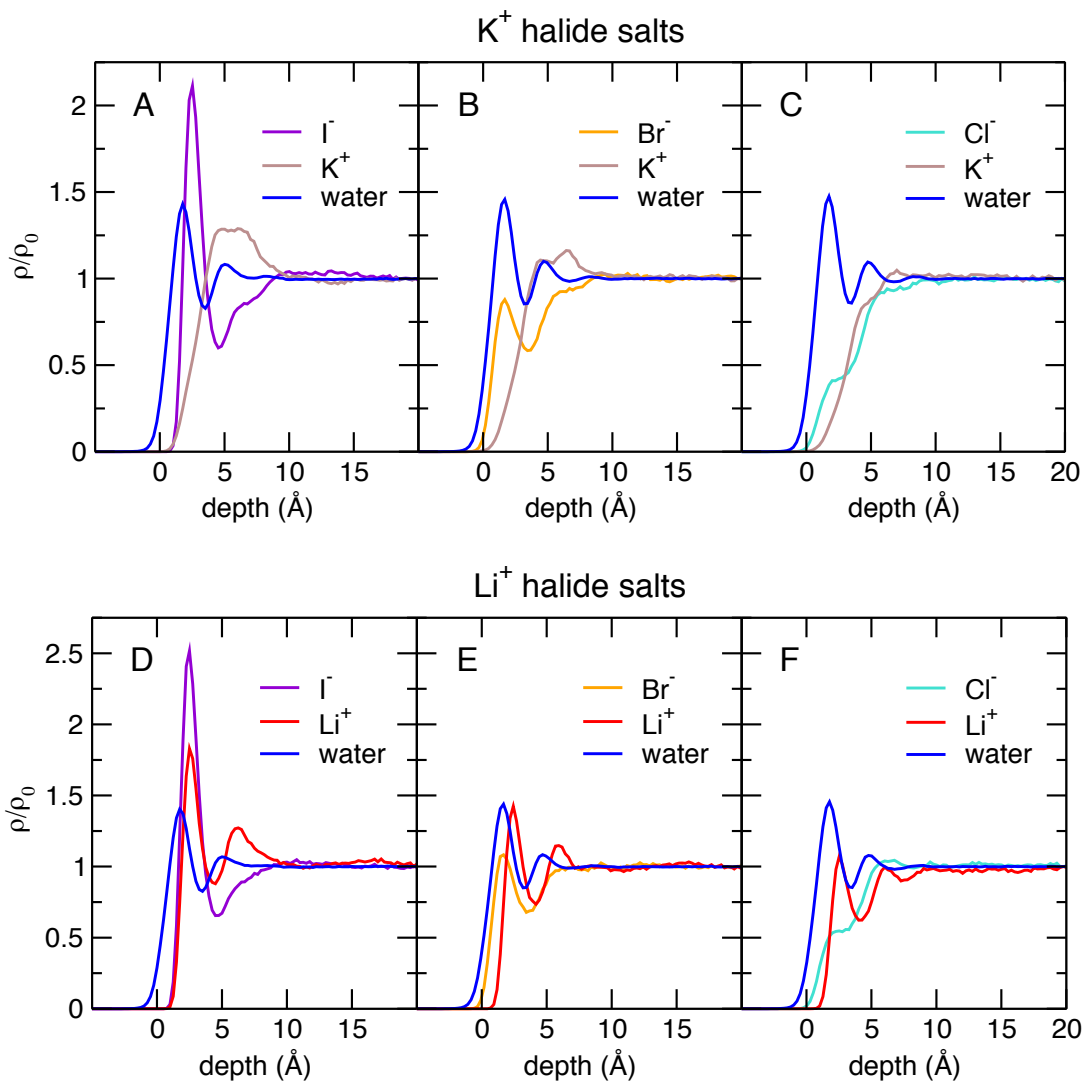
Figure 4.8: Density profiles of ions and water oxygen atoms from MD simulations of (A) 2 M, (B) 2 M KBr, (C) 2 M KCl, (D) 2 M LiI, (E) 2 M LiBr, and (F) 2 M LiCl solutions. The density profile of each species has been calculated with respect to the instantaneous solution-air interface and divided by the corresponding bulk density, ρ_0. The interface is located at depth = 0.
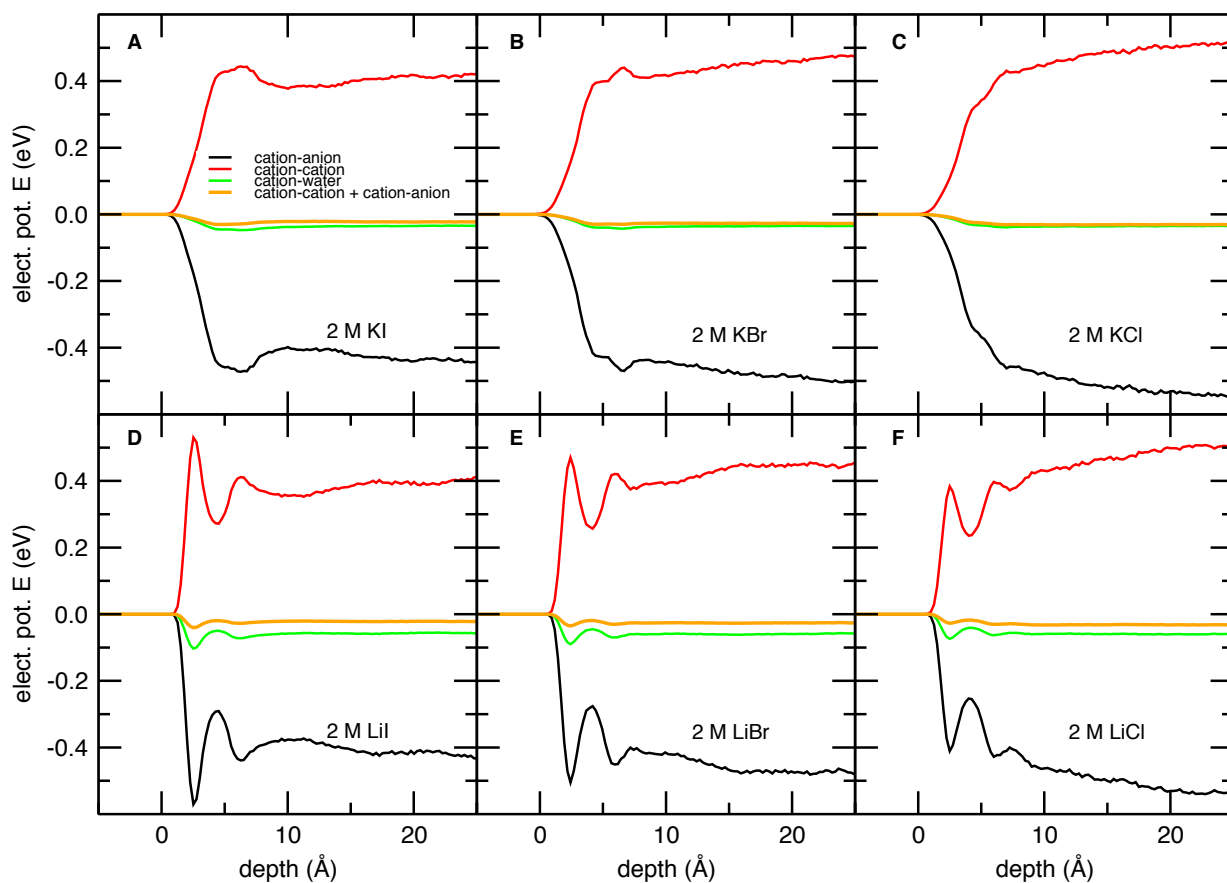
Figure 4.9: Depth-dependence of the electrostatic interaction energies of (A) K^+ ions in 2 M KI, (B) K^+ ions in 2 M KBr, (C) K^+ ions in 2 M KCl, (D), Li^+ ions in 2 M LiI, (E) Li^+ ions in 2 M LiBr, and (F) Li^+ ions in 2 M LiCl. The black curves are contributions from cation-anion interactions, the red curves from cation-cation interactions, and the green curves from cation-water interactions. The orange curves are the sum of the cation-anion and cation-cation electrostatic interaction energies.
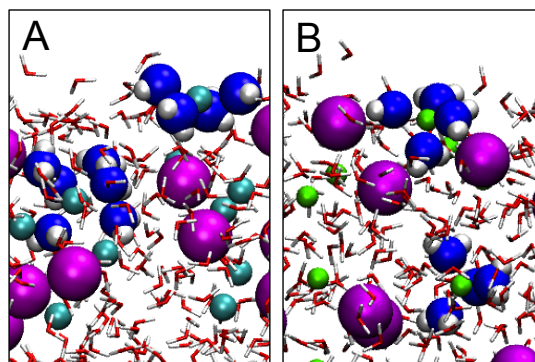
Figure 4.10: Snapshots of the interfacial region in simulations of (A) 2 M KI and (B) 2 M LiI. K$^+$ ions are colored cyan, Li$^+$ ions green, I$^-$ ions magenta. Water molecules in the first solvation shell of two cations in each system are drawn as spheres with oxygen atoms colored blue and hydrogen atoms white. The remaining water molecules are drawn in licorice representation with oxygen atoms colored red and hydrogen atoms white.

Solution	bulk concentration (M)^a	$\Delta\gamma$ (mN/m)^b MD	$\Delta\gamma$ (mN/m)^b experiment^c
KCl	2.23	3.47	3.66
KBr	2.10	2.06	2.94
KI	1.98	1.79	2.40
LiCl	2.19	3.52	3.68
LiBr	2.12	1.82	2.84
LiI	1.95	0.68	1.62

Table 4.2: Comparison of surface tension increments ($\Delta\gamma$) from MD simulations with experimental measurements.^{a}Obtained from the region of the simulated systems where all of the density profiles are flat. ^{b} $\Delta\gamma = \gamma$solution γwater. ^{c}Calculated using the bulk concentrations in the second column and the d($\Delta\gamma$/dc) values tabulated by Marcus,[168] which were converted from the d($\Delta\gamma$)/dm values tabulated by Pegram and Record,[144] where c is molar concentration and m is molality.
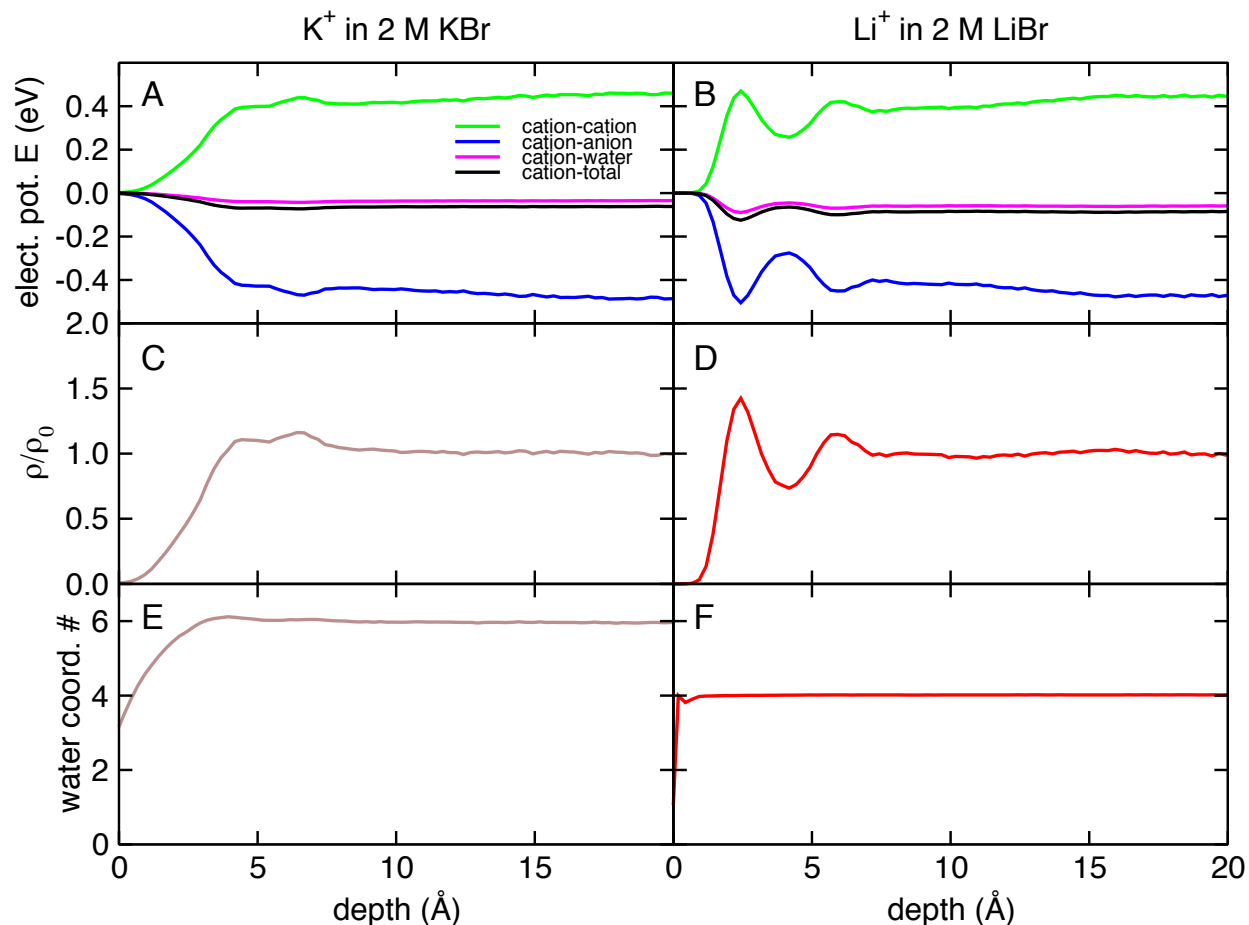
Figure 4.11: Depth-dependence of the electrostatic interaction energies of (A) K^+ ions in 2 M KBr and (B) Li^+ ions in 2 M LiBr. The green curves are contributions from cation-cation interactions, the blue curves from cation-anion interactions, and the magenta curves from cation-water interactions. The black curves are the total electrostatic interaction energies. (C) Density profile for K^+ ions in 2 M KBr. (D) Density profile for Li^+ in 2 M LiBr. (E) Number of water molecules in the first solvation shell of K^+ in 2 M KBr. (F) Number of water molecules in the first solvation shell of Li^+ in 2 M LiBr. All quantities in this figure were calculated with respect to the instantaneous solution-air interface. The interface is located at depth = 0.
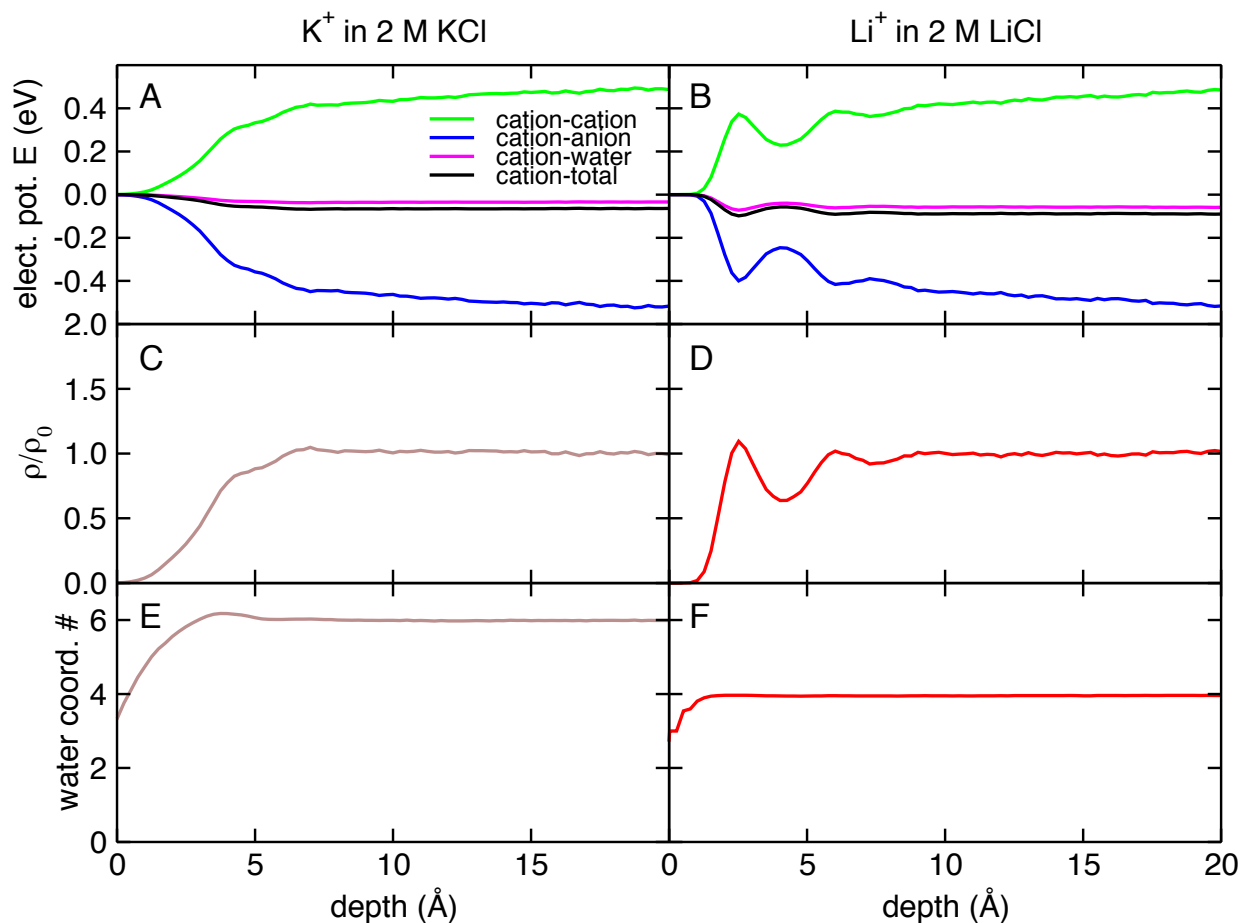
Figure 4.12: Depth-dependence of the electrostatic interaction energies of (A) K^+ ions in 2 M KCl and (B) Li^+ ions in 2 M LiCl. The green curves are contributions from cation-cation interactions, the blue curves from cation-anion interactions, and the magenta curves from cation-water interactions. The black curves are the total electrostatic interaction energies. (C) Density profile for K^+ ions in 2 M KCl. (D) Density profile for Li^+ in 2 M LiCl. (E) Number of water molecules in the first solvation shell of K^+ in 2 M KCl. (F) Number of water molecules in the first solvation shell of Li^+ in 2 M LiCl. All quantities in this figure were calculated with respect to the instantaneous solution-air interface. The interface is located at depth = 0.
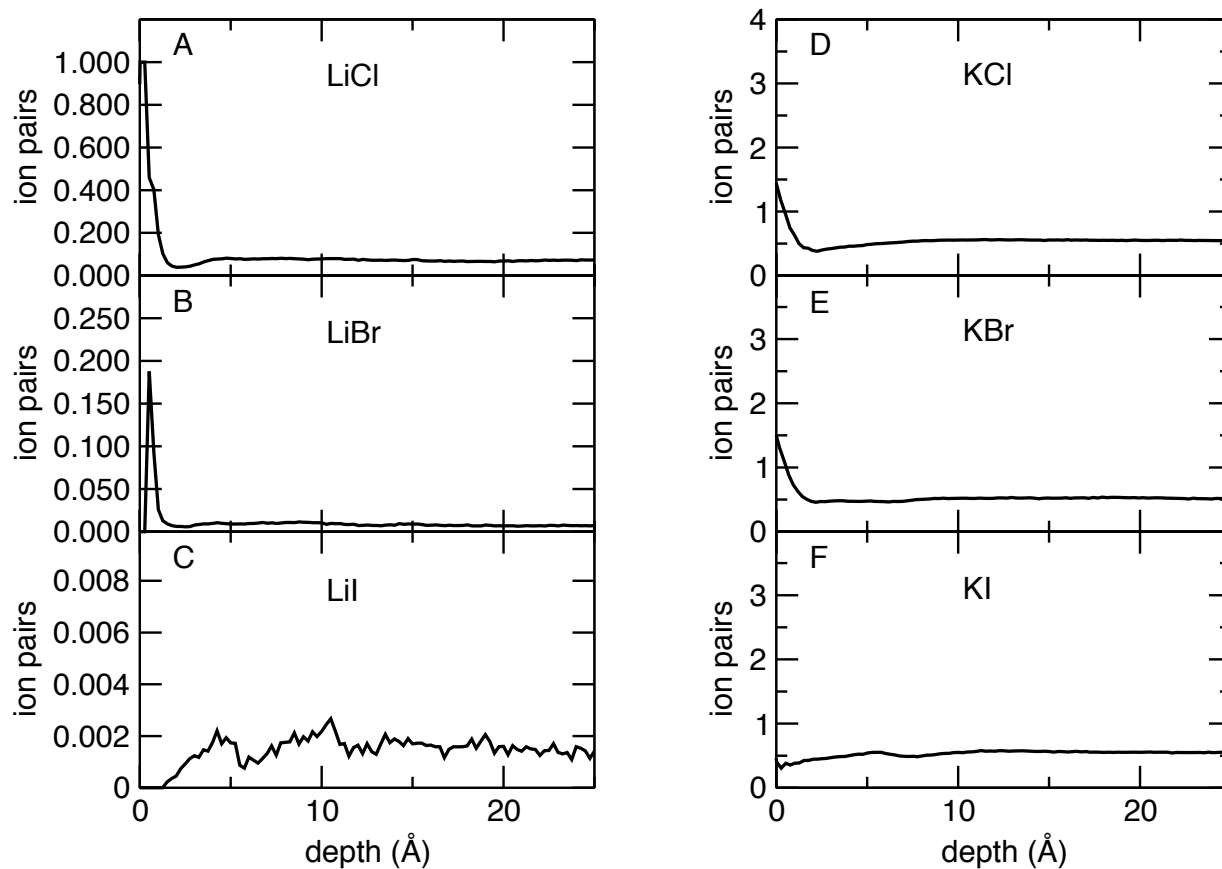
Figure 4.13: Depth dependence of the average number of cation-anion pairs in: (A) 2 M LiCl, (B) 2 M LiBr, (C) 2 M LiI, (D) 2 M KCl, (E) 2 M KBr, and (F) 2 M KI. Ion pairs were considered to be formed when the cation-anion distance was less than the position of the first minimum in the cation-anion radial distribution function. The specific distance cutoffs used were: Li^+-Cl^-, 2.90 Å; Li^+-Br^-, 2.95 Å; Li^+-I^-, 3.15 Å; K^+-Cl^-, 3.85 Å; K^+-Br^-, 4.06 Å; K^+-I^-, 4.36 Å.

Chapter 5

Solvent-Shared Ion Pairs at the Air-Solution Interface of Magnesium Chloride and Sulfate Solutions Revealed by Sum Frequency Spectroscopy and Molecular Dynamics Simulation

5.1 Introduction

Atmospheric aerosol composition and size are strongly correlated to thunderstorm activity, lightning production, and precipitation.[105,169] The ability for aerosol particles to take up atmospheric gas phase water determines whether they can act as cloud condensation nuclei (CCN), that is, whether they can initiate cloud droplet formation. Depending on their origins and atmospheric journey, aerosols are composed of various chemical species including, among others, inorganic and organic ions, acids, and surfactant-like compounds in varying concentrations. Although it is well accepted that surface-active long-chain fatty acids such as palmitic and oleic acid are the most atmospherically prevalent,[170] there has been increasing evidence over the last two decades showing that certain atmospherically relevant inorganic ions also exhibit definite surface activity.[23,22,171]

Large and polarizable anions have been mostly considered as being surface-active,[59,27,24,172] whereas cations are known, for the most part, to be repelled from a water surface.[23] In this new paradigm of research focused on ion surface activity, cations have been much less studied, although a few studies do exist.[173,87,154,151] The classical view considers that ions are repelled from the surface of water due to image charge effects.[113] Small, highly charged cations have strongly held hydration layers, making them much less apt to reside near or at the aqueous surface. There is evidence that doubly charged anions, such as SO_4^{2-}, are also repelled from the air-aqueous interface.[174,149,148]

The Mg^{2+} cation can certainly be categorized as a strongly hydrated cation. For instance, it was shown in prior work by Allen et al. and others that the bulk Raman spectra of magnesium salt solutions exhibit a Mg^{2+}-OH_2 vibrational resonance at ~ 360 cm^{-1}, demonstrating the strength of the first solvation shell water molecules.[175,176,177] There is also strong evidence that Mg^{2+} is indeed repelled from aqueous surfaces[151,177,178,179,180] In addition, magnesium has most recently gained attention due to its observed prevalence at the

surface of marine aerosols.[181] Magnesium ion is the central metal cation of chlorophyll, and is strongly correlated with biological productivity in marine regions.[182,183]

Sulfate (SO_4^{2-}), on the other hand, is a relatively large and polarizable anion, yet it has a highly symmetric water coordination as shown in many studies of gas-phase clusters[184,185,186] and aqueous solutions.[175,187,136,188] Cluster studies suggest a symmetric coordination of ~ 12 water molecules,[184,189] and condensed phase work has indicated sulfates unique solvent-separated ion pairing behavior.[175,190] With the prevalence of Mg^{2+} and SO_4^{2-} ions in naturally occurring systems,[191] an important question is: which of these species will have a higher surface propensity, or preference for the air-aqueous interface?

In the study reported herein we addressed this question using a combination of vibrational sum frequency generation (VSFG) spectroscopy, heterodyne-detected VSFG (HD- VSFG) spectroscopy, and molecular dynamics (MD) simulations. HD-VSFG is a phase- resolving spectroscopic technique that provides access to the imaginary part of the nonlinear susceptibility (Im $\chi^{(2)}$) of the interface.[192,193,194,195] The magnitude and direction of the effective surface electric field of aqueous electrolyte solutions is inferred from the sign and magnitude of the Im $\chi^{(2)}$ response.[148] The net direction of the OH transition dipole moment, either upward (toward the vapor phase) or downward (toward the aqueous phase), correlates with a larger number of anions (or cations) existing nearer to the surface relative to their counterions, thus inducing the water molecules to orient preferentially. In a simplistic view, one can imagine that a particular distribution of anions and cations, say, in an electrical double layer (EDL), forces a particular net orientation of interfacial water dipoles. It was suggested previously by using HD-VSFG spectroscopy that, for $Mg(NO_3)_2$ solutions, Mg^{2+} prefers bulk solvation, whereas NO_3^- is more surface-active.[151] The ion distribution of $MgCl_2$ has not yet been investigated using HD-VSFG, but prior MD simulations and VSFG studies point to a greater surface activity of Cl^- over Mg^{2+} which prefers bulk solvation.[180]

Here, we investigate the aqueous surfaces of magnesium salt solutions ($MgSO_4$ and $MgCl_2$)

using VSFG and HD-VSFG spectroscopy to provide an experimental view of the air- aqueous solution interface as a proxy for the surfaces of salt-containing atmospheric aerosol particles. We then use MD simulations to make a connection between the ion distributions in the interfacial region and the surface electric fields inferred from the HD-VSFG spectra. We find that in $MgCl_2$, Cl^- approaches the interface closely, while Mg^{2+} prefers to remain fully solvated in the bulk region. In contrast, in $MgSO_4$ solutions a change in the sign of Im $\chi^{(2)}$ is observed, suggesting a reversal in the surface preference for the Mg^{2+} ion. In the traditional interpretation of Im $\chi^{(2)}$ in terms of the direction of the surface electric field, this would indicate that the Mg^{2+} is the more surface-active species when paired with SO_4^{2-}. Our MD simulations predict that the distributions of Mg^{2+} and SO_4^{2-} are essentially the same, in apparent disagreement with the experimental Im $\chi^{(2)}$ from the $MgSO_4$ solution surface. However, the surface electric fields computed from MD trajectories are consistent with those inferred from the Im $\chi^{(2)}$ spectra for both the $MgCl_2$ and $MgSO_4$ solutions. Based on further analysis of the MD simulations, we propose that the main contribution to the effective surface electric field in both the $MgCl_2$ and $MgSO_4$ solutions comes from solvent-shared ion pairs (SIPs) near the interface.

5.2 Experimental Procedures

5.2.1 Chemicals

Magnesium sulfate anhydrous ($MgSO_4$) (certified, 99.9%) and magnesium chloride hexahydrate ($MgCl_2 \bullet 6\ H_2O$) (certified ACS, 99%) were purchased from Fisher Scientific (Waltham, MA). Ultrapure water with a resistivity of 18.2-18.3 MΩ cm and measured pH of 5.6 (the pH is slightly acidic due to the dissolution of gaseous CO_2) was obtained from a Barnstead Nanopure system (D4741, Thermolyne Corporation, Dubuque, IA) equipped with additional

organic removing cartridges (D5026 Type I ORGANICfree Cartridge Kit; Pretreat Feed). Stock salt solutions were prepared by dissolving salts in ultrapure water and pretreated according to procedures described previously to remove potential remaining organic contamination.[196] The concentration of the $MgCl_2$ solution was standardized by Mohr titration,[197] whereas the concentration of the $MgSO_4$ solution was determined using the $\nu_1(SO_4^{2-})$ Raman stretching mode at ~ 980 cm^{-1}.[198] The measured pH of the salt solutions was in the range 5-7. All salt solutions were shown to be free of organic impurities, as revealed by the lack of VSFG signal in the CH stretching region (28003000 cm^{-1}). All solutions were thermally equilibrated to room temperature (296 $\pm$ 1 K) over 24 h prior to measurement.

5.2.2   VSFG and HD-VSFG Spectroscopy

VSFG and HD-VSFG spectroscopic measurements were performed on a broad-bandwidth VSFG spectrometer setup that has been described elsewhere.[199] The two measuring modes mainly differ by the design in the optical configuration of the sample stage area and by the data processing procedure.[200, 201] Incident angles for the visible (0.8 μm) and infrared (2.6 - 3.3 μm in the water OH region) were 59/63 $\pm$ 1° and 50/60 $\pm$ 1° for the VSFG and HD-VSFG experiments, respectively. The ssp (s for sum-frequency, s for visible, and p for infrared) polarization combination was selected and the average energy of the visible and infrared beams incident on the aqueous surface was 300/10 and 260/8 μJ for VSFG and HD-VSFG measurements, respectively.

In a typical experiment, ultrapure water was poured ($\sim$30 mL) in acid-cleaned Petri dishes (5 cm diameter) and spectra of the neat air/water interface were used as a reference to assess reproducibility during the entire experimental period. The reproducibility for both VSFG$|\chi^{(2)}(\omega)|^{2}$ was (Im $\chi^{(2)}(\omega)$) replaced by an aqueous salt solution and spectra were recorded in the water OH region; each spectrum was integrated for a period of 5 min. All VSFG spectra

were background-subtracted and normalized against a non-resonant VSFG spectrum from a GaAs(110) crystal (Lambda Research Optics, Costa Mesa, CA) to eliminate the spectral distortion caused by the uneven infrared beam energy distribution at different frequencies in the spectral region of interest. In the case of the HD-VSFG spectra, the normalization was done against a reference z-cut quartz crystal (MTI Corporation, Richmond, CA) according to procedures described elsewhere. The zero point on the HD-VSFG spectra was tethered to zero around 3200 for the $MgSO_4$ data according to Ji et al.[202] and Nihonyanagi et al.[192] Yet we note that recent experiments have shown that this procedure generates a positive spectral feature in the low frequency region (3000-3200 cm^{-1}) that is an artifact likely due to contamination and/or water adsorbed on the quartz surface.[203] All measurements were repeated at least three times to ensure reproducibility and were recorded at room temperature (296 $\pm$ 1 K). Only every second and fourth data point are plotted in the VSFG and HD-VSFG spectra, respectively, to avoid spectral clutter.

5.3 Computational Methodology

5.3.1 Simulation protocols

Simulations of $MgCl_2$ and $MgSO_4$ solutions, as well as of neat water, were performed using the NAMD 2.9 simulation package.[204] The number of water molecules and ions present in each simulation, chosen in order to give a nominal salt concentrations of $\sim$ 1 M, are listed in Table 5.1. Interfaces were created by setting up the systems in a slab geometry in a 38 Å $\times$ 38 Å $\times$ 120 Å box, with periodic boundary conditions implemented in all three dimensions.

The ions and water molecules were described using a polarizable force field based on the classical Drude oscillator model.[205] The SWM4-NDP model of Lamoureux et al. was used for water.[206] The SO_4^{2-} parameters were taken from Verde and Lipowsky,[207,208] the Cl$^-$

System	MgCl$_2$(aq)	MgSO$_4$ (aq)	Neat Water
num. water molecules	2308	2236	2592
num. cations	40	40	0
num. anions	40	40	0

Table 5.1: Compositions of systems simulated.

parameters from Yu et al.,[209] and the Mg^{2+} parameters from Lemkul and MacKerell.[210] Simulation of approximately 60 ns duration were carried out for each system at constant volume and a constant temperature of 298 K. The last 35 ns of each simulation was used for analysis. The smooth particle mesh Ewald method[95] was used to calculate electrostatic interactions. Short- range, real-space interactions were cut off between 10.5 Å and 12 Å using a switching function. A reversible, multiple time-step algorithm[211] was employed to integrate the equations of motion with a time step of 1 fs for the non-bonded forces and 0.5 fs for bonded forces. The lengths of water OH bonds were held fixed using the SHAKE[122] and SETTLE[96] algorithms. A Langevin dynamics scheme was used for temperature control.

5.3.2   Force Field Validation

To provide some assessment of force field quality, the bulk densities and surface tension increments of the MgCl$_2$ and MgSO$_4$ solutions were also computed and compared with experimental data. The solution concentrations (c) and densities (d) were calculated from bulk regions of the simulation cells. The surface tension increment (STI) is $\Delta\gamma =\delta$solution δneat water , and the surface tension is computed using eq 5.1:

$$\gamma = \frac{L_z}{2}\langle P_{zz} - \frac{1}{2}(P_{xx} + P_{yy})\rangle \tag{5.1}$$

where P$_{ii}$ are the diagonal elements of the pressure tensor, L$_z$ is the box length in the

	MgCl$_2$(aq)		MgSO$_4$(aq)	
Quantity	MD	Expt.	MD	Expt.
c (M)	0.95 ± 0.01	0.95	1.42 ± 0.03	1.42
d (g/mL)	1.048 ± 0.001	1.068	1.142 ± 0.003	1.16
$\Delta\gamma$ (mN/m)	2.50 ± 0.37	$3.05, 3.48 \pm 0.1$	4.05 ± 0.42	$2.54, 3.65 \pm 0.1$

Table 5.2: Bulk solution densities and surface tension increments from MD simulations and experiments.

z-direction (normal to the interface), the angular brackets denote a time average, and the factor 12 in front of the brackets accounts for the number of interfaces in the slab. Statistical uncertainties are reported as standard deviations calculated by using the method of blocking transformations.[96]

The calculated bulk densities for the MgCl$_2$ and MgSO$_4$ solutions, 0.95 ± 0.01 M and 1.42 ± 0.03 M, respectively, are close to the 1 M concentrations used for the VSFG measurements. The bulk densities and STIs computed from the simulations are compared to the corresponding experimental values in Table 2. The computed densities for the MgCl$_2$ and MgSO$_4$ solutions are 1.9% and 1.6% higher, respectively, than the experimental values. Although there is considerable variability in the experimental STIs reported in Table 5.2, both sets of measurements give a slightly higher value for MgCl$_2$ vs. MgSO$_4$, while the current simulations predict that the STI for MgCl$_2$ is lower than that of MgSO$_4$. However, it is reassuring that, consistent with experimental data, the computed STIs are positive for both solutions.

5.3.3   Definition of the Instantaneous Interface

Below, several quantities are reported that depend on the distance from the solution surface, which is located according to the instantaneous interface definition introduced by Willard and Chandler.[20] The instantaneous interface is defined at every instant in time by a coarse-grained density field obtained by convoluting the positions of the water oxygens and the ions

Atom	α	ζ
Cl^-	1.61	2.53
SO_4^{2-}	1.50	2.29

Table 5.3: Instantaneous interface Gaussian convolution parameters for anions.

with normalized Gaussians given by eq 5.2:

$$\phi(r; \alpha, \zeta) = \frac{\alpha}{(2\pi\zeta^2)^{3/2}} exp\left(\frac{-r^2}{2\zeta^2}\right) \tag{5.2}$$

where r is the position of a water oxygen or ion, ζ is the width parameter, and α the scaling parameter. The surface grids were then determined by parsing the density field and finding the z-value at each x,y-grid point at which the density is equal to half that of bulk water (0.033 Å $^{-3}$).

Following Willard and Chandler,[20] a half-width of $\xi = 2.4$ Å and scaling parameter of $\alpha = 1.0$ were used for the convolution of the water oxygens. The convolution parameters for the ions were determined by fitting a normalized Gaussian to the depletion in the local density field obtained from a simulation of an isolated bulk solvated ion.[63] In the case of Cl^- and SO_4^{2-}, the local density fields showed noticeable reductions (compared to the surrounding water density), which were described well by Gaussian functions (eq 2) with the parameters listed in Table 5.3. In the case of the Mg^{2+} cation, no depletion in the local density field was observed in bulk solution and, hence, no convolution was performed.

5.4　Results and Discussion

5.4.1　Anions Induce Structural Changes in Interfacial Water

Figure 5.1 shows the VSFG spectra of the interfacial region of neat water and 1 M aqueous salt solutions of magnesium salts measured in the OH stretching region (3000- 3800 cm^{-1}). It is important to clarify that the interfacial region refers here to the region between the vapor and aqueous phases that lacks inversion symmetry (centrosymmetry), and hence, that is SFG-active. In the case of neat water, only the topmost layers (∼1-3) are considered to contribute to the SFG signal, while the deeper sublayers make minimal contributions.[202, 212, 213] Yet, the presence of ions within the air-aqueous interfacial region generates an electrostatic field that reorients water molecules and extends the region of non-centrosymmetry. This has the effect of changing the SFG-active volume (i.e., interfacial depth), thereby leading to additional field-induced bulk contributions to the SFG signal. Recent models of charged aqueous interfaces have further shown that the extent of these contributions varies with the ionic strength[214, 215] In particular, at low ionic strengths, interference effects by mathematical modeling were shown to strongly reduce the expected SFG intensity, despite the fact that the interfacial depth is increased.At higher ionic strengths (10^{-1} M), the SFG lineshapes continue to be impacted by the absorptive-dispersive (i.e., optical) interactions resulting from changes in the interfacial potential; however, they are minimal in this regime.

The neat water VSFG spectrum in Figure 5.1 reveals a broad region spanning from 3000 to 3600 cm^{-1} representing water molecules with a broad distribution of coordination and hydrogen bond strengths, and a narrow band at 3700 cm^{-1} assigned to the distinct dangling OH bond of water molecules located in the topmost layer. In the lower frequency part of the broad region, it is accepted that hydrogen bonds are relatively strong, and as one moves to higher frequency, the hydrogen bonding strength weakens significantly; the spectrum
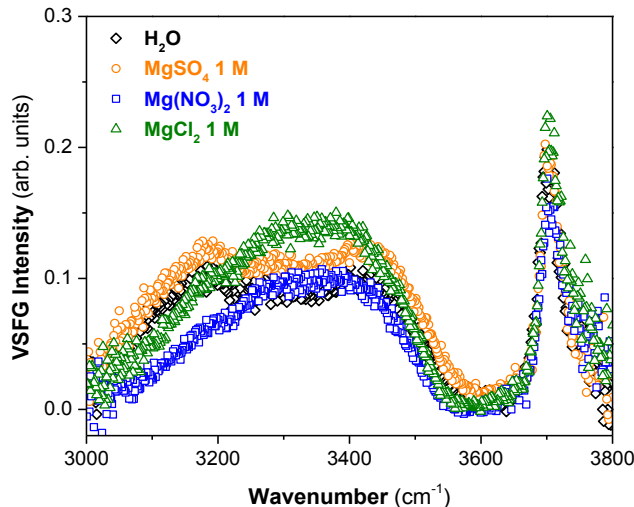
119

Figure 5.1: VSFG spectra of air-aqueous interfaces of 1 M $MgSO_4$, $Mg(NO_3)_2$, and $MgCl_2$ salt solutions over the entire OH stretching region (3000 - 3800 cm^{-1}). The $Mg(NO_3)^2$ data was previously reported by Hua et al.[151] The VSFG spectrum of the neat air-water interface is also shown as reference. The VSFG spectra contain the real (Re $\chi^{(2)}$) and imaginary (Im $\chi^{(2)}$) contributions.

represents collective motions of the water molecules that preclude one from making structural assignments to specific frequencies. However, additional assignments to this broad band have also been proposed.[44, 216, 217, 218, 219, 220]

The VSFG spectra of the 1 M magnesium salt solutions reveal variations primarily in the OH stretching region relative to neat water. Interestingly, the dangling OH band remains mostly unaffected for $MgCl_2$ and $MgSO_4$, yet not for $Mg(NO_3)_2$; albeit at higher magnesium chloride and nitrate concentrations, a decrease in the dangling OH oscillator strength was previously reported.[22, 24] The 1 M $MgSO_4$ spectrum follows closely the spectral profile of neat water, although with a slight increase in intensity. In contrast, the 1 M $Mg(NO_3)_2$ spectrum is less intense, and the 1 M $MgCl_2$ spectrum is narrowed and more intense relative to that of neat water. Overall, these spectra indicate a varying hydrogen bonding environment that depends on the identity of the anion. However, as was shown previously with $MgCl_2$ solutions,[24] some of these changes might be due to the convolution of the real and imaginary parts of $\chi^{(2)}$,[45, 77-79] such that it is difficult to know which frequency-dependent portion

of the spectrum relates directly to the OH transition dipole moment. This limitation is overcome by using HD-VSFG spectroscopy, which exclusively samples the Im $\chi^{(2)}$ response, thus enabling interrogation of the net orientation of the OH transition dipole moments and, in turn, to infer interfacial ion distributions.

5.4.2 Interfacial Water Orientation from HD-VSFG Spectra

The HD-VSFG Im $\chi^{(2)}$ spectra for neat water and the different magnesium salt solutions are shown in Figure 5.2a. Here the resultant sign and frequency-dependent intensity are related to the average orientation and the number density of OH oscillators. Figure 5.2b provides the difference between the Im $\chi^{(2)}$ salt spectra and that of neat water. Clearly, relative to neat water, the 1 M $MgSO_4$ spectrum has a completely negative Im $\chi^{(2)}$ response, while those of the 1 M $MgCl_2$ and $Mg(NO_3)_2$ spectra are both positive, albeit to a different extent. Interestingly, the $Mg(NO_3)_2$ Im $\chi^{(2)}$ spectrum is twice as intense as that of $MgCl_2$. Moreover, the magnitude of the $MgSO_4$ Im $\chi^{(2)}$ spectrum (Figures 5.2a,b) is largest when normalized to the total number of ions present, revealing that this salt combination has the strongest effect on the surface electric field.

The sign of the difference Im $\chi^{(2)}$ spectra has been used to infer the change in net orientation of water OH bonds in salt solutions relative to neat water, as well as the sign of the surface electric field produced by the ions that gives rise to the change of net orientation.[148] According to this line of reasoning, a positive difference Im $\chi^{(2)}$ spectrum, as seen here for the $MgCl_2$ and $Mg(NO_3)_2$ solutions, indicates that the OH bonds point their hydrogen atoms more toward the air compared to neat water, and implies that there is a negative surface field generated by an EDL formed near the interface, in which the anions are distributed closer to the interface than the cations. In contrast, from the difference Im $\chi^{(2)}$ spectra in Figure 5.2b, the sign of the effective surface electric field is positive in $MgSO_4$, i.e., reversed
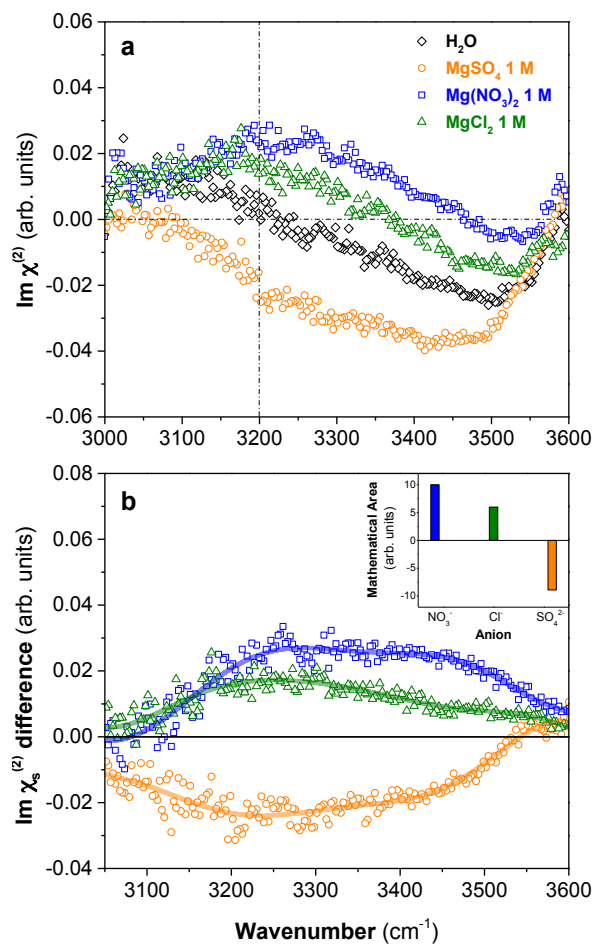
Figure 5.2: (a) Im$\chi^{(2)}$ spectra of air-aqueous interfaces of 1 M MgSO$_4$, Mg(NO$_3$)$_2$, and MgCl$_2$ salt solutions over the 3000 - 3600 cm^{-1} spectral region. Im $\chi^{(2)}$ spectrum of the neat air-water interface is also shown as reference. (b) Im $\chi^{(2)}$ difference spectra relative to neat water of the spectra in (a). The mathematical area under the Im $\chi^{(2)}$ difference curves is shown as an inset. The solid curves serve as eye guides to show the trend in the data.

compared to that of $MgCl_2$ and $Mg(NO_3)_2$. According to the above line of reasoning, this suggests a reversal in its surface preference of the Mg^{2+} ion, with Mg^{2+} approaching the interface more closely than SO_4^{2-} in $MgSO_4$. However, given the solvation shell stability and high surface charge density of the Mg^{2+} ion, is it reasonable to observe such a reversal in surface preference? If not, is it possible to observe a reversal of the surface electric field that is not a result of a reversal in the ion distribution? To answer these questions, MD simulations of $MgCl_2$ and $MgSO_4$ solutions were carried out.

5.4.3 Density Profiles from MD Simulations

In Figure 5.3 the normalized density profiles for the aqueous $MgCl_2$ and $MgSO_4$ solutions are shown alongside snapshots of the simulated solutions. The density profiles are plotted as a function of displacement z from the instantaneous interface at z = 0, and divided by the bulk density ρ_0 of each component. A pronounced electrical double layer is evident in the density profiles for the $MgCl_2$ solution: there is a sharp peak in the Cl^- distribution that overlaps with the topmost layer of water molecules,extending from z=3 Å to z=+2 Å , followed by a zone of depletion of Cl^- between z=3Å to z = 8 Å , in which Mg $^{2+}$ ions accumulate. In contrast, there is no pronounced layering of the ions in the $MgSO_4$ solution. Rather, the density profiles of both the Mg^{2+} and SO_4^2 ions are similar; the densities of both ions decay monotonically from their bulk values and vanish around z = 3 Å just below the topmost layer of water molecules. Upon close inspection, the Mg^{2+} density profile vanishes slightly closer to the interface than the SO_4^{2-} density profile, indicating that there is a weak but discernable charge separation near the surface of the $MgSO_4$ solution. A similar weak charge separation was observed in a MD simulation of a Na_2SO_4 solution that was validated by comparison of SFG spectra calculated from the MD trajectory to experimental data.[221]

The density profiles for the $MgCl_2$ and $MgSO_4$ solutions suggest a stark counterion depen-
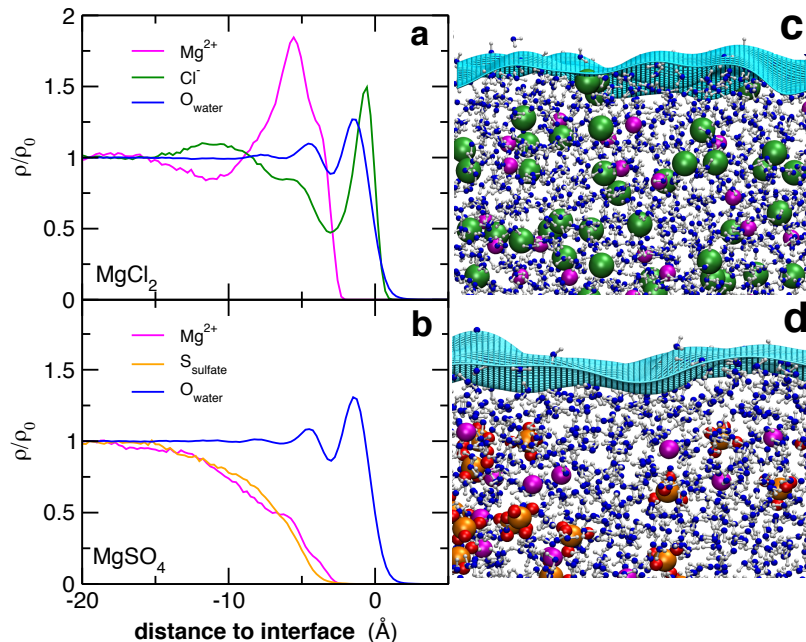
Figure 5.3: Normalized density profiles for the components of the (a) $MgCl_2$ and (b) $MgSO_4$ solutions. The instantaneous interface is located at $z = 0$ Å. Snapshots of the corresponding solutions are shown in panels c and d. The colors of the atoms displayed in the snapshot correspond to the legend shown in the density profiles. The instantaneous interface is depicted by a cyan mesh in each snapshot.

dence of the distribution of Mg^{2+} ions in the interfacial region. Although Mg^{2+} is repelled from the surface of both solutions, in the presence of the adsorbing Cl^- ion, Mg^{2+} participates in a pronounced double layer, whereas in the MgS_4 solution, Mg^{2+} is distributed roughly the same as the strongly surface averse SO_4^{2-} ion. The simulation results support the ion layering interpretation of the HD- VSFG spectra in the case of $MgCl_2$. In $MgSO_4$, the observation that neither of the ionic species shows any surface propensity indicates that the positive surface electric field inferred from the spectra does not originate from ion distribution in which Mg^{2+} is closest to the surface, followed by the SO_4^{2-} anion.
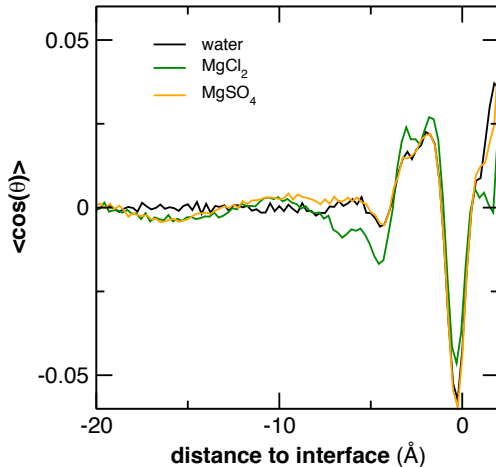
Figure 5.4: Water orientational order parameter profiles as a function of distance to the instantaneous interface for neat water, and $MgCl_2$ and $MgSO_4$ solutions.

5.4.4 Water Orientational Order Parameters

The VSFG signal in the OH stretching region originates from water OH oscillators in non-centrosymmetric regions. In order to quantify the interfacial depth probed by the VSFG experiments, an orientational order parameter, $\langle cos(\theta) \rangle$, was calculated where θ is the angle between a water molecules dipole moment and the z-axis terface ($\mathring{A}$) (directed along the normal to the air-water interface), and the angular brackets denote an average over time and water molecules. This quantity, which vanishes for a uniform orientational distribution, is plotted in Figure 5.4 as a function of displacement from the interface for the $MgCl_2$ and $MgSO_4$ solutions and a slab of neat water.

In all three systems, regions of net water orientation originating from the presence of the interface, and an inversion of the direction of the net orientation on going from the topmost to the second layer of water were observed. The order parameter profile for the $MgSO_4$ solution is almost identical to that of neat water, and in both cases the region of significant net water orientation extends roughly 5 $\mathring{A}$ into the solution, indicating that no EDL is formed in the $MgSO_4$ solution (Figure 5.3b). In contrast, the profile for the $MgCl_2$ solution displays some noteworthy differences from that of neat water, consistent with the presence of an EDL

125

near the surface of the MgCl$_2$ solution (Figure 5.3a). Near the location of the density peak of the chloride ions, from -3 Å to -1 Å , the values of $\langle cos(\theta) \rangle$ for the MgCl$_2$ solution are more positive compared to those for neat water, which means that the hydrogens of the water molecules of the MgCl$_2$ solution point more towards the surface than the hydrogens of pure water. In contrast, the values at the location of the density peak of the magnesium ions, from -8 Å to -2.5 Å , are more negative. These results show that the hydrogens of the water molecules in this region of the MgCl$_2$ solution point more away from the surface than the hydrogens of pure water.

5.4.5   Electric Fields

In the absence of ion layering and significant reorientation of water molecules in the interfacial region of the MgSO$_4$ solution, the origins of the positive surface electric field remain unclear. In order to gain insight into the origins of the surface electric fields inferred from the HD-VSFG spectra, an analysis of the electric fields acting on water OH bonds was performed. The electric field vector at the position of each water hydrogen was first calculated using eq 5.3:

$$E_H = \frac{1}{4\pi\epsilon_0} \sum_i \frac{q_i}{|r_H - r_i|^2} \hat{r}_{Hi} \tag{5.3}$$

where r$_H$ is the position vector of the hydrogen atom, q$_i$ is the charge and r$_i$ is the position vector of any other charge i in the system which is not located in the same water molecule, and $\hat{r}_{Hi}$ is the unit vector along the direction from the hydrogen atom to the charge i. Next, the resulting electric field vector was projected onto a unit vector along the corresponding OH bond. In 5.5, the projected electric field per bond is plotted as a function of the distance
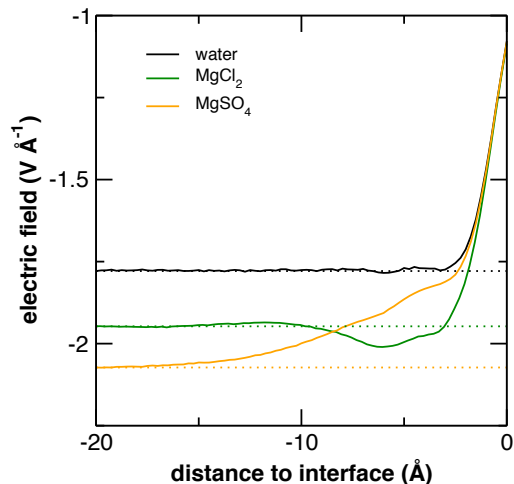
Figure 5.5: Total electric field projected onto water OH bonds, plotted as a function of the distance of the water oxygen to the instantaneous interface. The dotted lines serve as a guide to the eye for comparison of the interfacial electric field to the bulk value.

of the associated water oxygen to the instantaneous interface.

Upon moving from the bulk toward the surface of neat water, the electric field profile is flat until around 3 Å from the interface, where it rises steeply. A similar rise is seen at the same distance from the interface in the profiles for the $MgCl_2$ and $MgSO_4$ solutions. In addition, for the $MgCl_2$ solution there is a narrow region, from -7 Å to -3 Å, where the field is more negative than in the bulk, and for the $MgSO_4$ solution, there is a broad region, from -12 Å to the interface, where the field is more positive than in the bulk. In these regions, the magnitude of the deviation of the field from the bulk value is significantly greater for the $MgSO_4$ solution than the $MgCl_2$ solution.

The electric field profiles shown in Figure 5.5, for the $MgCl_2$ and $MgSO_4$ solutions agree qualitatively with the surface fields inferred from the corresponding difference Im $\chi^{(2)}$ spectra shown in Figure 5.2b. In particular, the observation that the electric field projected on the OH bonds is more negative (positive) in the interfacial region vs. in the bulk for the $MgCl_2$ ($MgSO_4$) solution is consistent with the negative surface field inferred from the Im $\chi^{(2)}$ spectrum for the $MgCl_2$ solution. Conversely, the observation that the electric field

projected on the OH bonds is more positive in the interfacial region vs. in the bulk for the $MgSO_4$ solution is consistent with the positive surface field inferred from the Im $\chi^{(2)}$ spectrum for the $MgSO_4$ solution.

The next step was to identify which water molecules contribute to the deviations from bulk behavior of the electric field profiles in the interfacial region of the $MgCl_2$ and $MgSO_4$ solutions. While considering water molecules in ion hydration shells, it was found that water molecules participating in SIPs make the dominant contribution to the deviations. These SIPs were identified by inspecting the ion-ion and ion-water radial distribution functions (RDFs) shown in Figure 5.6. The radial cutoff of the ion solvation shell is defined by the first minimum in the ion-water RDFs. The Mg^{2+} ion has a tightly bound and clearly defined solvation shell with a radial cutoff of 3.00 Å. The Cl^- ion has a more loosely bound hydration shell with a radial cutoff of 3.86 Å, whereas SO_4^{2-} has a broader solvation shell that extends out to 4.64 Å. No evidence of contact ion pairs is observed in the ion-ion RDFs of either solution; the first peaks in the ion-ion RDFs correspond to SIPs. For subsequent analysis, SIPs were identified by finding pairs of ions that share at least one water in their respective solvation shells.

The contributions from water molecules engaged in SIPs to the projected electric field profiles are shown in Figure 5.7a,b. In Figure 5.7c,d, snapshots of the projected electric field are shown at the position of the water hydrogens, represented as spheres. Only a small region of each solution is shown for illustrative purposes. A change in sign of the electric field is indicated by a change in color between red white, and blue. In this representation, the color of the water hydrogen is not important; only a change in color between the waters in a distinct region compared to the surrounding waters is significant. In Figure 5.7c, the majority of the projected electric field is colored red. Solvent-shared ion pairing is seen between the Mg^{2+} and Cl^- ions, and in the vicinity of the SIPs, the electric field changes sign. Similarly, in Figure 5.7d, waters in the vicinity of the $Mg2^+$ - SO_4^{2-} SIP show a change
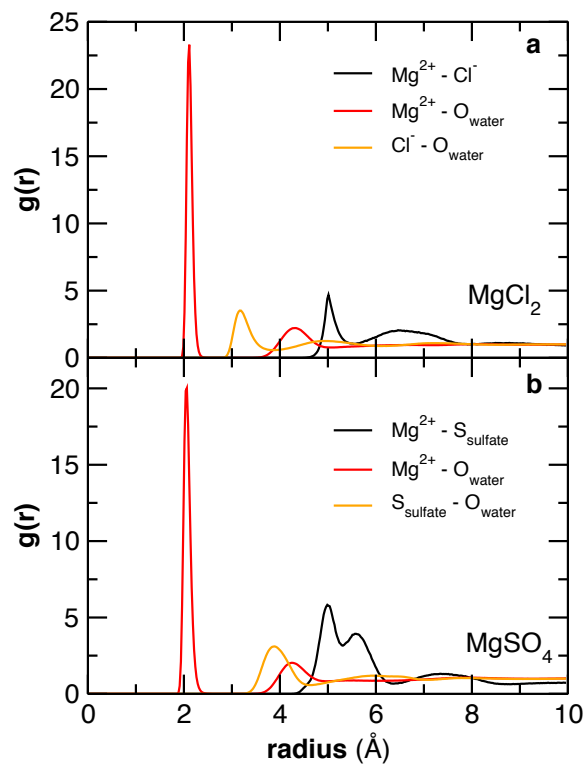
Figure 5.6: Radial distribution functions for the ion-water and ion-ion pairs for (a) $MgCl_2$ and (b) $MgSO_4$ solutions.
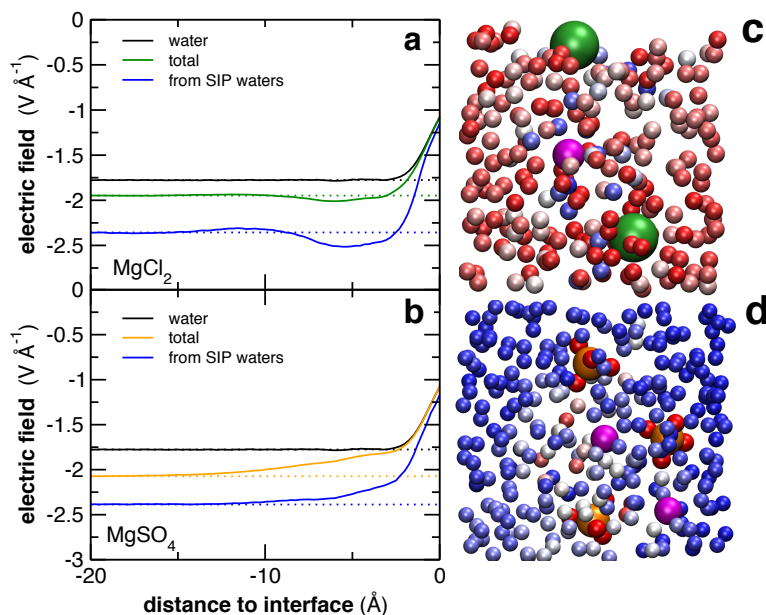
Figure 5.7: Projected electric field contributions for (a) MgCl$_2$ and (b) MgSO$_4$ solutions. The contributions from solvent shared ion pairs are plotted in blue. The total projected electric fields plotted in Figure 5.5 are reproduced here for comparison. Snapshots of the total projected electric field on water OH bonds are shown in panels c and d. The Mg^{2+} ions are colored magenta, the SO$_4^2$ sulfur and oxygen atoms in orange and red, respectively, and the Cl$^-$ ions in cyan.

in sign in the projected electric field (blue to red). This changes in sign of the electric field in the vicinity of the SIPs indicates that water molecules involved in these pairs have significant influence on the local electric field.

This effect was quantified in Figure 5.7a and b. In the MgCl$_2$ solution (Figure 5.7a), a significant negative region (with respect to bulk) is observed in the projected electric fields of water molecules in solvation shells of SIPs near the interface (between 2.5 Å to 9 Å). Comparing this to the total electric field profile of the MgCl$_2$ (plotted in green in panel a), it is clear that some of this negative electric field contribution is averaged out when considering all of the waters in the interfacial region. In the case of the MgSO$_4$ solution (Figure 5.7b), the opposite trend is observed, with a positive contribution (with respect to bulk) to the electric field coming from water molecules in the solvation shells of SIPs. This positive region spans from the interface to approximately 12 Å into the solution. As can be seen, this trend

130

is not significantly averaged out in the total electric field plot (plotted in orange). Close to the interface (3 Å to 0 Å), the contribution of the waters in solvation shells of SIPs to the total projected electric field is around 90%. Figure 5.7 indicates that the main contribution to the deviation of the effective surface electric field from its bulk value comes from waters in the solvation shells of SIPs. Figures 5.5 and 5.7 agree qualitatively with the difference HD-VSFG spectra shown in Figure 5.2b, in the sense that the surface electric field is negative in the $MgCl_2$ solution, and positive in the $MgSO_4$ solution.

That SIPs are the origin of the positive surface electric field in the $MgSO_4$ solution is an intriguing possibility that needs to be reconciled with the observation that the ion population in the $MgSO_4$ solution decays rapidly as the interface is approached from below (cf. the density profiles in Figure 5.3b). Based on additional analyses presented below, we propose that a particular orientation of the Mg^{2+} SO_4^{2-} SIP near the interface dominates the effective surface electric field, despite the infrequent occurrence of such a scenario. To verify this hypothesis, an orientational order parameter $\langle \cos(\phi) \rangle$ is defined, where ϕ is the angle between the vector pointing from the cation to the anion and the z-axis of the simulation cell (see Figure 5.8a). This order parameter is plotted along with the average number of SIPs as a function of the displacement from the instantaneous interface in Figure 5.8b and c for the $MgCl_2$ and $MgSO_4$ solutions, respectively.

In the $MgCl_2$ solution (Figure 5.8b), the number of SIPs shows a distinct peak between -3 Å to +2 Å followed by a small minimum. From -5 Å into the bulk, the number of SIPs is nearly constant. The orientational order parameter rises steeply from -0.5 Å to +1.5 Å. Positive values of $\langle \cos(\phi) \rangle$ indicate a net orientation of SIPs in which the vectors from the magnesium to the chloride ions are pointing toward the solution surface, reflecting the presence of the EDL. The small minimum from 3.5 Å to -0.5 Å corresponds to a weak net orientation in the opposite direction.

In the $MgSO_4$ solution (Figure 5.8c), the number of SIPs increases gradually starting at - 2 Å

131
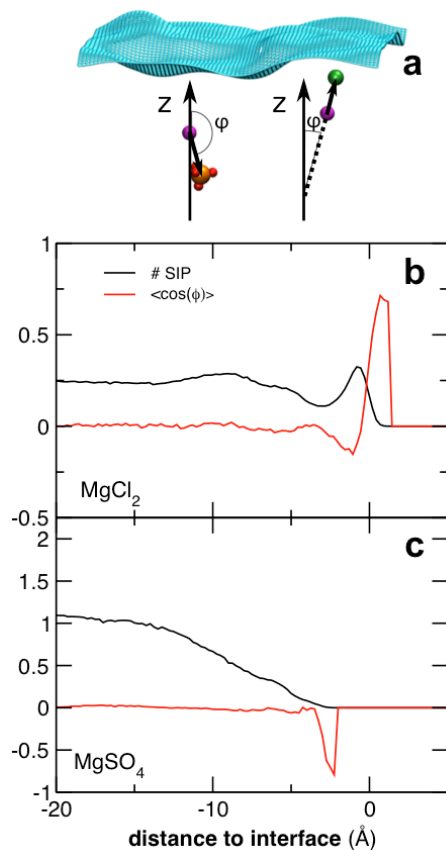
Figure 5.8: Schematic for the calculation of the SIP orientational order parameter with respect to the instantaneous interface. The Mg^{2+} ions are colored magenta, the SO_4^2 sulfur and oxygen atoms in orange and red, respectively, and the Cl ions in cyan. (b, c) Profiles of the number of SIPs and the order parameter plotted as a function of distance to the instantaneous interface for the $MgCl_2$ and $MgSO_4$ solutions, respectively. For the $MgCl_2$ and $MgSO_4$ solutions, the plots are histogrammed at the positions of the Cl^- and Mg^{2+} ions, respectively.

from the interface into the bulk. The orientational order parameter profile is flat, indicating a random orientation of SIPs, throughout most of the solution, except for between -3.5 Å to -2 Å, where it displays a sharp minimum. The negative value of the order parameter indicates a net orientation in which the vectors from the magnesium to the sulfate ions point away from the surface. Thus, near the interface, where the number of SIPs is very low, there is a strong preference for Mg^{2+} to reside closer to the interface than the SO_4^{2-}, resulting in a negative value of $\langle \cos(\phi) \rangle$. In conjunction with the electric field plots in Figure 5.7, it can be concluded that, while the occurrence of these SIPs in the interfacial region of the $MgSO_4$ solution is infrequent, they have a strong effect on the surface electric field.

5.5   Conclusions

Difference HD-VSFG spectra of water OH stretching vibrations are commonly used to infer the sign of the surface electric field and, hence, the distribution of ions at air-aqueous solution interfaces. According to the HD-VSFG spectra reported here, EDLs in which the anions are closer to the solutions surface than the cations, are formed near the interfaces of $MgCl_2$ and $Mg(NO_3)_2$ solutions. Our MD simulation of a $MgCl_2$ solution is consistent with this picture. In the case of $MgSO_4$ a negative difference Im $\chi^{(2)}$ response is observed which, using the same line of reasoning, suggests a reversal of the double layer, with the cations residing closer to the solutions surface than the anions. This is not borne out by our MD simulation of a $MgSO_4$ solution, where we observe that the distribution of both the cation and the anion is essentially the same, and neither ion closely approaches the solution surface.

Based on our simulations we propose an alternative, albeit less general, interpretation of the HD-VSFG spectrum of the $MgSO_4$ solution. We showed that the dominant contribution to the surface electric field acting on the water OH bonds comes from water molecules that are engaged in SIPs, and that the orientation of the SIPs is critical in determining the sign of the

contribution to the surface electric field. Thus, we conclude that the net orientation of SIPs in the interfacial region of the MgSO$_4$ solution can be inferred from the sign of the Im $\chi^{(2)}$ response measured in HD-VSFG experiments. Based on our limited observations, we do not know how general the connection is between SIPs and surface electric fields for solutions in which EDLs are not formed in the vicinity of the interface. Nonetheless, this study suggests that care should be taken when interpreting HD-VSFG spectra measured on salt solutions. In particular, the inferred surface fields might not be a consequence of the formation of an EDL.

The results reported herein provide new insights into the origin of the surface electric fields at the air -aqueous interfaces of salt solutions. Such insights could have significance to the atmospheric chemistry community, as surface electric fields may play a critical role in the electrification processes for thunderclouds. In addition, the potential growth of CCN could be considerably influenced as surface charge has strong implications for enhancing kinetics and selective adsorption of polar gas phase species.

Chapter 6

Nitric acid at the air/water interface

6.1 Introduction

Nitric acid is a naturally occurring molecule in the atmosphere, and can be found dissolved in aqueous aerosol particles. Upon equilibration in water, nitric acid loses a proton, resulting in four species in solution (HNO_3, NO_3^-, H_2O, H_3O^+), according to the following reaction:

$$HNO_3 + H_2O \rightleftharpoons NO_3^-{}_{(aq)} + H_3O^+_{(aq)}$$
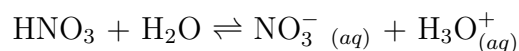
The distribution of these species in solution (with respect to the interface) mediate chemistry that occur on the surface, and therefore can have significant impacts on the complex chemistry of the atmosphere. If these species are present at the air/water interface, they are then free to participate in heterogeneous chemistry with gas-phase species. For example, studies have shown that undissociated nitric acid participates in renoxification reactions, and therefore acts as an important source of reactive nitrogen oxides in the atmosphere.[222] Additionally, the concentration of ozone in the troposphere is very sensitive to NO_x and

HNO_3 concentrations. Therefore, understanding the degree to which HNO_3 exists in the undissociated form at the air/water interface is a key factor in determining the contribution of dissolved HNO_3 from aqueous aerosols to the overall nitrate concentration in the atmosphere.

Numerous spectroscopic and experimental methods have been used to study liquid solutions of HNO_3 species, with somewhat inconclusive results.[6,7,8,9] For example, liquid-jet X-ray photoelectron spectroscopy (LJ-XPS) studies of aqueous HNO_3 solutions have been able to distinguish the degree of dissociation of the nitric acid species in solution via the N 1s binding energy.[11,10] In a combined LJ-XPS and molecular dynamics simulation study, the degree of dissociation of HNO_3 was shown to decrease in the interfacial region ($\sim$20% relative to bulk), and the degree of dissociation was shown to have significant concentration-dependence.[11,10]

Nonlinear spectroscopic methods, including VSFG and SHG studies, have been successful in detecting HNO_3 moities in the interfacial region, but the extent to which these methods can accurately detect HNO_3 concentrations, and the exact probe depth are unclear. For example, SHG studies have shown an appreciable concentration of NO_3^- at the air/water interface, but not enhanced relative to bulk concentrations.[223] Additionally, a VSFG study of binary HNO_3 - water systems concluded that two distinct hydrogen-bonded species of HNO_3 exist in the interfacial region, with the more hydrogen-bonded species residing deeper in the interfacial region.[224]

In conjunction with experimental spectroscopic studies, computational studies have been useful in determining the mechanism of nitric acid dissociation. For example, theoretical works highlight the importance of the solvation shell environment and hydrogen bonding between undissociated nitric acid and water in the interfacial region. For example, Wang et $al.$ show that, at the surface, undissociated nitric acid accepts two hydrogen bonds from water prior to dissociation.[225]

Lewis *et al.* show that molecular nitric acid (HNO_3) is stabilized near the air/water interface compared to in bulk solution, particularly at high concentration.[11] They suggest that in the low concentration regime, nitrate ion predominates over the molecular form due to the clathrate-like structure of the solvation shell around the nitrate species. The proposed reason for this suggests that at higher concentrations, solvation shells surrounding the nitrate species begin to overlap, therefore reducing the stability of the solvent environment surrounding the nitrate species, and the number of molecular nitric acid species increases.[10]

In this work, we study a concentrated aqueous nitric acid solution using *ab initio* molecular dynamics to assess the dissociation behavior of nitric acid in aqueous solution as a function of the distance to the interface. Here we implement the instantaneous definition of the interface, developed by William and Chandler[20] and discussed in detail elsewhere,[63,1] to give an enhanced resolution of the depth into solution (compared to the Gibbs dividing surface (GDS) definition.)

6.2 Methods

6.2.1 Simulation Details

The aqueous nitric acid solution was simulated using the simulation package CP2K (`http://cp2k.berlios.de`) for a total of approximately 200 ps with a timestep of 0.5 fs. The simulation cell was created by placing 14 nitric acid molecules and 156 water in a 15.0 Å × 15.0 Å × by 71.44 Å unit cell in the slab geometry. Two interfaces spontaneously formed above and below the solution slab perpendicular to the z-direction, resulting in a slab approximately 30 Å in length.

The simulation was run in the canonical ensemble and the temperature was held constant at

300 K using the Nose-Hoover thermostat.[226, 227] Forces were computed using the QuickStep module, which implements density functional theory using the dual basis sets of Gaussian type orbitals (TZ2V2P) and plane waves for the electron density.[228] The valence electrons were considered explicitly, and the core-electrons were represented via GTH psuedopotentials.[229] Grimme dispersion corrections were implemented in conjunction with the Becke exchange and Lee-Yang-Parr corelation functionals.[230, 231, 232] At each time step, the wave function was minimized to a tolerance of 10^{-6} H.

6.2.2 Instantaneous Interface

The instantaneous interface is defined at each timestep by constructing a coarse-grained density field by convoluting the position of the oxygen and nitrogen atoms with normalized Gaussians given by equation 6.1, where r is the position of the atom, α is the scaling parameter, and ζ is the Gaussian half-width.[20] Convolution parameters were chosen such that the bulk density of the solution does not contain any large "holes" or deficits in density, and are summarized below in Table 6.1. The interface is then determined by parsing the density field in the z-direction to find an isodensity contour in x and y where the density is equal to half that of the bulk solution.

$$\phi(r; \alpha, \zeta) = \frac{\alpha}{(2\pi\zeta^2)^{3/2}} exp\left(\frac{-r^2}{2\zeta^2}\right) \tag{6.1}$$

Species	Molecule	q (e$^-$)	ξ (Å)	η
OW	H_2O/H_3O^+	-0.8476	2.4	1.0
HW	H_2O/H_3O^+	+0.4238	-	-
HP	H_3O^+	+1.0	-	-
NN	HNO_3/NO_3^-	-0.8476	2.4	1.0
ON	HNO_3/NO_3^-	-0.8476	2.4	1.0
HN	HNO_3	+0.4238	-	-

Table 6.1: Convolution parameters

Molecule	Num. Density (Å^{-3})
HNO_3	0.000166
NO_3^-	0.002737
H_2O	0.024598
H_3O^+	0.0002737

Table 6.2: Bulk concentrations of each molecule type.

6.3   Results & Discussion

6.3.1   Density Profiles and Speciation of Nitric Acid Species.

Because we perform the simulation using CP2K, the HNO_3 molecule can freely dissociate during the course of the simulation, resulting in both the HNO_3 (undissociated) and the NO_3^- (dissociated) moities. The first task in the analysis of the simulation is to differentiate between the two nitric acid moities. In Figure 6.1 we plot the probability distribution of the distance between the nitric acid oxygens (which we will refer to as ON) to the nearest hydrogen as a function of the distance to the instantaneous interface. A bimodal distribution is observed when considering cross-sections perpendicular to the z-axis.

The peak corresponding to the shorter ON-H distance is centered at 1.25 Å indicating that the cutoff distance between the ON-H of the undissociated nitric acid falls between $\sim$ 0.5 Å and 1.25 Å. Therefore, any nitric acid species in which the distance between the nearest hydrogen to any nitric acid oxygen (ON) is greater than 1.25 Å is considered a dissociated

nitric acid species (NO_3^-). The remaining population of the nitric acid species are considered the undissociated HNO_3 molecule.

From this plot, three distinct layers of the nitric acid species are observed along the z-direction. We separate the layers at the minima observed in the PDF distribution along the z-direction, into "bulk", "middle" and "surface" regions. The bulk region is defined for distances to the interface z > 8 Å, the middle is defined from 8 Å $\leq$ z < 5 Å, and the surface is defined from 5 Å $\leq$ z < 0.
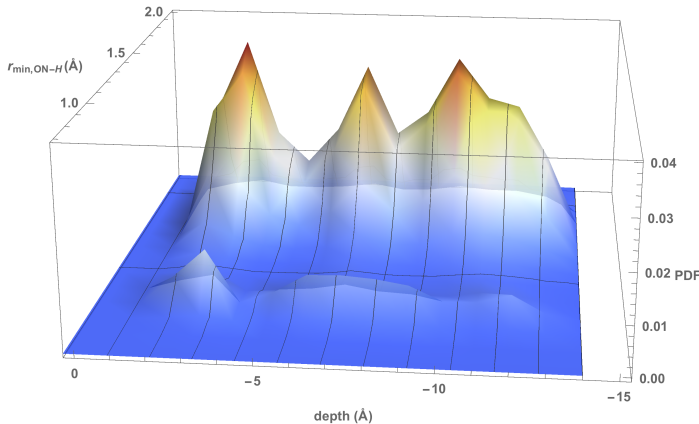
Figure 6.1: PDF of $r_{min(O-H)}$ vs. distance to instantaneous interface. Two dimensional probability distribution of the minimum radial distance of hydrogen closest to oxygen on any nitric acid species (HNO_3 and NO_3^- as a function of the distance to the instantaneous interface.

In Figure 6.2, density profiles of each molecular species are plotted as a function of the distance to the instantaneous interface. The concentration of undissociated nitric acid is very low relative to the other molecular components, therefore the profile of undissociated nitric acid (HNO_3) is magnified 10× to reveal detail. The large peak in the HNO_3 profile indicates a large enhancement (relative to bulk) in the interfacial region and suggests that the undissociated nitric acid prefers to reside $\sim$ 2.5 Å from the interface.

Both H_3O^+ and NO_3^- show little affinity for the interface (relative to their bulk concentrations), with H_3O^+ approaching the interface slightly closer than NO_3^-. It is suprising then that SHG studies have shown NO_3^- present at the interface, but this could be explained with
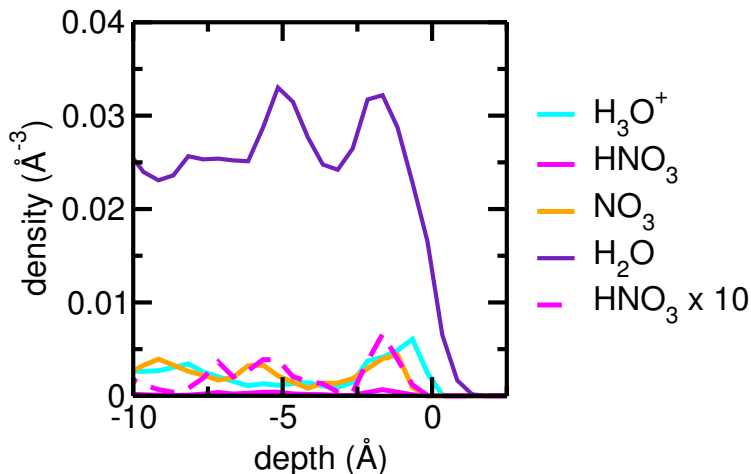
Figure 6.2: Density profiles of all molecule types in aqueous nitric acid solution, plotted with respect to the instantaneous interface.

a probe depth extending well into what we define here as the middle region.

A useful quantity for assessing the degree of dissociation of the nitrate species, α is defined as follows in Equation 6.2.

$$\alpha = \frac{[NO_3^-]}{[NO_3^-] + [HNO_3]} \tag{6.2}$$

Upon equilibration, the total concentration of nitric acid (both dissociated and undissociated) in the bulk was determined to be 4.82 mol/L, which decreases to 2.94 mol/L in the surface region. At this concentration, the bulk density was calculated to be 1.12 g cm^{-3}, which agrees quite well with the experimental measurement of 1.16 g cm^{-3}.[233]

While the overall concentration of nitric acid species decreases at the interface, the degree of dissociation α (defined in Eq. 6.2) decreases for HNO$_3$ species closer to the interface, with α ranging from 0.96 in the bulk, 0.90 in the middle, and 0.83 in the surface region. This indicates that the proportion of undissociated HNO$_3$ relative to the dissociated form

predominates in the interfacial region.

6.3.2   Hydrogen Bonding Environment of Molecular HNO$_3$

In order to investigate this decreased degree of dissociation in the interfacial region, we consider the number of hydrogen bonds made between water and molecular nitric acid in the various regions of solution.
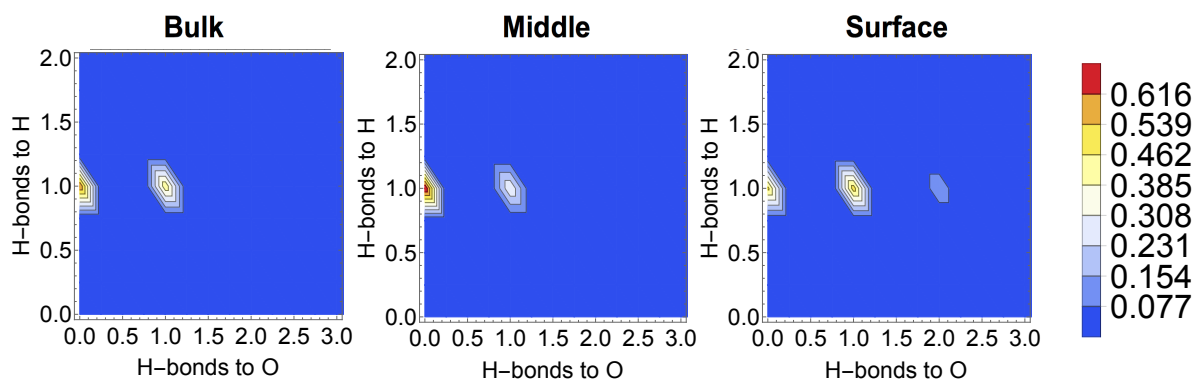
Figure 6.3: Contour plots showing hydrogen bonding configurations for the HNO$_3$ species in the bulk, middle, and surface regions of the slab. The number of hydrogen bonds to Hydrogen and Oxygen are calculated per undissociated HNO$_3$ molecule.

In Figure 6.3, contour plots depict the hydrogen-bonding environment of the HNO$_3$ species in the bulk, middle, and surface regions. In all three regions (surface, middle, bulk), the hydrogen of the nitric acid molecule is always acting as a hydrogen bond donor to one water molecule. In each of the regions, distinct hydrogen-bonding configurations are observed for the nitric acid oxygens acting as hydrogen-bond acceptors.

In the bulk region, a bimodal distribution is observed, with the nitric acid oxygen accepting either one or zero hydrogen bonds. The distribution is slightly weighted toward the configuration where the oxygen accepts zero hydrogen bonds relative to the configuration in which it accepts one hydrogen bond. In the middle region, the bimodal distribution shifts toward the configuration in which HNO$_3$ accepts zero hydrogen bonds compared to the configuration

in which HNO$_3$ accepts one hydrogen bond. In the surface region, a third configuration is observed in which the distribution shifts toward the nitric acid oxygen accepting zero and one hydrogen bond with approximately equal probability, and a small proportion of the time, accepting two hydrogen bonds.

We compare these findings to the results of Ref. 224, in which the authors observed two distinct hydrogen-bonding configurations in the interfacial region, with one configuration having one ON-HW and one HN-OW bond, and the other having only the single HN-OW bond. They acknowledge the possibility of a third hydrogen configuration in which a second ON-HW bond exists, but argue that it is not a "good" hydrogen bond because of the long ON-HW bond length. While the low probability of finding the triply hydrogen-bonded configuration observed here is in agreement with the results of Ref. 224, we do not observe a significantly stretched bond length for the second ON-HW bond in this configuration.

In Figure 6.4, a snapshot of the solvation shell surrounding HNO$_3$ (left) and a hydrogen-bonding configuration are shown (right). In the right panel, the triply hydrogen-bonded configuration is shown, with the two ON-HW bonds equal in length (2.2 Å). In the left panel, the waters participating in the solvation shell of HNO$_3$ are shown in cyan, as further discussed in the next section.

6.3.3 Solvation Shell of HNO$_3$ and Ion Pairing Between NO$_3^-$ and H$_3$O$^+$

In Figure 6.5, characteristics of both the solvation shell and ion pairing of the nitric acid species are further investigated. In the left panel of Figure 6.5, the number of ion pairs between NO$_3^-$ and H$_3$O$^+$ are calculated as a function of the distance of the NO$_3^-$ molecule to the instantaneous interface. Here the distance between NO$_3^-$ and H$_3$O$^+$ in an ion pair was determined by finding the minimum in the NN - OW radial distribution function (approxi-
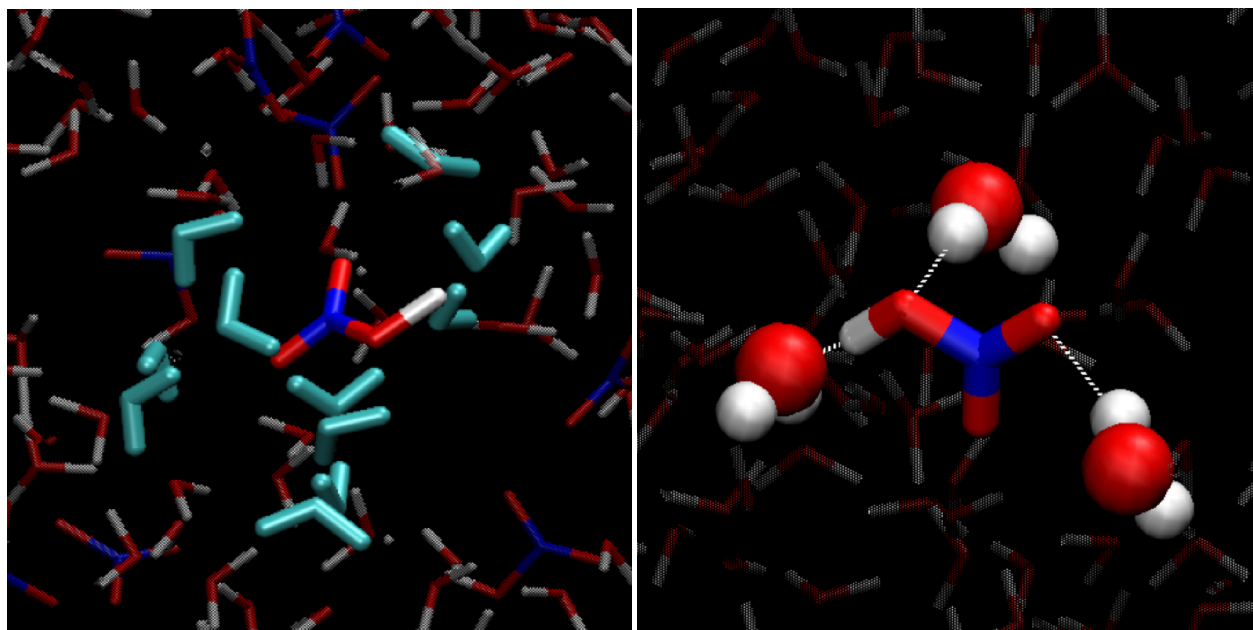
Figure 6.4: (Left) Snapshot of waters in the solvation shell of HNO$_3$ molecule. Water molecules are shown in cyan, the molecular nitric acid is shown in red, blue and white.(Right) Snapshot of molecular nitric acid acting as both a hydrogen-bond donor and acceptor. The hydrogen acts as a hydrogen-bond donor to an oxygen atom on a nearby water molecule, while two of the oxygens of the nitric acid molecule accept a hydrogen-bond from hydrogen of nearby water molecules.

mately 3.6 Å apart). Ion pairing is quite rare irrespective of position, but some structuring is evident. In the surface region, no ion pairing is observed. Deeper in to solution, approximately 5 Å from the instantaneous interface, NO$_3^-$ participates in an ion pair $\sim$ 42% of the time. At this distance from the interface, the NO$_3^-$ molecule would fall on the border of the middle and surface region. A clear minimum is observed in the ion pairing profile approximately 8 Å which coincides with the border line between the middle and bulk regions. In the bulk region, ion pairing occurs between $\sim$ 1-3 % of the time, with a slight increase in ion pairing deeper into solution.

In the right panel of Figure 6.5, the probability distribution of the number of waters in a solvation shell of an oxygen on HNO$_3$ molecule is shown for each of the solution layers. In this analysis, the solvation shell is defined as a water within 3.7 Å from any of the HNO$_3$ oxygen. This cutoff was determined by finding the first minimum in the radial distribution

144
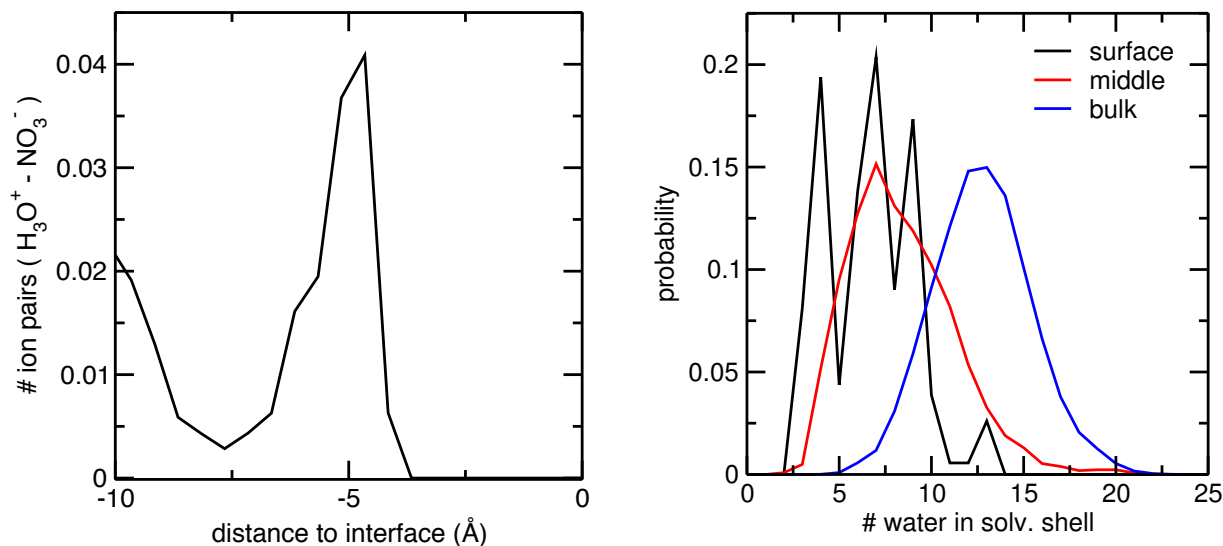
Figure 6.5: (Left) Ion pairing between NO_3^- and H_3O^+ plotted as a function of the distance of the NO_3^- molecule to the instantaneous interface. (Right) Probability distribution of the solvation shell surrounding any oxygen atom on an HNO_3 molecule in the bulk, middle, and surface regions.

function between nitric acid (either moiety) oxygen (ON) and water oxygen (OW).

In the middle and bulk regions, the probability of the number of waters participating in a solvation shell of HNO_3 appear as unimodal distributions with maxima at 7 and 13, respectively. In the surface region, the distribution becomes trimodal, with three distinct peaks centered at 4, 7 and 9 waters in the solvation shell. While the surface distribution is more structured than the middle region, the surface and middle regions overlap considerably, with the middle distribution having a shoulder that extends to larger solvation shells.

These three distinct configurations in the surface region suggest that structuring of the solvation shell arises near the interface. The fact that HNO_3 shows a configuration in which only 4 water molecules participate in the solvation shell is in agreement with the conclusion of Ref. 223 that shows that HNO_3 must have at minimum 5 waters for dissociation. With only 4 waters in the solvation shell, HNO_3 is therefore undersolvated and stabilized in the molecular form. Further exploration of the precise solvation shell structure is needed to

characterize the configurations that serve to stabilize the HNO_3 molecule in regions where the number of waters available to participate in the solvation shell decreases.

6.4   Conclusions

In this work, we show unambiguously, that molecular nitric acid exists at the air/water interface of concentrated aqueous solution. Using the instantaneous interface definition, we have an enhanced resolution of the interfacial region and therefore can distinguish differences in the solvation environment of the molecular nitric acid.

Within the interfacial region, the molecular form is stabilized by 1 or 2 hydrogen bonds between the nitric acid oxygens and water hydrogens, as well as a single hydrogen bond between the nitric acid proton to water oxygens. Additionally, we observe a clear structuring of the solvation shell surrounding the molecular nitric acid molecule in the interfacial region, with the nitric acid remaining undissociated with a solvation shell of 4 water molecules. As the undissociated nitric acid moves deeper into solution, the number of waters participating in the solvation shell increases to, on average, 13 water molecules.

Bibliography

[1] Giorgia Olivieri, Krista M. Parry, Cedric J. Powell, Douglas J. Tobias, and Matthew A. Brown. Quantitative interpretation of molecular dynamics simulations for x-ray photoelectron spectroscopy of aqueous solutions. *The Journal of Chemical Physics*, 144(15):154704, 2016.

[2] G. Olivieri, K. M. Parry, R. D'Auria, D. J. Tobias, and M.A. Brown. Specific anion effects on na$^+$ adsorption at the aqueous solutionair interface: Md simulations, sessa calculations, and photoelectron spectroscopy experiments. *J. Phys. Chem. B*, XX:XX–XX, 2017.

[3] K. A. Perrine, K. M. Parry, A. C. Stern, M. H. C. Van Spyk, M. J. Makowski, J. A. Freites, B. Winter, D. J. Tobias, and J. C. Hemminger. Specific cation effects at aqueous solutionvapor interfaces: Surfactant-like behavior of li+ revealed by experiments and simulations. *Proc. Natl. Acad. Sci. USA*, XX:XX–XX, 2017.

[4] L. Götte, K. M. Parry, D. Verreault, H. C. Allen, and D. J. Tobias. Solvent-shared ion pairs at the airsolution interface of magnesium chloride and sulfate solutions revealed by sum frequency spectroscopy and molecular dynamics simulations. *J. Phys. Chem. A*, 121:6450–6459, 2017.

[5] Hofmeister F. Zur lehre von der wirkung der salze. *Arch. Exp. Pathol. Pharmakol.*, 24:247–260, 1888.

[6] G. C. Hood, O. Redlich, and C. A. Reilly. Ionization of strong electrolytes. iii. proton magnetic resonance in nitric, perchloric, and hydrochloric acids. *J. Chem. Phys.*, 22:2067, 1954.

[7] H.A.C. McKay. The activity coefficient of nitric acid, a partially ionized 1:1-electrolyte. *Trans. Faraday Soc.*, 52:1568, 1956.

[8] W. Jr. Davis and H. J. De Bruin. New activity coefficients of 0-200 per cent aqueous nitric acid. *J. Inorg. Nuel. Chem.*, 26:1069–1083, 1964.

[9] O. Redlich, R. W. Duerst, and A. Merbach. Ionization of strong electrolytes. xi. the molecular states of nitric acid and perchloric acid. *J. Chem. Phys.*, 49:2986, 1968.

[10] T. Lewis, B. Winter, A. C. Stern, M. D. Baer, C. J. Mundy, D. J. Tobias, and J. C. Hemminger. Dissociation of strong acid revisited: X-ray photoelectron spectroscopy and molecular dynamics simulations of hno3 in water. *J. Phys. Chem. B*, 115:9445–9451, 2011.

[11] T. Lewis, B. Winter, A. C. Stern, M. D. Baer, C. J. Mundy, D. J. Tobias, and J. C Hemminger. Does nitric acid dissociate at the aqueous solution surface? *J. Phys. Chem. C*, 115:21183–21190, 2011.

[12] E. M. Knipping, M. J. Lakin, K. L. Foster, P. Jungwirth, D. J. Tobias, R. B. Gerber, D. Dabdub, and B. J. Finlayson-Pitts. Experiments and simulations of ion-enhanced interfacial chemistry on aqueous nacl aerosols. *Science*, 288(5464):301–306, 2000.

[13] C. W. Spicer, E. G. Chapman, B. J. Finlayson-Pitts, R. A. Plastridge, J. M. Hubbe, J. D. Fast, and C. M. Berkowitz. Unexpectedly high concentrations of molecular chlorine in coastal air. *Nature*, 394(6691):353–356, 1998.

[14] S. M. Kathmann, I. F. W. Kuo, and C. J. Mundy. Electronic effects on the surface potential at the vapor-liquid interface of water. *Journal of the American Chemical Society*, 130(49):16556–16561, 2008.

[15] V. Buch, A. Milet, R. Vacha, P. Jungwirth, and J. P. Devlin. Water surface is acidic. *Proceedings of the National Academy of Sciences of the United States of America*, 104(18):7342–7347, 2007.

[16] H. Mishra, S. Enami, R. J. Nielsen, L. A. Stewart, M. R. Hoffmann, W. A. Goddard, and A. J. Colussi. Bronsted basicity of the air-water interface. *Proceedings of the National Academy of Sciences of the United States of America*, 109(46):18679–18683, 2012.

[17] R. J. Saykally. Air/water interface two sides of the acid-base story. *Nature Chemistry*, 5(2):82–84, 2013.

[18] L. Vrbka, J. Vondrasek, B. Jagoda-Cwiklik, R. Vacha, and P. Jungwirth. Quantification and rationalization of the higher affinity of sodium over potassium to protein surfaces. *Proceedings of the National Academy of Sciences of the United States of America*, 103(42):15440–15444, 2006.

[19] C. M. Johnson and S. Baldelli. Vibrational sum frequency spectroscopy studies of the influence of solutes and phospholipids at vapor/water interfaces relevant to biological and environmental systems. *Chemical Reviews*, 114(17):8416–8446, 2014.

[20] A. P. Willard and D. Chandler. Instantaneous liquid interfaces. *J. Phys. Chem. B*, 114:1954–1958, 2010.

[21] G. Olivieri, K. M. Parry, C. J. Powell, D. J. Tobias, and M.A. Brown. Simulated photoelectron intensities at the aqueous solutionair interface for flat and cylindrical (microjet) geometries. *Phys. Chem. Chem. Phys.*, 19:6330–6333, 2017.

[22] D. J. Tobias, A. C. Stern, M. D. Baer, Y. Levin, and C. J. Mundy. Simulation and theory of ions at atmospherically relevant aqueous liquid-air interfaces. *Annu. Rev. Phys. Chem.*, 64:339–359, 2013.

[23] P. Jungwirth and D. J. Tobias. Specific ion effects at the air/water interface. *Chem. Rev.*, 106:1259–1281, 2006.

[24] S. Ghosal, J. C. Hemminger, H. Bluhm, B. S. Mun, E. L. D. Hebenstreit, G. Kettler, D. F. Ogletree, F. G. Requejo, and M. Salmeron. Electron spectroscopy of aqueous solution interfaces reveals surface enhancement of halides. *Science*, 307:563–566, 2005.

[25] B. Winter, R. Weber, P. M. Schmidt, I. V. Hertel, M. Faubel, L. Vrbka, and P. Jungwirth. Photoemission from liquid aqueous solutions: Photoelectron spectroscopy and molecular dynamics simulations of aqueous tetrabutylammonium iodide. *J. Phys. Chem. B*, 108:14558–14564, 2004.

[26] E. A. Raymond and G. L. Richmond. Probing the molecular structure and bonding of the surface of aqueous salt solutions. *J. Phys. Chem. B*, 108:5051–5059, 2004.

[27] D. Liu, G. Ma, L. M. Levering, and H. C. Allen. Vibrational spectroscopy of aqueous sodium halide solutions and air-liquid interfaces: Observation of increased interfacial depth. *J. Phys. Chem. B*, 108:2252–2260, 2004.

[28] Poul B. Petersen and Richard J. Saykally. Evidence for an enhanced hydronium concentration at the liquid water surface. *J. Phys. Chem. B*, 109(16):7976–7980, 2005.

[29] P. B. Petersen, J. C. Johnson, K. P. Knutsen, and R. J. Saykally. Direct experimental validation of the Jones-Ray effect. *Chem. Phys. Lett.*, 397:46–50, 2004.

[30] Poul B. Petersen and Richard J. Saykally. Confirmation of enhanced anion concentration at the liquid water surface. *Chem. Phys. Lett.*, 397:51–55, 2004.

[31] Y. Zhang and P. S. Cremer. Chemistry of hofmeister anions and osmolytes. *Annu. Rev. Phys. Chem.*, 61:63–83, 2010.

[32] Barbara J. Finlayson-Pitts and James N. Pitts Jr. *Chemistry of the Upper and Lower Atmosphere.* Academic Press, 2000.

[33] Douglas J. Tobias and John C. Hemminger. Chemistry - getting specific about specific ion effects. *Science*, 319(5867):1197–1198, 2008.

[34] E. M. Knipping and D. Dabdub. Impact of chlorine emissions from sea-salt aerosol on coastal urban ozone. *Environ. Sci. Technol.*, 37:275–284, 2003.

[35] S. W. Hunt, M. Roeselova, W. Wang, L. M. Wingen, E. M. Knipping, D. J. Tobias, D. Dabdub, and B. J. Finlayson-Pitts. Formation of molecular bromine from the reaction of ozone with deliquesced nabr aerosol: Evidence for interface chemistry. *Journal of Physical Chemistry A*, 108:11559–11572, 2004.

[36] B. J. Finlayson-Pitts and John C. Hemminger. Physical chemistry of sea salt particles and their components. *J. Phys. Chem. A*, 104:11463–11477, 2000.

[37] Bernd Winter and Manfred Faubel. Photoemission from liquid aqueous solutions. *Chem. Rev.*, 106(4):1176–1211, 2006.

[38] P. Jungwirth and B. Winter. Ions at aqueous interfaces: From water surface to hydrated proteins. *Annu. Rev. Phys. Chem.*, 59:343–366, 2008.

[39] Phillip L. Geissler. Water interfaces, solvation, and spectroscopy. *Ann. Rev. Phys. Chem.*, 64(1):317–337, 2013.

[40] T. Ishiyama and A. Morita. Molecular dynamics study of gas-liquid aqueous sodium halide interfaces. i. flexible and polarizable molecular modeling and interfacial properties. *J. Phys. Chem. C*, 111:721–737, 2007.

[41] M. A. Brown, B. Winter, M. Faubel, and J. C. Hemminger. Spatial distribution of nitrate and nitrite anions at the liquid/vapor interface of aqueous solutions. *J. Am. Chem. Soc.*, 131:8354–8355, 2009.

[42] V. Ostroverkhov, G. A. Waychunas, and Y. R. Shen. New information on water interfacial structure revealed by phase-sensitive surface spectroscopy. *Phys. Rev. Lett.*, 94:046102, 2005.

[43] N. Ji, V. Ostroverkhov, and C. Y. Chen Y. R. Shen. Phase-sensitive sum-frequency vibrational spectroscopy and its application to studies of interfacial alkyl chains. *J. Am. Chem. Soc.*, 129(33):10056–10057, 2007.

[44] C. S. Tian and Y. R. Shen. Sum-frequency vibrational spectroscopic studies of water/vapor interfaces. *Chem. Phys. Lett.*, 470:1–6, 2009.

[45] M. H. Cheng, K. M. Callahan, A. M. Margarella, D. J. Tobias, J. C. Hemminger, H. Bluhm, and M. J. Krisch. Ambient pressure x-ray photoelectron spectroscopy and molecular dynamics simulation studies of liquid/vapor interface of aqueous nacl, rbcl, and rbbr solutions. *J. Phys. Chem. C*, 116:4545–4555, 2012.

[46] N. Ottosson, M. Faubel, S. E. Bradforth, P. Jungwirth, and B. Winter. Photoelectron spectroscopy of liquid water and aqueous solution: Electron effective attenuation lengths and emission-angle anisotropy. *J. Electron Spectrosc.*, 177:60–70, 2010.

[47] Manfred Faubel, Björn Steiner, and J. Peter Toennies. Photoelectron spectroscopy of liquid water, some alcohols, and pure nonane in free micro jets. *J. Chem. Phys.*, 106:9013, 1997.

[48] Richard L. Kurtz, Noriaki Usuki, Roger Stockbauer, and Theodore E. Madey. Measurements of electron attenuation lengths in condensed molecular solids. *J. Electron. Spectrosc. Relat. Phenom.*, 40:35–58, 1986.

[49] M. P. Seah and W. A. Dench. Quantitative electron spectroscopy of surfaces:a standard data base for electron inelastic mean free paths in solids. *Surface and Interface Analysis*, 1(1):2–11, 1979.

[50] M. Michaud, A. Wen, and L. Sanche. Cross sections for low-energy (1-100 ev) electron elastic and inelastic scattering in amorphous ice. *Radiation Research*, 159:3–22, 2003.

[51] S. Tanuma, C. J. Powell, and D. R. Penn. Calculations of electron inelastic mean free paths. ix. data for 41 elemental solids over the 50 ev to 30 kev range. *Surf. Interface Anal.*, 43:689–713, 2011.

[52] A. Jablonski and C. J. Powell. Relationships between electron inelastic mean free paths, effective attenuation lengths, and mean escape depths. *J. Elec. Spec.*, 100:137–160, 1999.

[53] I. Lindau and W. E. Spicer. The probing depth in photoemission and auger-electron spectroscopy. *J. Electron Spectrosc.*, 3:409, 1974.

[54] C. J. Powell. Attenuation lengths of low-energy electrons in solids. *Surf. Sci.*, 44:29, 1974.

[55] Nist electron inelastic-mean-free-path database, version 1.1. National Institute of Stadnard and Technology, Gaithersburg, MD, 2000.

[56] D. Emfietzoglou, I. Kyriakou, I. Abril, R. Garcia-Molina, I. D. Petsalakis, H. Nikjoo, and A. Pathak. Electron inelastic mean free paths in biological matter based on dielectric theory and local-field corrections. *Nucl. Instrum. Methods Phys. Res., Sect. B*, 267:45–52, 2009.

[57] L. Vrbka, M. Mucha, B. Minofar, P. Jungwirth, E. C. Brown, and D. J. Tobias. Propensity of soft ions for the air/water interface. *Curr. Opin. Colloid Interface Sci.*, 9(1-2):67–73, 2004.

[58] L. Perera and M. L. Berkowitz. Many-body effects in molecular dynamics simulations na$^+$(h$_2$o)$_n$ and cl$^-$(h$_2$o)$_n$ clusters. *J. Chem. Phys.*, 95:1954–1963, 1991.

[59] P. Jungwirth and D. J. Tobias. Molecular structure of salt solutions: A new view of the interface with implications for heterogeneous atmospheric chemistry. *Journal of Physical Chemistry B*, 105:10468–10472, 2001.

[60] D. Horinek, A. Herz, L. Vrbka, F. Sedlmeier, S. I. Mamatkulov, and R. R. Netz. Specific ion adsorption at the air/water interface: The role of hydrophobic solvation. *Chem. Phys. Lett.*, 479:173–183, 2009.

[61] D. Horinek, S. I. Mamatkulov, and R. R. Netz. Rational design of ion force fields based on thermodynamic solvation properties. *J. Chem. Phys.*, 130:124507, 2009.

[62] J. Noah-Vanhoucke and P. L. Geissler. On the fluctuations that drive small ions toward, and away from, interfaces between polar liquids and their vapors. *Proc. Natl. Acad. Sci. USA*, 106:15125–15130, 2009.

[63] A. C. Stern, M. D. Baer, C. J. Mundy, and D. J. Tobias. Thermodynamics of iodide adsorption at the instantaneous air-water interface. *J. Chem. Phys.*, 138, 2013.

[64] B. Hess, C. Kutzner, D. Vanderspol, and E. Lindahl. Gromacs 4: Algorithms for highly efficient, load-balanced, and scalable molecular simulation. *J. Chem. Theory Comput.*, 4:435–447, 2008.

[65] T. Darden, D. York, and L. Pedersen. Particle mesh ewald: An n log (n) method for ewald sums in large systems. *J. Chem. Phys.*, 98:10089, 1993.

[66] H. J. Berendsen, J. R. Grigera, and T. P. Straatsma. The missing term in effective pair potentials. *J. Phys. Chem-Us*, 91:6269–6271, 1987.

[67] N. Matubayasi. *Surface Tension and Related Thermodynamic Quantities of Aqueous Electrolyte Solutions.* CRC Press, Boca Raton, 2013.

[68] K. Ali, A. U. H. A. Shah, S. Bilal, and Shah A. U. H. A. Surface tensions and thermodynamic parameters of surface formation of aqueous salt solutions: Iii. aqueous solution of kcl, kbr and ki. *Colloid Surface A*, 337:194–199, 2009.

[69] H. Ted Davis. Capillary waves and the mean field theory of interfaces. *J. Chem. Phys.*, 67(8):3636–3641, 1977.

[70] Oneka T. Cummings and Collin D. Wick. Interfacial behavior of simple inorganic salts at the air-water interface investigated with a polarizable model with electrostatic damping. *J. Chem. Phys.*, 139:064708, 2013.

[71] Xiaohu Li and George C. Schatz. Osmolytic co-solute perturbing the surface enhancement of halide ions. *J. Phys. Chem. Lett.*, 4:2285–2889, 2013.

[72] M. J. Krisch, R. D'Auria, M. A. Brown, D. J. Tobias, J. C. Hemminger, M. Ammann, D. E. Starr, and H. Bluhm. The effect of an organic surfactant on the liquidvapor interface of an electrolyte solution. *J. Phys. Chem. C*, 111:13497–13509, 2007.

[73] Song Hi Lee and Jayendran C. Rasaiah. Molecular dynamics simulation of ionic mobility. i. alkali metal cations in water at 25 ° c. *J. Chem. Phys.*, 101:6964, 1994.

[74] Peter A. Kollman and Irwin D. Kuntz. Cation hydration. *J. Am. Chem. Soc.*, 94:9236–9237, 1972.

[75] Bernd Winter, Emad F. Aziz, Uwe Hergenhahn, Manfred Faubel, and Ingolf V. Hertel. Hydrogen bonds in liquid water studied by photoelectron spectroscopy. *J. Chem. Phys.*, 126:124504, 2007.

[76] A. Akkerman and E. Akkerman. Characteristics of electron inelastic interactions in organic compounds and water over the energy range 20–10000 ev. *J. Applied Phys.*, 86:5809–5816, 1999.

[77] S. Thurmer, R. Seidel, M. Faubel, W. Eberhardt, J. C. Hemminger, S. E. Bradforth, and B. Winter. Photoelectron angular distributions from liquid water: Effects of electron scattering. *Phys. Rev. Lett.*, 111, 2013.

[78] C. J. Powell and A. Jablonski. Surface sensitivity of x-ray photoelectron spectroscopy. *Nucl. Instrum. Meth. A.*, 601:54–65, 2009.

[79] C. J. Powell and A. Jablonski. Progress in quantitative surface analysis by x-ray photoelectro spectroscopy: Current status and perspectives. *J. Electron. Spectrosc.*, 178:331–346, 2010.

[80] S. Tanuma, C. J. Powell, and D. R. Penn. Calculations of electron inelastic mean free paths. v. data for 14 organic compounds over the 502000 ev range. *Surf. Interface Anal.*, 21:165–176, 1994.

[81] M. P. Seah. An accurate and simple universal curve for the energy-dependent electron inelastic mean free path. *Surf. Interface Anal.*, 44:497–503, 2012.

[82] C. J. Powell and A. Jablonski. Evaluation of calculated and measured electron inelastic mean free paths near solid surfaces. *J. Phys. Chem. Ref. Data*, 1:19–62, 1999.

[83] Y. I. Suzuki, K. Nishizawa, N. Karuhashi, and Suzuki T. Effective attenuation length of an electron in liquid water between 10 and 600 ev. *Phys. Rev. E*, 90, 2014.

[84] D. Emfietzoglou, I. Kyriakou, I. Abril, R. Garcia-Molina, I. D. Petsalaki, H. Nikjoo, and A. Pathak. Photoelectron angular distributions from liquid water: Effects of electron scattering. *Nucl. Instrum. Meth. B*, 267:45–52, 2009.

[85] I. Jordan, A. B. Redondo, M. A. Brown, D. Fodor, M. Staniuk, A. Kleibert, H. J. Worner, J. B. Giorgi, and J.A. van Bokhoven. Non-uniform spatial distribution of tin oxide (sno₂) nanoparticles at the airwater interface. *Chem. Commun.*, 50:4242–4244, 2014.

[86] S. Ghosal, M. A. Brown, H. Bluhm, M. J. Krisch, M. Salmeron, P. Jungiwrth, and J. C. Hemminger. Ion partitioning at the liquid/vapor interface of a multicomponent alkali halide solution: A model for aqueous sea salt aerosols. *J. Phys. Chem. A*, 112:12378–12384, 2008.

[87] M. H. Cheng, K. M. Callahan, A. M. Margarella, D. J. Tobias, M. Ammann, D. E. Starr, and H. Bluhm. Ambient pressure x-ray photoelectron spectroscopy and molecular dynamics simulation studies of liquid/vapor interfaces of aqueous nacl, rbcl, and rbbr solutions. *J. Phys. Chem. C*, 116:4545–4555, 2012.

[88] W. Smekal, W. S. M. Werner, and C. J. Powell. Simulation of electron spectra for surface analysis (sessa): a novel software tool for quantitative auger-electron spectroscopy and x-ray photoelectron spectroscopy. *Surf. Interface Anal.*, 37:1059–1067, 2005.

[89] W. S. M. Werner, W. Smekal, and C. J. Powell. NIST Database for the Simulation of Electron Spectra for Surface Analysis, Version 2.0, Standard Reference Data program Database 100. Department of Commerce, National Institute of Standard and Technology, 2014.

[90] D. Vanderspoel, E. Lindahl, B. Hess, G. Groenhof, A. E. Mark, and H. J. C. Berendsen. Gromacs: Fast, flexible, and free. *J. Comput. Chem.*, 26:1701–1718, 2005.

[91] W. F. Vangunsteren, H. J. C. Berendsen, and R. Vandrunen. Computer simulation of molecular dynamics: Methodology, applications, and perspectives in chemistry. *Angewandte Chemie-International Edition*, 29:992–1023, 1990.

[92] H. J. C. Berendsen, D. Vanderspoel, and R. Vandrunen. Gromacs: A message-passing parallel molecular dynamics implementation. *Comput. Phys. Commun.*, 91:43–56, 1995.

[93] E. Lindahl, B. Hess, and D. Vanderspoel. Gromacs 3.0: a package for molecular simulation and trajectory analysis. *J. Mol. Model.*, 7:306–317, 2001.

[94] G. Bussi, D. Donadio, and M. Parrinello. Canonical sampling through velocity rescaling. *J. Chem. Phys.*, 126, 2007.

[95] U. Essmann, L. Perera, M. L. Berkowitz, T. Darden, H. Lee, and L. G. Pedersen. A smooth particle mesh ewald method. *J. Chem. Phys.*, 103:8577–8593, 1995.

[96] S. Miyamoto and P. A. Kollman. Settle: An analytical version of the shake and rattle algorithm for rigid water models. *J. Comput. Chem.*, 13:952–962, 1992.

[97] E. W. Washburn. International critical tables of numerical data, physics, chemistry, and technology. McGraw-Hill, New York, 1928.

[98] P. O. N. Sohnel. Densities of aqueous solutions of inorganic substances. Elsevier Science, Amsterdam, 1985.

[99] S. Tanuma, C. J. Powell, and D. R. Penn. Calculations of electron inelastic mean free paths. *Surf. Interface Anal.*, 37:1–14, 2005.

[100] M. A. Brown, A. B. Redondo, I. Jordan, N. Duyckaerts, M. T. Lee, M. Ammann, F. Nolting, A. Kleibert, T. Huthwelker, J. P. Machler, M. Birrer, J. Honegger, R. Wetter, H. J. Worner, and J. A. van Bokhoven. A new endstation at the swiss light source for ultraviolet photoelectron spectroscopy, x-ray photoelectron spectroscopy, and x-ray absorption spectroscopy measurements of liquid solutions. *Rev. Sci. Instrum.*, 84, 2013.

[101] J. J. Yeh and I. Lindau. Atomic subshell photoionization cross sections and asymmetry parameters: 1 < z < 103. *Atom. Data Nucl. Data*, 32:1–155, 1985.

[102] Surface chemical analysis- vocabulary - part 1, international organization for standardization, geneva, 2013.

[103] A. Jablonski and C. J. Powell. Practical expressions for the mean escape depth, the information depth, and the effective attenuation length in auger-electron spectroscopy and x-ray photoelectron spectroscopy. *J. Vac. Sci. Technol. A*, 27:253–261, 2009.

[104] G. Olivieri, K. M. Parry, C. J. Powell, D. J. Tobias, and M. A. Brown. This parameter is defined as the ratio of the IMFP to the sum of the IMFP and the transport mean free path (TMFP). The TMFP is the inverse product of the density of atoms or molecules and the transport cross section that is calculated from the differential cross section for elastic scattering of electrons by the atoms or molecules.

[105] F. Tao, M. E. Grass, Y. W. Zhang, D. R. Butcher, J. R. Renzas, Z. Liu, J. Y. Chung, B. S. Mun, M. Salmeron, and G. A. Somorjai. Reaction-driven restructuring of rh-pd and pt-pd core-shell nanoparticles. *Science*, 322:932–934, 2008.

[106] H. Tissot, G. Olivieri, J. J. Gallet, F. Bournel, M. G. Silly, F. Sirotti, and F. Rochet. Cation depth-distribution at alkali halide aqueous solution surfaces. *J. Phys. Chem. C*, 119:9253–9259, 2015.

[107] G. Olivieri, K. M. Parry, C. J. Powell, D. J. Tobias, and M. A. Brown. See supplementary material for the detailed composition of each layer used as SESSA input parameters for 2 M KI and 1 M NaI in the instantaneous interface representation and 2 M KI in the GDS representation. For 1 M NaI the MD simulation results are shown.

[108] R. D'Auria and D. J. Tobias. Relation between surface tension and ion adsorption at the airwater interface: A molecular dynamics simulation study. *J. Phys. Chem. A*, 113:7286–7293, 2009.

[109] T. Goulet, A. Bernas, C. Ferradini, and J. P. Jay-Gerin. On the electronic structure of liquid water: Conduction-band tail revealed by photoionization data. *Chem. Phys. Lett.*, 170:492–496, 1990.

[110] A. Bernas, C. Ferradini, and J. P. Jay-Gerin. On the electronic structure of liquid water: Facts and reflections. *Chem. Phys.*, 222:151–160, 1997.

[111] J.V. Coe, A. D. Earhart, M. H. Cohen, G. J. Hoffman, H.W. Sarkas, and K. H. Bowen. Using cluster studies to approach the electronic structure of bulk water: Reassessing the vacuum level, conduction band edge, and band gap of water. *J. Chem. Phys.*, 107:6023–6031, 1997.

[112] J. V. Coe. Fundamental properties of bulk water from cluster ion data. *Int. Rev. Phys. Chem.*, 20:33–58, 2001.

[113] L. Onsager and N. N. T. Samaras. The surface tension of debye-huckel electrolytes. *Journal of Chemical Physics*, 2(8), 1934.

[114] J. Cheng, C. D. Vecitis, M. R. Hoffmann, and A. J. Colussi. Experimental anion affinities for the air/water interface. *J. Phys. Chem. B*, 110:25598–25602, 2006.

155

[115] R. Weber, B. Winter, P. M. Schmidt, W. Widdra, I. V. Hertel, M. Dittmar, and M. Faubel. Photoemission from aqueous alkali-metal-iodide salt solutions using euv synchrotron radiation. *Journal of Physical Chemistry B*, 108(15):4729–4736, 2004.

[116] J. H. Hu, Q. Shi, P. Davidovits, D. R. Worsnop, M. S. Zahniser, and C. E. Kolb. Reactive uptake of cl2(g) and br2(g) by aqueous surfaces as a function of br- and i-ion concentration - the effect of chemical-reaction at the interface. *J. Phys. Chem-Us*, 99:8768–8776, 1995.

[117] D. A. Case, D. A. amd Pearlman, J. W. Caldwell, T. E. III Cheatham, J. Wang, W. S. Ross, C. L. Simmerling, T. A. Darden, K. M. Merz, R. V. Stanton, A. L. Cheng, J. J. Vincent, M. Crowley, V. Tsui, H. Gohlke, R. J. Radmer, Y. Duan, J. Pitera, I. Massova, G. L. Seibel, U. C. Singh, P. K. Weiner, and P. A. Kollman. Amber 7, 2002.

[118] J. W. Caldwell and P. A. Kollman. Structure and properties of neat liquids using nonadditive molecular-dynamics - water, methanol, and n-methylacetamide. *J. Phys. Chem.*, 99:6208–6219, 1995.

[119] L. S. Sremaniak, L. Perera, and M. L. Berkowitz. Enthalpies of formation and stabilization energies of br-(h2o)n (n = 1,2,...,15) clusters - comparisons between molecular-dynamics computer- simulations and experiment. *Chem. Phys. Lett.*, 218:377–382, 1994.

[120] G. Markovich, L. Perera, M. L. Berkowitz, and O. Cheshnovsky. The solvation of cl-, br-, and i- in acetonitrile clusters: Photo- 682 electron spectroscopy and molecular dynamics simulations. *J. Chem. Phys.*, 105:2675–2685, 1996.

[121] H. J. C. Berendsen, J. P. M. Postma, W. F. Vangunsteren, A. Dinola, and J. R. Haak. Molecular-dynamics with coupling to an external bath. *J. Chem. Phys.*, 81:3684–3690, 1984.

[122] J. P. Ryckaert, G. Ciccotti, and H. J. C. Berendsen. Numerical-integration of cartesian equations of motion of a system with constraints - molecular-dynamics of n-alkanes. *J. Comput. Phys.*, 23:327–341, 1977.

[123] G. Olivieri, A. Goel, A. Kleibert, D. Cvetko, and M. A. Brown. Quantitative ionization energies and work functions of aqueous solutions. *Phys. Chem. Chem. Phys.*, 18:29506–29515, 2016.

[124] M. A. Brown, M. Faubel, and B. Winter. X-ray photo- and resonant auger-electron spectroscopy studies of liquid water and aqueous solutions. *Annu. Rep. Prog. Chem. C*, 105:174–212, 2009.

[125] G. Olivieri, J. B. Giorgi, R. G. Green, and M. A. Brown. 5 years of ambient pressure photoelectron spectroscopy (appes) at the swiss light source (sls). *J. Electron Spectrosc.*, 216:1–16, 2017.

[126] G. Olivieri, A. Goel, A. Kleibert, and M. A. Brown. Effect of x-ray spot size on liquid jet photoelectron spectroscopy. *J. Synchrotron. Radiat.*, 22:1528–1530, 2015.

[127] Niklas Ottosson, Jan Heyda, Erik Wernersson, Wandared Pokapanich, Svante Svensson, Bernd Winter, Gunnar Ohrwall, Pavel Jungwirth, and Olle Bjorneholm. The influence of concentration on the molecular surface structure of simple and mixed aqueous electrolytes. *Physical Chemistry Chemical Physics*, 12(36):10693–10700, 2010.

[128] C. D. Wick. Electrostatic dampening dampens the anion propensity for the air-water interface. *J. Chem. Phys.*, 131:084715, 2009.

[129] P. K. Weissenborn and R. J. Pugh. Surface tension of aqueous solutions of electrolytes: Relationship with ion hydration, oxygen solubility, and bubble coalescence. *J. Colloid Interf. Sci.*, 184:550–563., 1996.

[130] A. Grossfield, P. Ren, and J. W. Ponder. Ion solvation thermodynamics from simulation with a polarizable force field. *J. Am. Chem. Soc.*, 125:15671–15682, 2003.

[131] A. Arslanargin and T. L. Beck. Free energy partitioning analysis of the driving forces that determine ion density profiles near the water liquid-vapor interface. *J. Chem. Phys.*, 136:104503, 2012.

[132] M. D. Baer, A. C. Stern, Y. Levin, D. J. Tobias, and C. J. Mundy. Electrochemical surface potential due to classical point charge models drives anion adsorption to the air-water interface. *J. Phys. Chem. Lett.*, 3:1565–1570, 2012.

[133] K. D. Collins and M. W. Washabaugh. The hofmeister effect and the behavior of water at interfaces. *Quarterly Reviews of Biophysics*, 18(4):323–422, 1985.

[134] P. Lo Nostro and B. W. Ninham. Hofmeister phenomena: An update on ion specificity in biology. *Chem. Rev.*, 112:2286–2322, 2012.

[135] Y. Marcus. Effect of ions on the structure of water: Structure making and breaking. *Chem. Rev.*, 109:1346–1370, 2009.

[136] A. W. Omta, M. F. Kropman, S. Woutersen, and H. J. Bakker. Negligible effect of ions on the hydrogen-bond structure in liquid water. *Science*, 301:347–349, 2003.

[137] J. D. Smith, R. J. Saykally, and P. L. Geissler. The effects of dissolved halide anions on hydrogen bonding in liquid water. *J, Am. Chem. Soc.*, 129:13847–13856, 2007.

[138] T. Corridoni, R. Mancinelli, M.A. Ricci, and F. Bruni. Viscosity of aqueous solutions and local microscopic structure. *J. Phys. Chem. B.*, 115:14008–14013, 2011.

[139] S. et al. Funkner. Watching the low-frequency motions in aqueous salt solutions: The terahertz vibrational signatures of hydrated ions. *J. Am. Chem. Soc.*, 134:1030–1035, 2012.

[140] L. Vrbka, P. Jungwirth, P. Bauduin, D. Touraud, and W. Kunz. Specific ion effects at protein surfaces: A molecular dynamics study of bovine pancreatic trypsin inhibitor and horseradish peroxidase in selected salt solutions. *J. Phys. Chem. B*, 110:7036–7043, 2006.

[141] R. Zangi, M. Hagen, and B. J. Berne. Effect of ions on the hydrophobic interaction between two plates. *J. Am. Chem. Soc.*, 129:4678–4686, 2007.

[142] L. M. Pegram and M.T. Jr Record. Thermodynamic origin of hofmeister ion effects. *J. Phys. Chem. B*, 112:9428–9436, 2008.

[143] L. M. Pegram and M.T. Jr Record. Partitioning of atmospherically relevant ions between bulk water and the water/vapor interface. *Proc Natl Acad Sci USA*, 103:14278–14281, 2006.

[144] L. M. Pegram and M.T. Jr Record. Hofmeister salt effects on surface tension arise from partitioning of anions and cations between bulk water and the air-water interface. *J. Phys. Chem. B*, 111:5411–5417, 2007.

[145] T. M. Chang and L.X. Dang. Recent advances in molecular simulations of ion solvation at liquid interfaces. *Chem. Rev.*, 106:1305–1322, 2006.

[146] P. B. Petersen and R. J. Saykally. On the nature of ions at the liquid water surface. *Annu. Rev. Phys. Chem.*, 57:333–364, 2006.

[147] M. A. Brown, R. D'Auria, I. F. W. Kuo, M. J. Krisch, D. E. Starr, H. Bluhm, D. J. Tobias, and J. C. Hemminger. Ion spatial distributions at the liquid-vapor interface of aqueous potassium fluoride solutions. *Phys. Chem. Chem. Phys.*, 10:4778–4784, 2008.

[148] Chuanshan Tian, Steven J. Byrnes, Hui-Ling Han, and Y. Ron Shen. Surface propensities of atmospherically relevant ions in salt solutions revealed by phase-sensitive sum frequency vibrational spectroscopy. *J. Phys. Chem. Lett.*, 2(15):1946–1949, 2011.

[149] S. Gopalakrishnan, P. Jungwirth, D. J. Tobias, and H. C. Allen. Air-liquid interfaces of aqueous solutions containing ammonium and sulfate: Spectroscopic and molecular dynamics studies. *J. Phys. Chem. B*, 109:8861–8872, 2005.

[150] P. Jungwirth and D. J. Tobias. Ions at the air/water interface. *Journal of Physical Chemistry B*, 106(25):6361–6373, 2002.

[151] W. Hua, D. Verreault, and H. C. Allen. Surface electric fields of aqueous solutions of nh4no3, mg(no3)2, nano3, and lino3: Implications for atmospheric aerosol chemistry. *J. Phys. Chem. C*, 118:24941–24949, 2014.

[152] Niklas Ottosson, Manfred Faubel, Stephen E. Bradforth, Pavel Jungwirth, and Bernd Winter. Photoelectron spectroscopy of liquid water and aqueous solution: Electron effective attenuation lengths and emission-angle anisotropy. *Journal of Electron Spectroscopy and Related Phenomena*, 177(2-3), 2010.

[153] J. E. B. Randalls. Structure at the free surface of water and aqueous electrolyte solutions. *Phys. Chem. Liquids*, 7:107–179, 1977.

[154] W. Hua, D. Verreault, Z. Huang, E. M. Adams, and H. C. Allen. Cation effects on interfacial water organization of aqueous chloride solutions. i. monovalent cations: Li+, na+, k+, nh4+. *J. Phys. Chem. B*, 118:8433–8440, 2014.

[155] F. Bresme, E. Chacon, P. Tarazona, and A. Wynveen. The structure of ionic aqueous solutions at interfaces: An intrinsic structure analysis. *Journal of Chemical Physics*, 137(11), 2012.

[156] Y. Marcus. Ionic radii in aqueous solutions. *Chem. Rev.*, 88:1475–1498, 1988.

[157] Dale E. Otten, Patrick R. Shaffer, Phillip L. Geissler, and Richard J. Saykally. Elucidating the mechanism of selective ion adsorption to the liquid water surface. *Proceedings of the National Academy of Sciences of the United States of America*, 109(3):701–705, 2012.

[158] D. Ben-Amotz. Interfacial solvation thermodynamics. *J. Phys. Condens. Matter*, 28:414013, 2016.

[159] et al. Ogletree, D. F. A differentially pumped electrostatic lens system for photoemission studies in the millibar range. *Rev. Sci. Instrum.*, 73:3872–3877, 2002.

[160] et al Bluhm, H. Soft x-ray microscopy and spectroscopy at the molecular en- vironmental science beamline at the advanced light source. *J. Electron. Spectros. Relat. Phenomena*, 150:86–104, 2006.

[161] D. E. Starr, E. K. Wong, D. R. Worsnop, K. R. Wilson, and H. Bluhm. A combined droplet train and ambient pressure photoemission spectrometer for the investigation of liquid/vapor interfaces. *Phys. Chem. Chem. Phys.*, 10:3093–3098, 2008.

[162] C. Hahn, Z. R. Kann, J. A. Faust, J. L. Skinner, and G. M. Nathanson. Supermaxwellian helium evaporation from pure and salty water. *J. Chem. Phys.*, 144:044707, 2016.

[163] D. F. Ogletree, H. Bluhm, E. D. Hebenstreit, and M. Salmeron. Photoelectron spectroscopy under ambient pressure and temperature conditions. *Nucl. Instrum. Methods Phys. Res. A*, 601:151–160, 2009.

[164] Hendrik Bluhm. Photoelectron spectroscopy of surfaces under humid conditions. *Journal of Electron Spectroscopy and Related Phenomena*, 177(2-3), 2010.

[165] B. L. Henke, E. M. Gullikson, and J. C. Davis. X-ray interactionsphotoabsorption, scattering, transmission, and reflection at e=50-30,000 ev, z=1-92. *At. Data Nucl. Data Tables*, 54:181–342, 1993.

[166] H. J. C. Berendsen, J. R. Grigera, and T. P. Straatsma. The missing term in effective pair potentials. *J. Phys. Chem-Us*, 91:6269–6271, 1987.

[167] R. W. Impey, P. A. Madden, and I. R. McDonald. Hydration and mobility of ions in solution. *J. Chem. Phys.*, 87:5071–5083, 1983.

[168] Y. Marcus. Surface tension of aqueous electrolytes and ions. *J. Chem. Eng. Data*, 55:3641–3644, 2010.

[169] P. Jungwirth, D. Rosenfeld, and V. Buch. A possible new molecular mechanism of thundercloud electrification. *Atmos. Res.*, 76:190–205, 2005.

[170] M. Mochida, Y. Kitamori, K. Kawamura, Y. Nojiri, and K. Suzuki. Fatty acids in the marine atmosphere: Factors governing their concentrations and evaluation of organic films on sea-salt particles. *J. Geophys. Res. - Atmos.*, 107:1/1–1/10, 2002.

[171] R. E. Cochran, T. Jayarinthe, E. A. Stone, and V. H. Grassian. A test of surface activity in the composition of organic-enriched aerosols from bulle bursting. *J. Phys. Chem. Lett.*, 7:1692–1696, 2016.

[172] W. Hua, D. Verreault, and H. C. Allen. Surface prevalence of perchlorate anions at the air/aqueous interface. *J. Phys. Chem. Lett.*, 4:4231–4236, 2013.

[173] H. T. Bian, R. R. Feng, Y. Guo, and H. F. Wang. Specific na+ and k+ effects on the interfacial water molecules at the air/aqueous solution interfaces probed with nonresonant second harmonic generation. *J. Chem. Phys.*, 130:134709, 2009.

[174] P. Jungwirth, J. E. Curtis, and D. J. Tobias. Polarizability and aqueous solvation of the sulfate dianion. *Chem. Phys. Lett.*, 367:704–710, 2003.

[175] W. W. Rudolph, G. Irmer, and G. T. Hefter. Raman spectroscopic investigation of speciation in mgso4 (aq). *Phys. Chem. Chem. Phys.*, 5:5253–5261, 2003.

[176] M. Xu, J. P. Larentzos, M. Roshdy, L. J. Criscenti, and H. C. Allen. Aqueous divalent metal-nitrate interactions: Hydration versus ion pairing. *Phys. Chem. Chem. Phys.*, 10:4793–4801, 2008.

[177] K. M. Callahan, N. N. Casillas-Ituarte, M. Roeselov, H. C. Allen, and D. J. Tobias. Molecular dynamics simulation and vibrational spectroscopic study of magnesium chloride in aqueous solutions. *J. Phys. Chem. A*, 114:5141–5148, 2010.

[178] M. Xu, R. Spinney, and H. C. Allen. Water structure at the air-aqueous interface of divalent cation and nitrate soluitons. *J. Phys. Chem. B*, 113:4102–4110, 2009.

[179] Karen M. Callahan, Nadia N. Casillas-Ituarte, Man Xu, Martina Roeselov, Heather C. Allen, and Douglas J. Tobias. Effect of magnesium cation on the interfacial properties of aqueous salt solutions. *J. Phys. Chem. A*, 114(32):8359–8368, 2010.

[180] N. N. Casillas-Ituarte, K. M. Callahan, C. Y. Tang, X. Chen, M. Roeselova, D. J. Tobias, and H. C. Allen. Surface organization of aqueous mgcl2 and application to atmospheric marine aerosol chemistry. *Proc. Natl. Acad. Sci. USA*, 107:6616–6621, 2010.

[181] A. P. Ault, R. C. Moffet, J. Baltrusaitis, D. B. Collins, M. J. Ruppel, L. A. Cuadra-Rodriguez, D. Zhao, T. L. Guasco, C. J. Ebben, M. Geiger, F, T. H. Bertram, K. A. Prather, and V. H. Grassian. Size-dependent changes in sea spray aerosol composition and properties with different seawater conditions. *Environ. Sci. Technol.*, 47:5603–5612, 2013.

[182] C. J. Gaston, H. Furutani, S. A. Guazzotti, K. R. Coffee, T. S. Bates, P. K. Quinn, L. I. Aluwihare, B. G. Mithcell, and K. A. Prather. Unique ocean-derived particles serve as a proxy for changes in ocean chemistry. *J. Geophys. Res. - Atmos.*, 116:D18310, 2011.

[183] M. Heldal, S. Norland, E. S. Erichsen, R.-A. Sandaa, A. Larsen, F. Thingstad, and G. Bratbak. Mg2+ as an indicator of nutritional status in marine bacteria. *IMSE J.*, 6:524–530, 2012.

[184] J. Zhou, G. Santambrogio, M. Brummer, D. T. Moore, G. Meijer, D. M. Neumark, and K. R. Asmis. Infrared spectroscopy of hydrated sulfate dianions. *J. Chem. Phys.*, 125:111102, 2006.

[185] J. T. O'Brien, J. S. Prell, M. F. Bush, and E. R. Williams. Sulfate ion patterns water at long distance. *J. Am. Chem. Soc.*, 132:8248–8249, 2010.

[186] T. Wende, N. Heine, T. I. Yacovitch, K. R. Asmis, D. M. Neumark, and L. Jiang. Probing the microsolvation of a quaternary ion complex: Gas phase vibrational spectroscopy of (naso4-)2(h2o)n=0-6, 8. *Phys. Chem. Chem. Phys.*, 18:267–277, 2016.

[187] C. C. Pye and W. W. Rudolph. An ab initio and raman investigation of sulfate ion hydration. *J. Phys. Chem. A*, 105:905–912, 2001.

[188] K. J. Tielrooij, N. Garcia-Araez, M. Bonn, and H. J. Bakker. Cooperativity in ion hydration. *Science*, 328:1006–1009, 2010.

[189] X. B. Wang, X. Yang, J. B. Nicholas, and L. S. Wang. Bulk-like features in the photoemission spectra of hydrated doubly charged anion clusters. *Science*, 294:1322–1325, 2001.

[190] R. Buchner, T. Chen, and G. T. Hefter. Complexity in "simple" electrolyte solutions: Ion pairing in mgso4(aq). *J. Phys. Chem. B*, 108:2365–2375, 2004.

[191] K. W. Bruland and M. C. Lohan. *Control of Trace Metals in Seawater*, pages 23–48. Treatise on Geochemistry. Elsevier, Amsterdam, 2003.

[192] S. Nihonyanagi, S. Yamaguchi, and T. Tahara. Direct evidence for orientational flip-flop of water molecules at charged interfaces: A heterodyne-detected vibrational sum frequency generation study. *J. Chem. Phys.*, 130:204704, 2009.

[193] R. E. Pool, J. Versluis, E. H. G. Backus, and M. Bonn. Comparative study of direct and phase-specific vibrational sum-frequency generation spectroscopy: Advantages and limitations. *J. Phys. Chem. B*, 115:15362–15369, 2011.

[194] I. V. Stiopkin, H. D. Jayathilake, A. N.; Bordenyuk, and A. V. Benderskii. Heterodyne-detected vibrational sum frequency generation spectroscopy. *J. Am. Chem. Soc.*, 130:2271–2275, 2008.

[195] H. Vanselous and P. B. Petersen. Extending the capabilities of heterodyne-detected sum-frequency generation spectroscopy: Probing any interface in any polarization combination. *J. Phys. Chem. C*, 120:8175–8184, 2016.

[196] W. Hua, D. Verreault, E. M. Adams, Z. S. Huang, and H. C. Allen. Impact of salt purity on interfacial water organization revealed by conventional and heterodyne-detected vibrational sum frequency generation spectroscopy. *J. Phys. Chem. C*, 117:19577–19585, 2013.

[197] A. C. Finlayson. The ph range of the mohr titration for chloride ion can be usefully extended to 4-10.5. *J. Chem. Educ.*, 69:559, 1992.

[198] F.; Rull, Ch.; Balarew, J. L. Alvarez, F. Sobron, and A. Rodriguez. Raman spectroscopic study of ion association in aqueous magnesium sulphate solutions. *J. Raman Spectrosc.*, 25:933–941, 1994.

[199] C. Y. Tang and H. C. Allen. Ionic binding of na+ versus k+ to the carboxylic acid headgroup of palmitic acid monolayers studied by vibrational sum frequency generation spectroscopy. *J. Phys. Chem. A*, 113:7383–7393, 2009.

[200] W. Hua, A. M. Jubb, and H. C. Allen. Electric field reversal of na2so4, (nh4)2so4, and na2co3 relative to cacl2 and nacl at the air/aqueous interface revealed by heterodyne-detected phas-sensitive sum frequency. *J. Phys. Chem. Lett.*, 2:2515–2520, 2011.

[201] X. K. Chen, W. Hua, Z. S. Huang, and H. C. Allen. Interfacial water structure associated with phospholipid membranes studies by phase-sensitive vibrational sum frequency generation spectroscopy. *J. Am. Chem. Soc.*, 132:11336–11342, 2010.

[202] N. Ji, V. Ostroverkhov, C. S. Tian, and Y. R. Shen. Characterization of vibrational resonances of water-vapor interfaces by phase-sensitive sum-frequency spectroscopy. *Phys. Rev. Lett.*, 100:096102, 2008.

[203] S. Nihonyanagi, R. Kusaka, K.-i. Inoue, A. Adhikari, S. Yamaguchi, and T. Tahara. Accurate determination of complex c(2) spectrum of the air/water interface. *J. Chem. Phys.*, 143:124707, 2015.

[204] J. C. Phillips, B. Braun, W. Wang, J. Gumbart, E. Tajkhorshid, E. Villa, C. Chipot, R. D. Skeel, L. Kal, and K. Schulten. Scalable molecular dynamics with namd. *J. Comput. Chem.*, 26:1781–1802, 2005.

[205] J. A. Lemkul, J. Huang, B. Roux, and A. D. MacKerrel Jr. An empirical polarizable force field based on the classical drude oscillator model: Development history and recent applications. *Chem. Rev.*, 116:4983–5013, 2016.

[206] G. Lamoureux, E. Harder, I. V. Vorobyov, B. Roux, and A. D. MacKerell Jr. A polarizable model of water for molecular dynamics simulations of biomolecules. *Chem. Phys. Lett.*, 418:245–249, 2006.

[207] A. Vila Verde and R. Lipowsky. Solvent-shared pairs of densely charged ions induce intense but short-range supra-additive slowdown of water rotation. *Phys. Chem. Chem. Phys.*, 18:1918–1930, 2016.

[208] A. Vila Verde and R. Lipowsky. Cooperative slowdown of water rotation near densely charged ions is intense but short-ranged. *J. Phys. Chem. B*, 117:10556–10566, 2013.

[209] H. Yu, T. W. Whitfield, E. Harder, G. Lamoureux, I. Vorobyov, V. M. Anisimov, A. D. MacKerell, and B. Roux. Simulating monovalent and divalent ions in aqueous solution using a drude polarizable force field. *J. Chem. Theory Comput.*, 6:774–786, 2010.

[210] J. A. Lemkul and A. D. MacKerell Jr. Balancing the interactions of mg2+ in aqueous solution and with nucleic acid moieties for a polarizable force field based on the classical drude oscillator model. *J. Phys. Chem. B*, 120:11436–11448, 2016.

[211] H. Grubmller, H. Heller, A. Windemuth, and K. Schulten. Generalized verlet algorithm for efficient molecular dynamics simulation with long-range interactions. *Mol. Simul.*, 6:121–142, 1991.

[212] A. Morita and J. T. Hynes. Theoretical analysis of the sum frequency generation spectrum of the water surface. *Chem. Phys.*, 258:371–390, 2000.

[213] I. V. Stiopkin, C. Weeraman, P. A. Pieniazek, F. Y. Shalhout, J. L. Skinner, and A. V. Benderskii. Hydrogen bonding at the water surface revealed by isotopic dilution spectroscopy. *Nature*, 474:192–195, 2011.

[214] G. Gonella, C. Ltgebaucks, A. G. F. de Beer, and S. Roke. Second harmonic and sum-frequency generation from aqueous interfaces is modulated by interference. *J. Phys. Chem. C*, 120:9165–9173, 2016.

[215] Y. C. Wen, S. Zhu, X. Liu, S. S. Yang, R. Guo, G. S. Shi, H. P. Fang, Y. R. Shen, and C. S. Tian. Unveiling microscopic structures of charged water interfaces by surface specific vibrational spectroscopy. *Phys. Rev. Lett.*, 116:016101, 2016.

[216] M. Sovago, R. K. Campen, H. J. Bakker, and M. Bonn. Hydrogen bonding strength of interfacial water determined with surface sum-frequency generation. *Chem. Phys. Lett.*, 470:7–12, 2009.

[217] T. Ishiyama and A. Morita. Analysis of anisotropic local field in sum frequency generation spectroscopy with the charge response kernel water model. *J. Chem. Phys.*, 131:244714, 2009.

[218] E. A. Raymond, T. L. Tarbuck, M. G. Brown, and G. L. Richmond. Hydrogen-bonding interactions at the vapor/water interface investigated by vibrational sum-frequency spectroscopy of hod/h2o/d2o. *J. Phys. Chem. B*, 107:546–556, 2003.

[219] P. A. Pieniazek, C. J. Tainter, and J. L. Skinner. Surface of liquid water: Three-body interactions and vibrational sum-frequency spectroscopy. *J. Am. Chem. Soc.*, 133:10360–10363, 2011.

[220] J. Schaefer, E. H. G. Backus, Y. Nagata, and M. Bonn. Both inter- and intramolecular coupling of oh groups determine the vibrational response of the water/air interface. *J. Phys. Chem. Lett.*, 7:4591–4595, 2016.

[221] T. Imamura, Y. Mizukoshi, T. Ishiyama, and A. Morita. Surface structures of naf and na2so4 aqueous solutions: Specific effects of hard ions on surface vibrational spectra. *J. Phys. Chem. C*, 116:11082–11090, 2012.

[222] A. M. Baergen and D. J. Donaldson. Photochemical renoxification of nitric acid on real urban grime. *Environ. Sci. Technol.*, 47:815–820, 2013.

[223] B. D. Kay, V. Hermann, and A. W. Castleman, Jr. Studies of gas-phase clusters: The solvation of hno$_3$ in microscopic aqueous studies. *Chem. Phys. Lett.*, 80:469–474, 1981.

[224] Melissa C. Kido Soule, Patrick G. Blower, and Geraldine L. Richmond. Nonlinear vibrational spetroscopic studies of the adsorption and speciation of nitric acid at the vapor/acid solution interface. *J. Phys. Chem. A*, 111:3349–3357, 2007.

[225] S. Wang, R. Bianco, and J. T. Hynes. Depth-dependent dissociate of nitric acid at an aqueous surface: Car-parrinello molecular dynamics. *J. Phys. Chem. A*, 113:1295–1307, 2009.

[226] S. Nose. A unified formulation of the coinstant temperature molecular-dynamics methods. *J. Chem. Phys*, 81:511–519, 1984.

[227] S. Nose. A molecular-dynamics method for simulations in the canonical-ensemble. *Mol. Phys*, 52:255–268, 1984.

[228] J. VandeVondele, M. Krack, F. Mohamed, M. Parrinello, T. Chassaing, and J. Hutter. Quickstep: Fast and accurate density functional calculations using a mixed gaussian and plane waves approach. *Comput. Phys. Commun.*, 167:103, 2005.

[229] S. Goedecker, M. Teter, and J. Hutter. Separable dual-space gaussian pseudopotentials. *J. Phys. Rev. B*, 54:1703, 1996.

[230] S. Grimme. Semiempirical gga-type density functional constructed with a long-range dispersion correction. *J. Comput. Chem.*, 27:1787, 2006.

[231] A. D. Becke. Density-functional exchange-energy approximation with correct asymptotic behavior. *Phys. Rev. A*, 38:3098, 1988.

[232] C.T Lee, W.T. Yang, and R.G. Parr. Development of the colle-salvetti correlation-energy formula into a functional of the electron density. *Phys. Rev. B*, 37:785, 1988.

[233] Don W. Green and Robert H. Perry. *Perry's Chemical Engineers' Handbook, Eighth Edition.* McGraw-Hill, 8 edition, 2008.